Graphenated organic nanoparticles immunosensors for the detection of TB biomarkers

UNIVERSITY *of the*
WESTERN CAPE

By

PHELISA YONELA MGWILI

(BSc Honours)

A mini-thesis submitted in partial fulfilment of the requirements for the degree

of

Magister Scientiae in Nanoscience

Faculty of Science

University of the Western Cape

Bellville, Cape Town, South Africa

Supervisor: Dr Rachel Fanelwa Ajayi

Co-supervisor: Prof Emmanuel I. Iwuoha

November 2017

Abstract

Pulmonary Tuberculosis (TB) a disease second to HIV/AIDS is a global health problem that arises in two states; as an active state and as a latent state. Diagnosis of active TB is tedious and requires expensive procedures since there is no recognizable method for the sole detection of active TB. The current diagnosis consists of chest X-rays and multiple sputum cultures used for acid-fast bacilli detection. The TB diagnosis of children is particularly difficult which further complicates the diagnosis. Thus, rapid identification of this pathogen is important for the treatment and control of this infection to allow effective and timely therapy. In an effort to solve this issue, this study reports the development of immunosensors constructed with electroactive layers of amino groups functionalized graphene oxide (GO) doped respectively with green synthesized zinc oxide (ZnO NPs) nanoparticles and silver (Ag NPs) nanoparticles on glassy carbon electrodes. The surface morphology of GO, ZnO NPs, Ag NPs and their composites was revealed by employing High-Resolution Transmission Electron Microscopy (HR-TEM) and High-Resolution Scanning Electron Microscopy (HR-SEM) while the composition and structure of these materials were studied using Fourier Transform Infra-Red Spectroscopy (FTIR). The resultant graphene oxide-metallic composites were covalently attached with CFP-10 and/or ESAT-6 antibodies to achieve the electrochemical detection. The immunosensor was then used for the impedimetric and amperometric detection of anti-CFP-10 and/or anti-ESAT-6 antigens in standard solutions.

Keywords

Tuberculosis

Graphene oxide

Zinc oxide nanoparticles

Silver Nanoparticles

Composites

Nanoalloys

Antibodies

Immunosensors

Declaration

I Phelisa Yonela Mgwili declare that '*Graphenated organic nanoparticles immunosensors for the detection of TB biomarkers'* is my own work, that it has not been submitted before for any degree or examination in any other university, and that all the sources I have used or quoted have been indicated or acknowledged as complete references.

Phelisa Yonela Mgwili November 2017

Signed…… ……

Acknowledgement

To the Lord Almighty thank you for granting me strength and the courage to complete my work through difficult times.

To my supervisors, **Dr Fanelwa Ajayi** and **Prof Emmanuel Iwuoha** a big and special thanks to both of you for the encouraging words when I had no hope, for the support that you gave me and ensuring that I do better than what I thought I could. Also thank you for the supervision and guidance that you have given me throughout my work.

To **Dr Mawethu Bilibana** and **Miss Nomaphelo Ntshongontshi** your support and encouragement has gone a long way. I am thankful for working under your supervision in the laboratory.

To the staff of the **Chemistry Department and SensorLab members**, thank you for the patience, technical assistance, the love and the support you have given me. Your help is highly appreciated.

To my family and friends without your love, patience, encouragement and support I wouldn't be where I am today. You are sincerely appreciated. Thank you.

I also thank the **Nanoscience and Nanotechnology Postgraduate Teaching and Training Platform (NNPTTP) and the Department of Science and Technology (DST)** for awarding me an MSc Nanoscience Scholarship.

Dedication

This thesis is dedicated to my late father Zama Elliot Mgwili, my late sister Ntombekhaya Mgwili, my mother Notobile Fihliwe Mgwili, my siblings Vuyokazi and Akhona Mgwili and my lovely son Chulumanco Mgwili

Table of contents

List of abbreviations

Ag NPs	- Silver nanoparticles
CE	- Counter electrode
CV	- Cyclic voltammetry
CVD	- Chemical vapour deposition
CMI	- Cell-mediated-immune
CT	- Computerised tomography
CSF	- Cerebrospinal fluid
ELISA	- Enzyme-linked immunosorbent assay
EIS	- Electrochemical impedance
FDA	- Food and drug administration
GCE	- Glassy-carbon electrode
GO	- Graphene oxide
HIV	- Human immunodeficiency virus
HRP	- Horseradish peroxide
IFN	- Interferon-assays
IGRAS	- Interferon-gamma release assays
LED-FM	- Light emitting diode fluorescence
LOD	- Limit of detection

MRI	- Magnetic resonance imaging
Mtb	- Mycobacterium tuberculosis
PCR	- Polymer chain reaction
PET	- Position emission tomography
RIF	- Rifampicin
RE	- Reference electrode
SERS	- Surface –enhanced Raman spectroscopy
SJIA	- System juvenile idiopathic arthritis
TB	- Tuberculosis
TNF	- Tumour necrosis factor
TST	- Tuberculin skin test
UV-vis	- Ultraviolet-visible
WE	- Working electrode
WHO	- World health organization
ZnO NPs	- Zinc oxide nanoparticles

List of Table

List of Figures

Chapter 1

Introduction

This chapter gives a brief overview on the background of the tuberculosis bacterial infection and the different stages in which it occurs. This chapter also includes the problem statement, the motivation behind this study, the study aim and finally, the objectives of this study are also outlined in this chapter

1.1.Background

Tuberculosis, commonly known as TB, is a bacterial infection that can spread through the lymph nodes and bloodstream to any organ in the body but is often found in the lungs. Most people who are exposed to TB never develop symptoms because the bacteria can live in an inactive form in the body but, if the immune system weakens such as in people with HIV or the elderly, then TB bacteria can become active. In its active state, TB bacteria causes death of the tissues of the organs they infect and can be fatal if left untreated. TB can be detected through a skin test or a TB blood test. The skin test involves injecting a small amount of fluid called tuberculin into the skin of the arm [1]. The patient is then required to return within 48 to 72 hours to have a healthcare worker check the arm to see if a bump has developed or not. The healthcare worker will measure the bump and tell the patient if the reaction to the test is positive or negative. If it's positive, it usually means that the patient has been infected with the TB germ. Alternatively, the TB blood test measures how ones immune system reacts to the germs that causes TB [2].

According to World Health Organisation (WHO) 2015 report, it was estimated that about 1.4 million deaths occurred due to TB infection and an additional 0.4 million deaths from TB disease among HIV-positive patients [3]. It was estimated that for 2015 there were about 10.4

million new TB cases including 1.2 million among HIV-positive patients, of which 5.9 million were men, 3.5 million were women and 1.0 million were children [4]

TB bacteria occurs in three different stages namely; latent TB, pulmonary TB and extra pulmonary TB. Latent TB is when one has been infected with the TB bacteria but does not have any symptoms of active disease. Treatment for latent TB is usually recommended for people aged 35 years or under, patients infected with HIV regardless of their age, healthcare workers regardless of their age, people with evidence of scarring caused by TB, as shown on chest X-rays and those who had never received treatment. Treatment is not recommended for people who have latent tuberculosis and are over the age of 35 and who do not have HIV and are not healthcare workers. This is because the risk of liver damage caused by antibiotic treatment increases with age, and the risks of treatment may outweigh the benefits. Latent TB is also not always treated if it's suspected to be drug resistant. If this is the case, one may be regularly monitored to check that the infection does not become active. In some cases testing and the treatment for latent TB may be recommended for people who require treatment that will weaken their immune system, such as long-term corticosteroids, chemotherapy or tumour necrosis factor (TNF) inhibitors. This is because there is a risk of the infection becoming active. Treatment for latent TB generally involves either taking a combination of rifampicin and isoniazid for three months, or isoniazid on its own for six months [5].

Active pulmonary TB is a TB that affects the lungs and causes symptoms. Treatment involves a six-month course of a combination of antibiotics. The usual course of treatment is: two antibiotics (isoniazid and rifampicin) every day for six months with two additional antibiotics (pyrazinamide and ethambutol) every day for the first two months. It may be several weeks or months before a patient starts feeling better. The exact length of time will depend on the patient's overall health and the severity of their TB infection. After taking the medicine for two weeks, most patients are no longer infectious and feel better. However, it is important they

continue taking the medicine exactly as prescribed and to complete the whole course of antibiotics. Taking medication for six months is the most effective method of ensuring that the TB bacteria are killed. Suspension of the antibiotics before completing the course, or the dose may cause the TB infection to be resistant to the antibiotics. This is potentially serious as it can be difficult to treat and will require a longer course of treatment. When patients find difficulty in taking their medication every day, the treatment team can work together to find a solution. This may include the patient having regular contact with the treatment team at home, the treatment clinic, or somewhere else more convenient. If treatment is completed correctly, the patient should not need any further checks by a TB specialist. However, advice is given regarding spotting signs that the illness has returned, although this is rare. In rare cases TB can be fatal, even with treatment. Death can occur if the lungs become too damaged to work properly [6].

Additionally, extra pulmonary TB is a TB that occurs outside the lungs and can be treated using the same combination of antibiotics as those used to treat pulmonary TB. However, patients need to take them for 12 months. If TB is in areas such as the brain, a corticosteroid such as prednisolone will be prescribed to be taken for several weeks at the same time as your antibiotics. This will help reduce any swelling in the affected areas. As with pulmonary TB, it's important to take your medicines exactly as prescribed and to finish the whole course [7].

1.2.Problem statement

Currently used TB tests (such as Interferon-assays (IFN-γ), Sputum culture and polymer chain reaction test) are tedious and can take up to 8 weeks to provide results to indicate whether or not a TB suspected patient has been infected with TB. Because of the prolonged waiting periods patients have to endure, some of them die not because treatment fails but they do due

to the prolonged process of getting results. The cause of these unfortunate cases arises from the fact that when TB symptoms arise, usually patients have been severely infected and require immediate treatment which they cannot receive due to the unavailability of their results. This issue requires immediate attention and intervention through the development of rapid and fast TB detection methods so that patients can be diagnosed within a short period of time (in hours or minutes) and those infected can administer their treatment promptly.

1.3.Rationale and Motivation

Because TB may occur in either a latent or active form, the definitive diagnosis of active TB depends on the culture of mycobacteria from sputum or tissue biopsy. However, it can take weeks for these slow-growing bacteria to grow on specialized media. Since patients with latent TB do not require isolation or immediate drug therapy, it is useful to determine if a person is either infected or not, has a latent infection, or is actively infected with transmissible TB bacteria.

Consequently, doctors need a presumptive test(s) that could reasonably assure that the person is infected or not so that therapy can resume. After getting a patient's history and physical exam data, the next is usually the skin test (termed the Mantoux tuberculin skin test or the tuberculin skin test (TST)). Another test, interferon-gamma release assays (IGRA) can measure the immune response to Mycobacterium tuberculosis. Another useful test is the chest X-rays which can give evidence of lung infection while a sputum smear stained with certain dyes that are retained mainly (but not exclusively) by mycobacteria can show the presence of the bacterium. These tests, when examined by a doctor, are useful in establishing a presumptive diagnosis of either latent or active TB, and most doctors will initiate treatment based on their judgment of these tests. In addition, some of these tests are useful only in patients who were not vaccinated

with a TB vaccine but are less useful in vaccinated people. For some patients, culture studies still should be completed to determine the drug susceptibility of an infecting TB strain [8].

Other tests which have been developed such as polymerase chain reaction test (PCR) to detect TB antigens and the light-emitting diode fluorescence (LED-FM) microscopic technique to identify TB organisms with microscopy may be used. Two other TB blood tests also called IGRAs have been approved by the food and drug administration (FDA) and measure how strongly the body's immune system reacts to TB bacteria. IGRAs are recommended in testing patients who have been vaccinated against TB. Treatment for tuberculosis (TB) will usually involve a long course of antibiotics lasting several months. While TB is a serious condition that can be fatal if left untreated, deaths are rare if treatment is completed [9].

The aim of this study is to reduce the waiting period currently experienced by patients to attain their TB infection or non-infection results through the development of immunosensors which will provide results to patients promptly. These devices are envisaged to be portable, sensitive and selective thus allowing healthcare practitioners to administer treatment to diagnosed patients immediately after TB diagnosis. Ultimately, these devices will provide either a negative or a positive response in terms of a determined concentration value within seconds or minutes as opposed to 8 weeks which patients are currently experiencing. Immunosensors relay on the detection resulting from the formation of anigen-antibody complexes which is converted by means of a transducer to an electrical signal which can be recorded, processed and finally displayed.

1.4.Aim and Objectives

The aim of this study was to develop an electrochemical immunosensor device for the detection and quantification of the TB antigens anti-CFP-10 and/or anti-ESAT-6. The development of

the immunosensor was constructed with electroactive layers of amino functionalized graphene oxide (GO) doped with zinc oxide (ZnO NPs), and silver (Ag NPs) nanoparticles respectively on glassy carbon electrodes.

The objectives of this study were as follows:

- To synthesize and characterize zinc oxide nanoparticles (ZnO NPs)
- To synthesize and characterize silver nanoparticles (Ag NPs)
- To synthesize and characterize graphene oxide (GO)
- To synthesize and characterize composites of ZnO NPs/GO and Ag NPs/GO
- To design and develop electrochemical immunosensors based on the immobilization of CFP-10 and/or ESAT-6 antibodies onto the developed composites (ZnO NPs/GO and Ag NPs/GO respectively).
- To apply the developed immunosensor to anti-CFP-10 and/or anti-ESAT-6 antigens.

1.5.Thesis lay-out

This thesis is presented in eight chapters

Chapter 1: Gives brief background information on the project, the problem statement, the motivation as well as aims and objectives of this study.

Chapter 2: Provides a detailed literature review.

Chapter 3: Consists of reagents, procedures and instrumentations used to achieve the success of this study.

Chapter 4: Comprises of the morphological, spectroscopic as well as electrochemical results obtained from the synthesised Ag NPs.

Chapter 5: Comprises of the morphological, spectroscopic as well as electrochemical results obtained from the synthesised ZnO NPs.

Chapter 6: Comprises of the morphological, spectroscopic as well electrochemical results obtained from the synthesized GO.

Chapter 7: Comprises of the morphological, spectroscopic as well electrochemical results obtained from the synthesized Ag NPs/GO composite. This chapter also provides electrochemical results obtained from the developed electrochemical immunosensor of ESAT-6 antibodies on composites Ag NPs/GO.

Chapter 8: Comprises of the morphological, spectroscopic as well electrochemical results obtained from the synthesized ZnO NPs/GO composite. This chapter also provides electrochemical results obtained from the developed electrochemical immunosensor of CFP-10 antibody on composites ZnO NPs/GO.

Chapter 9: Conclusion and recommendations

References

1. Ko, P.Y., Lin, S.D., Tu, S.T., Hsieh, M.C., Su, S.L., Hsu, S.R. and Chen, Y.C., 2016. High diabetes mellitus prevalence with increasing trend among newly-diagnosed tuberculosis patients in an Asian population: a nationwide population-based study. *Primary care diabetes*, *10*(2), pp.148-155.

2. Zumla, A., Hafner, R., Lienhardt, C., Hoelscher, M. and Nunn, A., 2012. Advancing the development of tuberculosis therapy. *Nature Reviews Drug Discovery*, *11*(3), p.171.

3. World Health Organization, 2015. *World health statistics 2015*. World Health Organization.

4. Kumar, S., Pai, A.G., Tungenwar, P.N. and Bhandarwar, A.H., 2017. Isolated primary tuberculosis of spleen—A rare entity in the immuno-competent patient. *International journal of surgery case reports*, *30*, pp.93-96.

5. Phillips, P.P., Gillespie, S.H., Boeree, M., Heinrich, N., Aarnoutse, R., McHugh, T., Pletschette, M., Lienhardt, C., Hafner, R., Mgone, C. and Zumla, A., 2012. Innovative trial designs are practical solutions for improving the treatment of tuberculosis. *Journal of infectious diseases*, *205*(suppl_2), pp.S250-S257.

6. Thiruppathiraja, C., Kamatchiammal, S., Adaikkappan, P., Santhosh, D.J. and Alagar, M., 2011. Specific detection of Mycobacterium sp. genomic DNA using dual labeled gold nanoparticle based electrochemical biosensor. *Analytical biochemistry*, *417*(1), pp.73-79.

7. Gopi, A., Madhavan, S.M., Sharma, S.K. and Sahn, S.A., 2007. Diagnosis and treatment of tuberculous pleural effusion in 2006. *Chest*, *131*(3), pp.880-889.

8. Zhang, J.A., Liu, G.B., Zheng, B.Y., Lu, Y.B., Gao, Y.C., Cai, X.Z., Dai, Y.C., Yu, S.Y., Jia, Y., Chen, C. and Zhuang, Z.G., 2016. Tuberculosis-sensitized monocytes sustain immune response of interleukin-37. *Molecular immunology*, *79*, pp.14-21.

9. Broughan, J.M., Maye, D., Carmody, P., Brunton, L.A., Ashton, A., Wint, W., Alexander, N., Naylor, R., Ward, K., Goodchild, A.V. and Hinchliffe, S., 2016. Farm characteristics and farmer perceptions associated with bovine tuberculosis incidents in areas of emerging endemic spread. *Preventive veterinary medicine*, *129*, pp.88-98.

Chapter 2

Literature review

This chapter gives a brief discussion on Tuberculosis, the detection of Tuberculosis through different methods as well as the background on Tuberculosis biomarkers. Covered in this chapter is also the role of nanoparticles and their applications in the field of immunosensor development as well as a detailed explanation of how these nanoparticles form composites with graphene.

2.1. Tuberculosis

Tuberculosis (TB) is a chronic infectious disease which is spread by air-borne droplets and caused by the acid-fast *Mycobacterium tuberculosis (M.tb*). All cases of TB are found to be passed through a person to person via droplets for example when someone coughs, talks or sneeze, tiny droplets of the saliva or of the mucus are spread into the air at which they can be inhaled by another person [1]. Once these infectious particles reach the alveoli another cell called the macrophage immerse the TB bacteria. Then the bacteria can be transmitted to the lymphatic system and bloodstream and spread to other organs. The bacteria further multiply in organs that have high oxygen pressures, such as the upper lobes of the lungs, the kidneys, spinal cord, bone marrow, and the membrane-like coverings of the brain [2]. According to World Health Organization (WHO) 2016 annual report, an estimated 10.4 million people developed TB and 1.5 million died from the disease [3]. TB begins by showing no symptoms infection that has a low number of *Mycobacterium tuberculosis (M.tb)*. TB infected patients may not notice any symptoms of illness until the disease has quite advanced. Even then the symptoms might be that of weight loss, loss of energy, poor appetite, fever, productive cough and some night sweats. Only about 10% of people infected with *Mycobacterium tuberculosis (M.tb)* ever

develop tuberculosis disease. Many of those who suffer TB do so in the first few years following infection. However, the bacillus may lie dormant in the body for decades [4]. Although most initial infections have no symptoms and people overcome them, they may develop fever, abnormalities and dry cough which can be only seen on chest x-ray and this kind of TB is mostly known as primary pulmonary TB, a TB that can go away on itself with no treatment needed.

TB diagnosis can be done through skin test, TB blood test, and chest x-ray and sputum culture. Once the patient has been diagnosed with TB then they will have to undergo a treatment, depending on a patient's health and also whether the patient is infected with pulmonary or extra pulmonary TB. If the patient is infected with pulmonary TB the treatment involves a six-month course of antibiotics which includes isoniazid and rifampicin every day for a period of 6 months with additional antibiotics (pyrazinamide and ethambutol) every day for the first two months [5]. But then if the patient is infected with extra-pulmonary TB, the TB can be treated using the same combination of antibiotics as those used to treat pulmonary TB. However, patients need to take them for 12 months. If TB is in areas such as brain, a corticosteroid such as prednisolone will be prescribed to be taken for several weeks at the same time as antibiotics. This will help reduce any swelling in the affected areas [6].

2.2. Different types of TB strains

Tuberculosis (TB) is divided into two categories: pulmonary (a contagious bacterial infection that involves lungs and may spread to other organs) and extrapulmonary (a bacterial infection that involves other organs except lungs such as lymph nodes, abdomen, skin, bones, meninges, pleura and joints).

2.2.1. Types of Pulmonary Tuberculosis

Pulmonary TB is a contagious TB that is caused by Mycobacterium tuberculosis (M.TB). This type of bacteria can spread easily from an infected patient to another through lymph nodes for example it can be spread when coughing or sneezing. Pulmonary TB has different types of TB's which are classified under it and are mentioned below.

- Primary Tuberculosis Pneumonia
- Tuberculosis Pleurisy
- Cavitary Tuberculosis
- Miliary TB [6]

2.2.2. Types of Extra-pulmonary Tuberculosis

Extra-pulmonary Tuberculosis occurs primarily in immuno-compromised patients. Immuno-compromised patients are patients who do not have ability to respond normally to an infection due to an impaired or weakened immune system. This inability to fight infection can be caused by a number of conditions including illness and disease (eg, diabetes, HIV), malnutrition, and drugs. [8]. Types of extra-pulmonary Tuberculosis include;

- Lymph Node Disease
- Tuberculosis Peritonitis
- Tuberculosis Pericarditis
- Osteal Tuberculosis
- Renal Tuberculosis
- Tuberculosis Meningitis

2.3. Detection of Tuberculosis

According to the statistics of the World Health Organization's (WHO) global tuberculosis (TB) report of 2016, 75% of the world's population is infected with *Mycobacterium tuberculosis (M.tb)* which is the cause of human TB. It has been estimated that about 9.8 million people developed TB and 1.5 million died from TB in 2015 [12]. South Africa alone accounted for 38 % of the total TB cases among 93 % of TB deaths occurring in middle class income countries [8]. Targets for the post 2016 global TB strategy include 95 % reduction in TB deaths and 90 % reduction in TB incidences by 2035. In order for these targets to be achieved implementation of new diagnostic tools is needs to be the immediate focus.

Because TB may occur as either in the latent or active form, the definitive diagnosis of active TB depends on the culture of mycobacteria from sputum or tissue biopsy. However, it may take weeks for these slow-growing bacteria to grow on specialized media. Since patients with latent TB do not require isolation or immediate drug therapy, it is useful to determine if a person is infected or not; whether they have a latent infection, or active transmissible TB bacteria [12]. Consequently, doctors need a presumptive test(s) that could reasonably assure that the person was infected or not so therapy could begin. After getting a patient's history and physical exam data, usually the next test is the skin test (termed the Mantoux tuberculin skin test or the tuberculin skin test (TST)). The test involves injecting tuberculin (an extract made from killed mycobacteria) into the skin. In about 48-72 hours, the skin is examined for induration (swelling) by a qualified person; a positive test (induration) strongly suggests the patient has either been exposed to live mycobacteria or is actively infected [13]. Another test, interferon-gamma release assays (IGRA) can measure the immune response to Mycobacterium tuberculosis. Other quick tests which are useful include chest X-rays which give evidence of lung infection while on the other hand sputum smear stained with certain dyes that are retained mainly (but not exclusively) by mycobacteria can show the presence of the bacterium [14].

Therefore it was said that chest x-ray are less cost-effective compared to culture sputum. It is less sensitive in detecting patients with active TB but could not be used in daily basis due to its high risk of unnecessary radiation exposure [15].

These tests, when examined by doctors are useful in establishing a presumptive diagnosis of either latent or active TB, and most doctors will initiate treatment based on their judgment of these tests. In addition, some of these tests are useful only in people who are not vaccinated with a TB vaccine but are less useful in vaccinated people. For some patients, culture studies still need to be completed to determine the drug susceptibility of an infecting TB strain [13].

The current or existing diagnostic tools have two major gaps namely; lack of recombinant biomarker that can be used to identify latent infected individuals who will benefit from the therapy and the lack of simple, fast and accurate point of care test that can give rapid diagnosis at the primary care level. Even though the acid-fast staining of bacilli in the sputum smear is a relatively simple method and relatively a fast test, it has the disadvantage of reduced sensitivity and requires N104 bacilli per ml of sputum for the reliable detection of active TB [16]. Sputum culture test is considered to be the best diagnostic tool for testing active TB even though it has some disadvantages like it takes weeks to obtain results, it is also expensive and requires a well-equipped laboratory with very well trained staff, and a well-organized transport system to ensure viable specimens. However in most cases about 5-10% active TB cases often gives negative results [17].

Other tests have been developed such as polymerase chain reaction (PCR) test to detect TB antigens and the LED-FM microscopic technique to identify TB organisms with microscopy. Two TB blood tests known as interferon-gamma release assays or IGRAs have been approved by the FDA and measure how strongly the body's immune system reacts to TB bacteria. IGRAs are recommended in testing patients who have been vaccinated against TB [18].

After discovering the failure of the above mentioned detection techniques new techniques such as immune reaction based on cell-mediated-immune (CMI) or humoral immune response have been investigated. Polymerase chain reaction (PCR) based molecular methods for detecting Mycobacterium TB-specific nucleic acids, especially WHO public approval of GeneXpert Mycobacterium TB/RIF have radically changed the diagnosis of active TB and rifampicin resistant TB. However, they are costly and require technological investments [18]. The GeneXpert Mycobacterium TB/RIF assay is a commercial real time polymerase chain reaction (PCR) cartridge based assay for the simultaneously detection of mycobacterium tuberculosis complex and resistance to rifampicin from sputum samples within 2 hours. The assay is approved by the manufacture for testing sputum samples but it is not approved for other respiratory specimens such as bronchoscopically collected samples and endotracheal aspirates [19].

Hence, this study has explored the development of immunosensors to improve on the failures that are recognised in the above mentioned diagnosis techniques. The success of these immunosensors is based on the sensitivity found in the use of electrochemistry to study the prompt responses facilitated by the use of conductive and electro-active materials in the immunosensor design.

2.4. Treatment of Tuberculosis

Treatment for tuberculosis (TB) usually involves a long course of antibiotics lasting several months. While TB is a serious condition that can be fatal if left untreated, on the other hand deaths are rare if treatment is completed. If the patient is diagnosed with TB, the patient will be given a six-month course of a combination of antibiotics. The usual course of treatment is:

- two antibiotics (isoniazid and rifampicin) every day for six months

- Two additional antibiotics (pyrazinamide and ethambutol) every day for the first two months.

It may be several weeks or months before the patient starts to feel better. The exact length of time will depend on the patients overall health and the severity of the TB infection. After taking the medicine for two weeks; most people are no longer infectious and feel better however, it is important to continue taking the medicine exactly as prescribed and to complete the whole course of antibiotics. Taking medication for six months is the most effective method of ensuring the TB bacteria are killed [20]. If the patient stop taking antibiotics before the course is complete, or they skip a dose, the TB infection may become resistant to the antibiotics. This is potentially serious as it can be difficult to treat and will require a longer course of treatment. If the patient finds it difficult to take medication every day, the treatment team can work with the patient to find a solution. This may include having regular contact with the treatment team at home, the treatment clinic, or somewhere else more convenient. If treatment is completed correctly, the patient should not need any further checks by a TB specialist afterwards. However, the patient may be given advice about spotting signs that the illness has returned, although this is rare. In rare cases TB can be fatal, even with treatment if the lungs become too damaged to work properly [20].

2.5. ESAT-6 and CFP-10 antibody for the detection of TB biomarkers anti-ESAT-6 and anti-CFP-10

An antigen detection assay for TB can be performed using a variety of clinical specimens such us sputum, blood, urine, saliva, cerebrospinal fluid (CSF), and pleural fluid. Antigens that are found from *M. tb* infected tissues can be present in the body fluids surrounding these tissues wherefrom they can reach the blood circulation and be excreted in urine which is a highly

practical specimen for diagnostic tests. Urine is known to be a safer sample to handle and less variable than sputum, beside that it is easier to collect from both adults and children. Additionally urine based assays could facilitate TB diagnosis in HIV co-infected patients, who normally have a low bacterial load in sputum [42]. Different types of biomarkers which have been used in detection of TB are listed in table 1 together with their functions.

Table 1: A list of different types of biomarkers and their functions

Gene	Rv number	Protein information (Alternative nomenclature)	Function	Diagnostic evidence
Apa	Rv1860	Alanine proline rich secreted protein APA (immunogenic protein MPT32; 45-kDa glycoprotein; 45/47 kDa antigen).	Unknown (could mediate bacterial attachment to host cells).	Tested in sputum and serum of active smear-positive TB patients [40]
EsxA	Rv3875	6 kDa Early secretory antigen target ESXA (ESAT-6)	Elicits high level of IFN-gamma from memory effector cells during first phase of a protective immune response. Co-transcribed with Rv3874 (CPF10)	Detected in cerebrospinal fluid (CSF) of tuberculous meningitis patients [41]
FbpA	Rv3804c	Secreted antigen 85-A FBPA (mycolyl transferase 85A; fibronectin-binding protein A; antigen 85 complex A).	Involved in cell wall mycoloylation. Proteins of the antigen 85 complex are responsible for the high affinity of mycobacteria to fibronectin. Possess a mycolyltransferase activity required for the biogenesis of trehalose dimycolate (cord factor), a structure necessary for maintaining cell wall integrity	Antigen 85 complex proteins have been detected in sputum [40]
FbpB	Rv1886c	Secreted antigen 85-B FBPB (mycolyl transferase 85B; fibronectin-binding protein B; antigen 85 complex B)	Same function as fbpA	Same diagnostic as fbpA [40]

FbpD	Rv3803c	Secreted MPT51/MPB51 antigen protein FBPD (MPT51/MPB51 antigen 85 complex C; mycolyl transferase 85C; fibronectin-binding protein C)	Same function as fbpA	Same diagnostic as fbpA [40]
GlcB	Rv1837c	Malate synthase G (GlcB)	Involved in glyoxylate bypass, an alternative to the tricarboxylic acid cycle.	Assayed with promising results in CSF in tuberculous meningitis [21].
groEL2	Rv0440	60 kDa chaperonin 2 GROEL2 (GROEL protein 2; 65 kDa antigen; heat shock protein 65)	Prevents misfolding and promotes folding and proper assembly of unfolded polypeptides	Showed a good diagnostic performance in ELISA of serum samples of TB patients [21].
HspX	Rv2031c	Heat shock protein HSPX (alpha-crystallin homolog; 14 kDa antigen; 16 kDa antigen; HSP16.3)	Stress protein induced by anoxia. HSPX has a proposed role in maintenance of long-term viability during latent, asymptomatic infections, as well as in replication during initial infection.	Assayed with promising results in CSF in tuberculous meningitis [21].
MoeX	Rv1681	Possible molybdopterin biosynthesis protein MoeX	Involved in molybdopterin cofactor biosynthesis	Identified by mass spectrometry in urine from active tuberculosis patients [40]
mpt64	Rv1980c	24 kDa immunogenic protein MPT64 (antigen MPT64/MPB64).	Secreted protein of unknown function specific for M. tuberculosis complex. Highly secreted during initial phases of bacterial growth.	A lateral flow assay was developed for the identification of M. tuberculosis complex in liquid culture media by using anti-MPB64 monoclonal antibodies [40].
pstS1	Rv0934	Periplasmic phosphate-binding lipoprotein PSTS1 (PBP-1; immunodominant 38 kDa protein; protein antigen B).	Involved in active transport of inorganic phosphate across the membrane [41]	Assayed in CSF in tuberculous meningitis [41].

TB31.7	Rv2623	Universal stress protein family protein TB31.7.	Regulates mycobacterial growth and is required for the entry of tubercle bacillus into the chronic phase of infection [41].	Potential biomarker for the diagnosis of latent as well as active tuberculous meningitis infection. Assayed in CSF [41].

With all the information given above ESAT-6 and CFP-10 can be used for the detection of Pulmonary TB due to their high levels of interferon (IFN)-gamma of memory effector cells. The early secreted antigenic target-6 (ESAT-6) and culture filtrate protein-10 (CFP-10) are considered as good surrogate biomarkers for TB detection [41]. ESAT-6 and CFP-10 are secreted by the ESX-1 secretion system, which is encoded for by the Mycobacterium Tuberculosis genomic region of difference one (RD1). The RD1 is important in the pathogenesis of MTB and distinguishes TB from non-TB-causing mycobacteria [42]. ESAT-6 and CFP-10 are associated in the pathogenesis of TB and the role of these proteins is that they extract cellular immune response in MTB-infected individuals. Their expression is associated with an increase in the cytolysis ability of MTB [43]. The proposed pathogenesis mechanism for ESAT-6 and CFP-10 is a two-fold system namely: T-cell activation and macrophage deactivation. A remarkable feature of the CFP-10 and ESAT-6 complex is their long flexible arm formed by the C-terminus of CFP- 10 and ESAT-6 that plays a key role in the virulence of the infection. This arm is considered as a contact point through which MTB interacts with host cell surfaces. Thus, due to their role in MTB pathogenicity and relatively restricted distribution in pathogenic mycobacteria, the antigenic pair will serve as good surrogate biomarkers for TB detection [44].

Thus, the focus of this study was the respective detection of these biomarkers using immunosensors.

2.6. Immunosensors

Immunosensors are compact analytical devices in which the event of formation of antigen-antibody complexes is detected and converted by means of a transducer to an electrical signal which can be processed, recorded and displayed. Different transducing mechanisms are employed in immunological biosensors, based on signal generation (such as an electrochemical or optical signal) or changes in properties (such as mass changes) following the formation of antigen-antibody complexes [32].

2.6.1.1. Electrochemical immunosensors

In electrochemical immunosensors, the event of the formation of antigen-antibody complex is converted into an electrical signal and can be studied through amperometric immunosensors, potentiometric immunosensors or conductimetric immunosensors. The most common type of amperometric immunosensors can be regarded as ELISA tests where redox species generated by a redox enzyme (enzymatic label) are converted into a measurable current. The aim of the test is to detect the presence of antibodies in serum via the formation of antigen-antibody complexes.

In electrochemical measurements the usual strategy is to immobilize the antigen onto the surface of a conductive electrode such as gold through adequate molecular linkers, for instance amino or carboxylic acid thiols. Thiols strongly bind to the gold surface, forming a self-assembled monolayer and providing the amino or carboxylic groups at the end of a small hydrocarbonated chain to which proteins can be covalently bonded. During an incubation time (typically from 30 to 60 minutes) with a positive serum, antigen-antibody complexes are formed. After rinsing, a second incubation is carried out with a solution containing anti-human

Ig antibodies labelled with a redox enzyme, such as horseradish peroxidase (HRP). The formation of the antigen-antibody labelled antibody complex is detected after the addition of the enzyme substrate and a proper redox mediator (cofactor). In the case of HRP, the substrate is hydrogen peroxidase and the redox mediator must be an adequate electron donor (a reduced species such as hydroquinone). HRP enzymatic activity converts the reduced redox mediator (hydroquinone) into an oxidized one (benzoquinone), which is further electrochemically reduced at the electrode surface [33]. A typical immunosensor example and its components is represented in Figure 2.1.

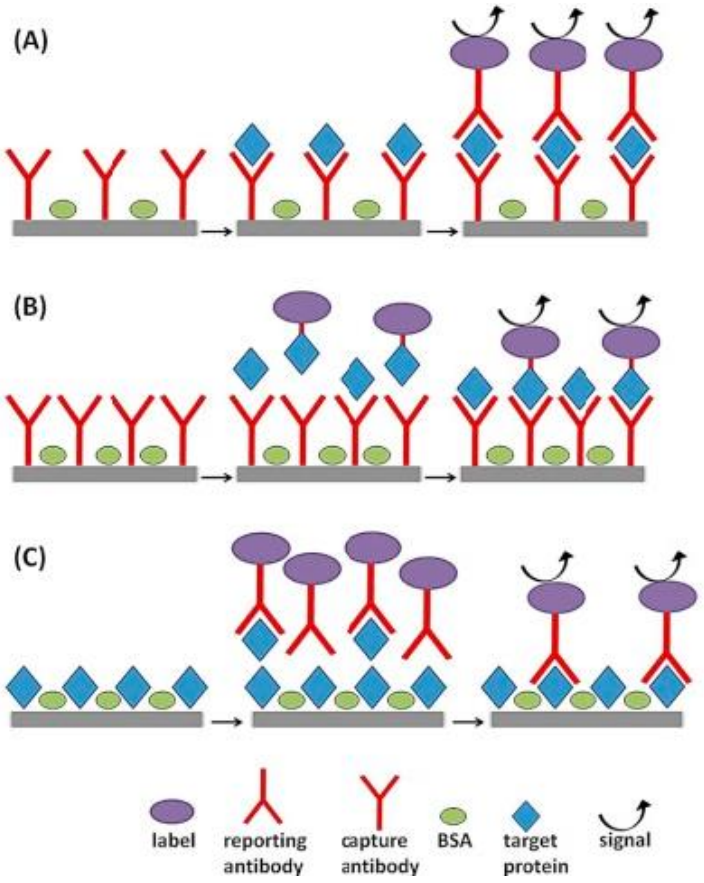

Figure 2.1: An illustration of various components of an electrochemical immunosensor [32]

2.6.1.2. Optical immunosensors

In an optical immunosensor, the biologically sensitive element is immobilized onto the surface of the transducer and responds to the interaction with the target analyte either by generating an optical signal, such as fluorescence or by undergoing changes in optical properties, such as absorption, reflectance, emission, refractive index, and optical path. The optical signals are collected by a photo-detector and converted into electrical signals that are further electronically processed [34].

2.6.1.3. Piezoelectric immunosensors

The mass changes that take place after the formation of antigen-antibody formation can be measured by means of piezoelectric transducers, such as quartz crystal microbalances and micro cantilevers which vibrate at a certain frequency sensitive. Antigens or antibodies can be immobilized onto the surface of piezoelectric devices and the formation of the antigen/antibody complex can be detected as a vibration frequency shift with a high sensitivity [35].

2.6.2. Metal Nanoparticles for immunosensor detection

Metallic nanoparticles have fascinated scientists for over a century and are now heavily utilized in biomedical sciences and engineering. They are a focus of interest because of their huge potential use in nanotechnology [23]. Today these materials can be synthesized and modified with various chemical functional groups which allow them to be conjugated with antibodies, ligands, and drugs of interest and thus opening a wide range of potential applications in biotechnology, magnetic separation, the pre-concentration of target analytes, targeted drug delivery, are vehicles for gene and drug delivery and more importantly are used in diagnostic

imaging [23]. Moreover, various imaging modalities have been developed over the period of time such as Magnetic Resonance Imaging (MRI), Computerized tomography (CT), Positron Emission Tomography (PET), Ultrasound, Surface-enhanced Raman Spectroscopy (SERS) and optical imaging as an aid to image various disease states [24]. These imaging modalities differ in both techniques and instrumentation and more importantly require a contrast agent with unique physiochemical properties. This led to the invention of various nanoparticulated contrast agents such as magnetic nanoparticles (Fe_3O_4), gold, zinc and silver nanoparticles for their application in these imaging modalities [23]. Therefore, this study explored the use of zinc oxide nanoparticles (ZnO NPs) and silver nanoparticles (Ag NPs) to enhance the surface area of the immunosensor for the detection of TB biomarkers [24].

Among metal oxide nanoparticles, zinc oxide (ZnO) nanoparticles are the most studied due to their large exciton binding energy (60 MeV), a wide direct band gap as well as high electron mobility (210 $cm^2\ V^{-1}\ S^{-1}$). According to literature, ZnO is relatively stable at physiological pH, compatible with biological fluids and species [25], and therefore suitable for in vivo application. This makes ZnO most suitable to be incorporated as immunosesor material to increase sensitivity due to its high isoelectric points which promote biomarker adsorption [26].

On the other hand, silver nanoparticles have unique optical, electrical, and thermal properties and are being incorporated into products that range from photovoltaic to biological and chemical sensors [25]. Examples include conductive inks, pastes and fillers which utilize silver nanoparticles for their high electrical conductivity, stability, and low sintering temperatures [26]. Additional applications include molecular diagnostics and photonic devices, which take advantage of the novel optical properties of these nanomaterials [27]. An increasingly common application is the use of silver nanoparticles for antimicrobial coatings, and many textiles,

keyboards, wound dressings, and biomedical devices now contain silver nanoparticles that continuously release a low level of silver ions to provide protection against bacteria [27].

They also play a vital role as metal nanoparticles mostly in cosmetics and also in sensors. In recent years silver nanoparticles (Ag NPs) have attracted many researchers interest because of their advantageous applications in biomedical, drug delivery, food industries, agriculture, textile industries, water treatment, catalysis and surface enhanced Raman scattering [28]. In this study Ag NPs have been used with GO to form a composite Ag NPs /GO which was used in conjunction with an antibody to produce an immunosensors that were used for TB detection.

Nanoparticles are used in immunosensors due to their unprecedented optical tunability as well as electrical and electrochemical qualities. Properties of nanoparticles such as light absorption and dispersion brings about interesting immunosensing alternatives at which they are improving the sensitivity of existing techniques used for protein detection in immunosensors based on Surface Plasmon Resonance, Quartz Crystal Microbalance, Fluorescence spectroscopy etc [28]. Electrochemical techniques are also taking advantage of electrical properties of nanoparticles. Redox properties of metal based nanoparticles, surface impedance change and conductance changes once nanoparticles are present as modifiers of transducer surfaces also result in better detection in the immunosensors [29].

Silver nanoparticles and zinc oxide nanoparticles were synthesized using green methods where pear extract and green tea were used respectively. Green nanotechnology is a new field aiming to replace the classical methods of obtaining nanoparticles which employ toxic and expensive chemicals with high energy input and negative effects on the environment [29]. Ever since the introduction of the concept by which an individual atom and molecules were manipulated and developed a discovery of the novel properties of nanomaterials was made [30]. These are currently being exploited over a wide range of applications such as drug delivery systems for

diagnosis and treatment, in the technology field where they are used as semiconductors as well as in environmental applications and industrial as catalysts [31].

2.6.3. Nanocomposites of graphene suitable for immunosensors

Due to its isolation and measurement of its unique properties graphene has been the centre of interest to the entire community of scientists looking for properties of carbon [36]. Quickly after its initial discovery, graphene was used to make electronic devices for a variety of applications [36]. Because high quality sheets of graphene is often prepared by chemical vapour deposition (CVD) which requires expensive equipment, many groups have looked at using graphene oxide as a solution processable alternative for the preparation of graphene like materials. Indeed, graphene oxide can be reduced in solution and as a thin film using a variety of reducing conditions; and reduction converts the graphene oxide into a material that has a large enhancement in electrical conductivity. In addition to its use in making reduced graphene oxide for electronic devices, graphene oxide has been used in catalytic oxidation biotechnology and as a surfactant. Graphene is also related to carbon nanomaterials such as carbon nanotubes and fullerene [36].

Graphene is usually prepared by the reduction of its precursor graphene oxide [37] a typical pseudo-two-dimensional oxygen-containing solid in bulk form, possessing functional groups including hydroxyls, epoxides, and carboxyl's [30]. Both graphene and graphene oxide literature show very high mechanical properties with good biocompatibility, and they have potential application as biomaterials [38]. The chemical groups of graphene oxide have been found to be a feasible and effective means of improving the dispersion of graphene. In addition functional side groups bound to the surface of graphene oxide or graphene sheets are there to improve the interfacial interaction between graphene oxide/graphene and the matrix similarly

to that observed for functionalized carbon nanotube-based nanocomposites [39]. Therefore by combining remarkable mechanical properties and low costs, 2D graphene or graphene oxide sheets are expected to offer promising nanoscale filler for the next generation of nanocomposite materials [31]. In particular, some important reports have discussed in detail their fascinating applications such as organic conductive films and heat-resistant material of graphene oxide–polymer nanocomposites [31]. Since graphene oxide can be dispersed at the individual sheet level in water, it is possible to achieve a truly molecular-level dispersion of graphene oxide if water is used as the common solvent for both graphene oxide and the polymer matrix. In addition, it has been reported that the epoxy groups in graphene oxide favour to react with primary amine group by addition, which has been widely used to modify graphene oxide [32]. So it is possible to form a graphene oxide composite with nanomaterials through the special interaction of graphene besides the H-bonding between them.

According to literature, composites infused with graphene are stronger, stiffer, and less prone to failure than composites infused with carbon nanotubes [32]. Graphene is said to have three distinct advantages over carbon nanotubes. The first advantage is the rough and wrinkled surface texture of graphene, caused by a very high density of surface defects. These defects are a result of the thermal exfoliation process that is used to manufacture bulk quantities of graphene from graphite [31]. These wrinkly surfaces interlock extremely well with the surrounding nanoparticle material, helping to boost the interfacial load transfer between graphene and the host material [32]. The second advantage is surface area. As a planner sheet, graphene benefits from considerably more contact with the host material than the tube-shaped carbon nanotubes. This is because the host materials usually nanoparticles are unable to enter the interior of the nanotubes, but both the top and bottom surfaces of the graphene sheet can be in close contact with the nanoparticle matrix [33]. The third benefit is geometry. When micro cracks in the composite structure encounter a two-dimensional graphene sheet, they are

deflected, or forced to tilt and twist around the sheet. This process helps to absorb the energy that is responsible for propagating the crack [32]. Crack deflection processes are far more effective for two-dimensional sheets with a high aspect ratio such as graphene, as compared to one-dimensional nanotubes [32]. The nanocomposites synthesized in this study are ZnO NPs/Go and Ag NPs/Go which will be used to develop immunosensors for the detection of ESAT-6 and CFP-10 antigens.

A detection of Mycobacterium Tuberculosis infection using a pool of synthetic peptides derived from ESAT-6 and CFP-10 proteins has been used by Paolo Scarpellini and his group to detect the number of specific gamma interferon-producing T cells by means of an enzyme-linked immunospot assay. The test results were highly specific (87.5%) and sensitive (93.1%). [26].

The immunosensor composition of ZnO NPs/GO and Ag NPs/ GO with ESAT-6 and CFP-10 carried out in this study were seen to have improved the detection limits as opposed to the above mentioned techniques due to the use of GO composite which have high surface areas, organic conductivity and biocompatibility.

2.7. Electrochemical techniques in immunosensor development

2.7.1. Cyclic Voltammetry (CV)

All electrochemical experiments including cyclic voltammetry, square wave and electrochemical impedance were carried out using a Palmsensor monitored on a PSTrace software. A conventional three electrode set up was used for all electrochemical analyses; as shown in Figure 2.2**.** This three electrode system consisted of a 10 mL electrochemical cell, immersed were three electrodes in an electrolyte solution. A glassy-carbon working electrode (WE), with an area of 0.0201 cm^2 purchased from BASi, a platinum wire purchase from BASi

which acted as a counter electrode (CE) and Ag/AgCl kept in 3 M NaCl also from BASi was the reference electrode (RE). The analytical grade argon gas was used for degassing all the cell solutions was purchased from Afrox Company, South Africa. Alumina polishing pads and powder (0.05, 0.3 and 1.0 μm) used to clean the working electrode surface were purchased from Buehler, Illinois, USA.

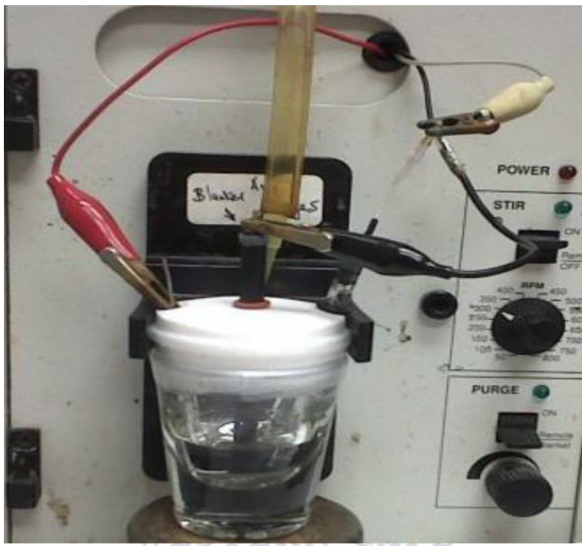

Figure 2.2: A three–way electrode electrochemical workstation for performing characterization of CV, SWV and EIS.

Cyclic voltammetry (CV) is the most flexible electroanalytical technique for the study of electroactive species. Its flexibility allows ease of measurement in the extensive use of CV in the field of electrochemistry. It is a technique capable of acquiring qualitative information about electrochemical reactions that occur in the reaction. It also observes the behaviour of redox potentials of electroactive species over a wide potential range. [45]. Cyclic voltammetry can be used to define the reversibility and irreversibility of electrochemical reactions. Figure 2.3 represent a graph of a reversible cyclic voltamogram redox system

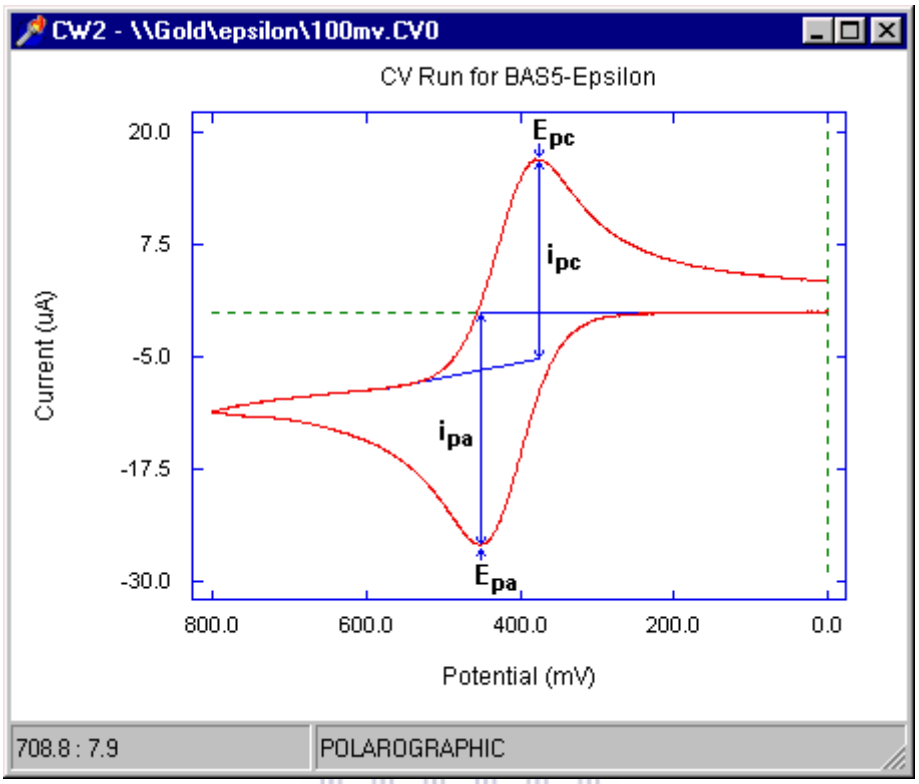

Figure 2.3: A representation of a graph illustating a reverse cyclic voltametry system [34]

Important parameters of CV are labelled in Figure 2.3 and are the magnitudes of anodic peak current (I_{pa}), cathodic peak current (I_{pc}), and the anodic peak potential together with cathodic peak potential (E_{pa} & E_{pc}) respectively and these peaks can be utilized further to understand the kinetics of the working electrode [46].

Reversible system: A reversible system is defined as a system in which both redox species exchange electrons with the electrode. For a reversible system, the peak current is given by the Randel-Sevčik equation:

$I_p = (2.6x10^5)\, n^{3/2} A C D^{1/2} v^{1/2}$

Where Ip is the peak current in amperes, n is the number of electrons, A is the electrode area in cm^2 C is the concentration in mol/cm^3, D is the diffusion coefficient in cm^2/s and v is the scan rate in V/s. The current is directly proportional to the concentration and increases with the root of the scan rate. The ratio of the reverse to forward peak current is I_{pr}/I_{pf}, a unity for a reversible couple. This peak ratio can be affected by chemical reactions coupled to redox reactions. The position of the peaks on the potential axis (E_p) is related to the formal potential of the redox reactions. The formal potential for a reversible couple is centred between E_{pa} and E_{pc}.

$\Delta E_p = E_{pa} - E_{pc} = 0.059/n$

Where ΔE_p represent peak-to-peak separation in mV. While the formal potential (E^0), can be expressed as the average of two peak potentials:

$\Delta E^0 = (E_{pa} + E_{pc})/2$

Irreversible system: the individual peaks are reduced in size and widely separated. The peak potentials depend on the potential scan rate as they shift away from the formal potential as the scan rate increases. The peak current for irreversible system is defined by:

$I_p = (2.6x10^5)a^{1/2}\, n^{3/2}ACD^{1/2}v^{1/2}$

Where I_p is the peak potential, α is the transfer coefficient, n is the number of electrons involved in charge transfer step, A is the area of the working electrode, C is the concentration of the redox species and D is the diffusion coefficient. Therefore E_p occurs at potentials higher than E_o, with E_o related to *ko* (standard rate constant) and α. For irreversible process, the relationship between *Eo* and *Ep* can be expressed by the equation below [47].

$E_p - E^0 = 48/an$

Quasi-reversible: A quasi-reversible system is determined by intermediate rates of electron transfer on the electrode surface. At very low scan rates quasi-reversible process appears to be fully reversible. Even thou the scan rate increases the kinetics of the electron transfer, the

process will not be fast enough to maintain (Nernstian) equilibrium [48]. As a result when the process is quasi-reversible the following observations can be made:

a) The separation of the forward and reverse peaks (ΔE_p) is larger than the value of 56/n mV associated with reversible process at 25 ºC.

b) The peaks broaden as the scan rate increases and the peak current is below the value expected for a reversible electron transfer process.

c) The magnitude of the peak current ratio (i_p^{ox}/i_p^{red}) is equal to unity for a quasi-reversible system when $\alpha = 0.5$

2.7.2. Electrochemical Impedance (EIS)

Impedance spectroscopy is an effective technique for examining the features of chemically-modified electrodes and for understanding electrochemical reaction rates. Impedance is the totally complex resistance encountered when a current flows through a circuit made up of combinations of resistors, capacitors, or inductors. An electrochemical transformation that occurs at the electrode–solution interface can be modelled using components of the electronic equivalent circuit that correspond to the experimental impedance spectra. An impedance graph include the double-layer capacitance (C_d), the ohmic resistance of the electrolyte solution (R_s), the electron transfer resistance (R_p), and the Warburg impedance (W) resulting from the diffusion of ions from the bulk solution to the electrode surface. The impedance of the interface, derived by application of Ohm's law, consists of two parts, a real number (Z') and an imaginary one, (Z) and this is shown in Figure 2.4 [49]

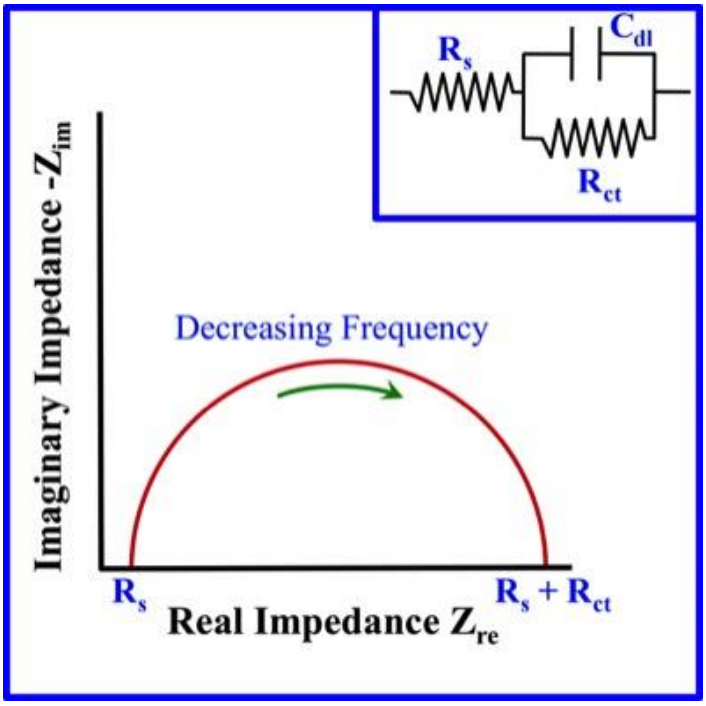

Figure 2.4 An illustration of the different components of EIS [34]

2.8. Spectroscopic techniques

2.8.1. Ultraviolet-visible spectroscopy (UV-VIS)

Ultraviolet and visible (UV-vis) absorption spectroscopy is a technique that measures the attenuation of beam of light when it passes through a sample surface. Absorption measurements can be at a single wavelength or even at extended spectral range. Uv-vis utilizes light in the visible region (200 – 800 nm) and ultraviolet region (185 – 400 nm) for the quantitative determination of different analytes in solution. In this study UV-vis was performed using Nicolet Evolution 100 spectrometer (Thermo Electron Cooperation) at room temperature. The basic principle of UV-vis spectroscopy is that the absorbance of the solution increases with the effect of the beam increase. Absorbance is directly proportional to the path length and the concentration of the absorbing species, and this is explained by Beer's law:

$A = \mathcal{E} l c$

Where is the absorbance, Ɛ is the greek letter also known as epslon, ⌊ is the path length of the solution that light passes through (cm) and c is the concentration (mol.dm^{-3}). The law states that there is a linear relationship between absorbance and path length at a fixed concentration. [50]. The linear factor of Beer-Lambert law is limited by chemical instrument factors hence there's a difference in the absorption state of different elements.

When a particular substance absorbs this light it undergoes an electron transition whereby a valence electron gets excited form ground state to excited state at which they go from lower energy level to higher energy level. [51]. These electronic transitions can provide the properties of substances such as structure and colour and energy associated with each transition as shown in Figure 2.5.

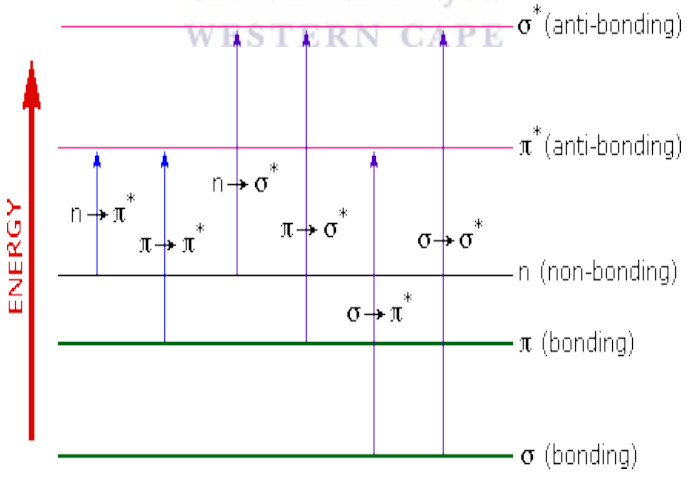

Figure 2.5: Different energy levels and types of electronic transitions [33].

2.8.2. Fourier transform infrared spectroscopy (FTIR)

Infra-red spectroscopy is the study of the interaction and relationship between matter and electromagnetic fields in the infra-red region. It is a powerful tool that provides information about the chemical composition of a sample. Liquids, solutions, pastes, powders, films, fibres, gases and surfaces can all be examined with a sensible choice of sampling technique [52]. Fourier transform infrared spectroscopy (FTIR) is a technique which is used to obtain an infrared spectrum of absorption, emission, photoconductivity or Raman scattering of a solid, liquid or gas. An FTIR spectrometer simultaneously collects high spectral resolution data over a wide spectral range. It is an effective analytical instrument that is able to detect functional groups and characterize polar covalent bonding information. [53]. In this study, liquid and solid FTIR were recorded on spectrum 100 FTIR spectrometer (PerkinElmer, USA) in a region of 400 to 4000 cm^{-1}.

2.9. Microscopic techniques

2.9.1. High resolution transmission electron microscopy (HRTEM)

High-resolution transmission electron microscopy (HRTEM) is an imaging mode of the transmission electron microscope (TEM) that allows direct imaging of the atomic structure of the sample. HRTEM is a powerful tool to study properties of materials on the atomic scale, such as semiconductors, metals, nanoparticles and sp^2-bonded carbon (e.g. graphene, C nanotubes) [54]. In HRTEM the image and corresponding diffraction pattern from the same part of the sample, the concentration of the elements in the sample as well as the mapping of the elements in the same region of the sample can be obtained through the analysis of the image and the corresponding diffraction as a results useful information can be obtained about the surface morphology, grain size, precipitates and their orientation on the matrix and on the

appearance of the superstructure [55]. For this study, HRTEM images were taken using Tecnai G2 F20X-Twin MAT 200kV Field Emission Transmission Microscopy from FEI (Eindhoven, Netherlands).

2.9.2. High resolution scanning electron microscopy (HRSEM)

High resolution scanning electron microscopy is a microscopic technique that uses the interaction between an electron beam and the atoms of the targeted sample to produce an image through the emission of different signals. The interaction between an electron beam and the atoms of the targeted sample serves as an important principle for scanning electron microscopy [56]. HRSEM images are obtained by a thin high energy electron beam which is focused over a sample and swept in a raster across the sample surface. An interaction occurs between the incident electron beam and sample atoms as the beam goes through the sample, causing the emission of different signals. The depth of penetration is determined by the accelerating voltage of the beam and the density of the sample, and ranges from a few nanometres to a few micrometres. Different interactions yield signals (secondary electrons, backscattered electrons and x-rays), each with different characteristics. As for surface topography, secondary and backscattered electrons are of great interest. This is because of the characteristic x-rays emitted as a result of electron bombardment, are element specific and permit both qualitative and quantitative elemental analysis in electron probe microanalysis. [57]. HRSEM images in this study were taken using Zess Auriga 1-20kV Field Emission Scanning Microscopy from FEI (Eindhoven, Netherlands).

References

1. Grossman, R.F., Hsueh, P.R., Gillespie, S.H. and Blasi, F., 2014. Community-acquired pneumonia and tuberculosis: differential diagnosis and the use of fluoroquinolones. International Journal of Infectious Diseases, 18, pp.14-21.
2. Hassanein, H.A. and Elbadry, M.I., 2016. Selective immunoglobulin M deficiency in an adult with miliary tuberculosis: A clinically interesting coexistence. A case report and review of the literature. International journal of mycobacteriology, 5(1), pp.106-110.
3. Chiu, N.C., Wu, S.J., Chen, M.R., Peng, C.C., Chang, L., Chi, H. and Lin, C.Y., 2016. A Mysterious Effusion: Tuberculous Pericarditis. The Journal of pediatrics, 174, pp.271-271.
4. Sabooni, K., Khosravi, M.H., Pirmohammad, H., Afrasiabian, S., Moghbel, N., Shahverdi, E., Konjedi, M.A. and Shahverdi, A., 2015. Tuberculosis peritonitis with features of acute abdomen in HIV infection. International journal of mycobacteriology, 4(2), pp.151-153.
5. Saavedra, J.S., Urrego, S., Toro, M.E., Uribe, C.S., García, J., Hernández, O., Arango, J.C., Pérez, Á.B., Franco, A., Vélez, I.C. and del Corral, H., 2016. Validation of Thwaites Index for diagnosing tuberculous meningitis in a Colombian population. Journal of the Neurological Sciences, 370, pp.112-118.
6. Pathakumari, B., Prabhavathi, M., Anbarasu, D., Paramanandhan, P. and Raja, A., 2016. Dynamic IgG antibody response to immunodominant antigens of M. tuberculosis for active TB diagnosis in high endemic settings. Clinica Chimica Acta, 461, pp.25-33.
7. Kowada, A., 2011. Cost-effectiveness of interferon-γ release assay versus chest X-ray for tuberculosis screening of employees. American journal of infection control, 39(10), pp.e67-e72.

8. Reeves, S.A. and Noble, R.C., 1983. Ineffectiveness of annual chest roentgenograms in tuberculin skin test-positive hospital employees. American journal of infection control, 11(6), pp.212-216.
9. Simmons, J.A., 2004. Risk of cancer from diagnostic X-rays. The Lancet, 363(9424), pp.1908-1909.
10. Kowada, A., Deshpande, G.A., Takahashi, O., Shimbo, T. and Fukui, T., 2010. Cost effectiveness of interferon-gamma release assay versus chest X-ray for tuberculosis screening of BCG-vaccinated elderly populations. Molecular diagnosis & therapy, 14(4), pp.229-236.
11. Mathew, P., Kuo, Y.H., Vazirani, B., Eng, R.H. and Weinstein, M.P., 2002. Are three sputum acid-fast bacillus smears necessary for discontinuing tuberculosis isolation? Journal of clinical microbiology, 40(9), pp.3482-3484.
12. Andersen, P., Munk, M.E., Pollock, J.M. and Doherty, T.M., 2000. Specific immune-based diagnosis of tuberculosis. The Lancet, 356(9235), pp.1099-1104.
13. Pandey, S., Congdon, J., McInnes, B., Pop, A. and Coulter, C., 2017. Evaluation of the GeneXpert MTB/RIF assay on extrapulmonary and respiratory samples other than sputum: a low burden country experience. Pathology, 49(1), pp.70-74.
14. Boehme, C.C., Nabeta, P., Hillemann, D., Nicol, M.P., Shenai, S., Krapp, F., Allen, J., Tahirli, R., Blakemore, R., Rustomjee, R. and Milovic, A., 2010. Rapid molecular detection of tuberculosis and rifampin resistance. New England Journal of Medicine, 363(11), pp.1005-1015.
15. Pantoja, A., Fitzpatrick, C., Vassall, A., Weyer, K. and Floyd, K., 2013. Xpert MTB/RIF for diagnosis of tuberculosis and drug-resistant tuberculosis: a cost and affordability analysis. European Respiratory Journal, 42(3), pp.708-720.

16. Hoza, A.S., Mfinanga, S.G. and König, B., 2015. Anti-TB drug resistance in Tanga, Tanzania: A cross sectional facility-base prevalence among pulmonary TB patients. Asian Pacific journal of tropical medicine, 8(11), pp.907-913.
17. Pan, L., Jia, H., Liu, F., Sun, H., Gao, M., Du, F., Xing, A., Du, B., Sun, Q., Wei, R. and Gu, S., 2015. Risk factors for false-negative T-SPOT. TB assay results in patients with pulmonary and extra-pulmonary TB. Journal of Infection, 70(4), pp.367-380.
18. Pai, M., 2010. Spectrum of latent tuberculosis—existing tests cannot resolve the underlying phenotypes. Nature Reviews Microbiology, 8(3), pp.242-242.
19. Mody, V.V., Siwale, R., Singh, A. and Mody, H.R., 2010. Introduction to metallic nanoparticles. Journal of Pharmacy and Bioallied Sciences, 2(4), p.282.
20. Salata, O.V., 2004. Applications of nanoparticles in biology and medicine. Journal of nanobiotechnology, 2(1), p.3.
21. Dobson, J., 2006. Gene therapy progress and prospects: magnetic nanoparticle-based gene delivery. Gene therapy, 13(4), pp.283-287.
22. Khan, A.K., Rashid, R., Murtaza, G. and Zahra, A., 2014. Gold nanoparticles: synthesis and applications in drug delivery. Tropical journal of pharmaceutical research, 13(7), pp.1169-1177.
23. Gou, X.C., Liu, J. and Zhang, H.L., 2010. Monitoring human telomere DNA hybridization and G-quadruplex formation using gold nanorods. Analytica chimica acta, 668(2), pp.208-214.
24. Pacławski, K., Streszewski, B., Jaworski, W., Luty-Błocho, M. and Fitzner, K., 2012. Zinc oxide formation via zinc nitrate complex ions reduction with glucose in the batch and in the flow microreactor systems. Colloids and Surfaces A: Physicochemical and Engineering Aspects, 413, pp.208-215.

25. Venugopal, K., Rather, H.A., Rajagopal, K., Shanthi, M.P., Sheriff, K., Illiyas, M., Rather, R.A., Manikandan, E., Uvarajan, S., Bhaskar, M. and Maaza, M., 2017. Synthesis of silver nanoparticles (Ag NPs) for anticancer activities (MCF 7 breast and A549 lung cell lines) of the crude extract of Syzygium aromaticum. Journal of Photochemistry and Photobiology B: Biology, 167, pp.282-289.
26. Pokpas, K., Zbeda, S., Jahed, N., Mohamed, N., Baker, P.G. and Iwuoha, E.I., 2014. Electrochemically reduced graphene oxide pencil-graphite in situ plated bismuth-film electrode for the determination of trace metals by anodic stripping voltammetry. Int. J. Electrochem. Sci, 9, pp.736-759.
27. Sharma, P., Tuteja, S.K., Bhalla, V., Shekhawat, G., Dravid, V.P. and Suri, C.R., 2013. Bio-functionalized graphene–graphene oxide nanocomposite based electrochemical immunosensing. Biosensors and Bioelectronics, 39(1), pp.99-105.
28. Bunch, J.S., Van Der Zande, A.M., Verbridge, S.S., Frank, I.W., Tanenbaum, D.M., Parpia, J.M., Craighead, H.G. and McEuen, P.L., 2007. Electromechanical resonators from graphene sheets. Science, 315(5811), pp.490-493.
29. Zbeda, S., Pokpas, K., Titinchi, S., Jahed, N., Baker, P.G. and Iwuoha, E.I., 2013. Few-layer Binder Free Graphene Modified Mercury Film Electrode for Trace Metal Analysis by Square Wave Anodic Stripping Voltammetry. Int. J. Electrochem. Sci, 8, pp.11125-11141.
30. Yang, H., Li, F., Shan, C., Han, D., Zhang, Q., Niu, L. and Ivaska, A., 2009. Covalent functionalization of chemically converted graphene sheets via silane and its reinforcement. Journal of Materials Chemistry, 19(26), pp.4632-4638.
31. Galashev, A.E. and Galasheva, A.A., 2015. Mercury removal from graphene by bombardment with xenon clusters: Computer simulation. High Energy Chemistry, 49(5), pp.347-351.

32. Cruz, H.J., Rosa, C.C. and Oliva, A.G., 2002. Immunosensors for diagnostic applications. Parasitology research, 88, pp.S4-S7.

33. Ricci, F., Adornetto, G. and Palleschi, G., 2012. A review of experimental aspects of electrochemical immunosensors. Electrochimica Acta, 84, pp.74-83.

34. Azam, M.S., RAHMAN, M.R.T., LOU, Z., TANG, Y., RAQIB, S.M. and JOTHI, J.S., 2014. Review: Advancements and application of immunosensors in the analysis of food contaminants. Nusantura Bioscience, 6(2), pp.186-195.

35. Conneely, G., Aherne, M., Lu, H. and Guilbault, G.G., 2007. Development of an immunosensor for the detection of testosterone in bovine urine. Analytica chimica acta, 583(1), pp.153-160.

36. Ko, P. Y., Lin, S. D., Tu, S. T., Hsieh, M. C., Su, S. L., Hsu, S. R., & Chen, Y. C. (2015). High diabetes mellitus prevalence with increasing trend among newly-diagnosed tuberculosis patients in an Asian population: A nationwide population-based study. Primary care diabetes.

37. Zumla, A. Hafner, R., Lienhardt, C., Hoelscher, M., Nunn A.(2012). Advancing the development of tuberculosis therapy Nat Rev Drug Discov, 11 , pp. 171–172.

38. World Health Organization, 2015. Global tuberculosis report 2015. World Health Organization.

39. Kumar, S., Pai, A.G., Tungenwar, P.N. and Bhandarwar, A.H., 2017. Isolated primary tuberculosis of spleen—A rare entity in the immuno-competent patient. International journal of surgery case reports, 30, pp.93-96.

40. Phillips, P.P., Gillespie, S.H., Boeree, M., Heinrich, N., Aarnoutse, R., McHugh, T., Pletschette, M., Lienhardt, C., Hafner, R., Mgone, C. and Zumla, A., 2012. Innovative trial designs are practical solutions for improving the treatment of tuberculosis. Journal of infectious diseases, 205(suppl_2), pp.S250-S257.

41. Chinnasamy T, Senthilkumar K, Periyakaruppan A (2011). Specific detection of Mycobacterium sp. genomic DNA using dual labeled gold nanoparticle based electrochemical immunosensor 10.1016/2011.05
42. Maserumule, M.C., 2013. The development of aptamer-based probes for the detection of TB antigens ESAT-6. CFP-10 potential TB diagnostic tools (Doctoral dissertation, University of Cape Town).
43. Renshaw, P.S., Panagiotidou, P., Whelan, A., Gordon, S.V., Hewinson, R.G., Williamson, R.A. and Carr, M.D., 2002. Conclusive Evidence That the Major T-cell Antigens of the Mycobacterium tuberculosis Complex ESAT-6 and CFP-10 Form a Tight, 1: 1 Complex and Characterization of the Structural Properties of ESAT-6, CFP-10, and the ESAT-6• CFP-10 Complex IMPLICATIONS FOR PATHOGENESIS AND VIRULENCE. Journal of Biological Chemistry, 277(24), pp.21598-21603.
44. Feng, T.T., Shou, C.M., Shen, L., Qian, Y., Wu, Z.G., Fan, J., Zhang, Y.Z., Tang, Y.W., Wu, N.P., Lu, H.Z. and Yao, H.P., 2011. Novel monoclonal antibodies to ESAT-6 and CFP-10 antigens for ELISA-based diagnosis of pleural tuberculosis. The International Journal of Tuberculosis and Lung Disease, 15(6), pp.804-810.
45. Bond, A.M., 2002. Broadening electrochemical horizons: principles and illustration of voltammetric and related techniques. Oxford University Press on Demand.
46. JO, M.B., 1993. KSUM, Surface Electrochemistry—A Molecular Level Approach.
47. Kissinger, P.T. and Heineman, W.R., 1983. Cyclic voltammetry. J. Chem. Educ, 60(9), p.702.
48. Bard, A.J., Faulkner, L.R., Leddy, J. and Zoski, C.G., 1980. Electrochemical methods: fundamentals and applications (Vol. 2). New York: Wiley.

49. Mann, M.A., Helfrick Jr, J.C. and Bottomley, L.A., 2014. Diagnostic Criteria for the Characterization of Quasireversible Electron Transfer Reactions by Cyclic Square Wave Voltammetry. Analytical chemistry, 86(16), pp.8183-8191.
50. Mirceski, V., Gulaboski, R., Lovric, M., Bogeski, I., Kappl, R. and Hoth, M., 2013. Square-Wave Voltammetry: A Review on the Recent Progress. Electroanalysis, 25(11), pp.2411-2422.
51. Mirceski, V., Gulaboski, R., Lovric, M., Bogeski, I., Kappl, R. and Hoth, M., 2013. Square-Wave Voltammetry: A Review on the Recent Progress. Electroanalysis, 25(11), pp.2411-2422.
52. MARTÍNEZ, M.C., 2017. Caracterización de la morfología y la interacción con el agua de hidrogeles inyectables de gelatina y ácido hialurónico para ingeniería tisular.
53. Klamt, A., 1996. Calculation of UV/Vis spectra in solution. The Journal of Physical Chemistry, 100(9), pp.3349-3353.
54. Baker, M.J., Gazi, E., Brown, M.D., Shanks, J.H., Gardner, P. and Clarke, N.W., 2008. FTIR-based spectroscopic analysis in the identification of clinically aggressive prostate cancer. British journal of cancer, 99(11), pp.1859-1866.
55. Gazi, E., Baker, M., Dwyer, J., Lockyer, N.P., Gardner, P., Shanks, J.H., Reeve, R.S., Hart, C.A., Clarke, N.W. and Brown, M.D., 2006. A correlation of FTIR spectra derived from prostate cancer biopsies with Gleason grade and tumour stage. European urology, 50(4), pp.750-761.
56. Tonejc, A., Djerdj, I. and Tonejc, A., 2001, January. High-resolution electron microscopy (HRTEM) image processing analysis of defects and grain boundaries in ball-milled ZrO2 and ZrO2-Y2O3 powders. In The Conference on Modern Microscopical Methods.

57. Tonejc, A., 1999. High resolution transmission electron microscopy (HRTEM): image processing analysis of defects and grain boundaries in nanocrystalline materials. Acta Chim Slov, 46(3), pp.435-461.

58. Wells, O.C. and Joy, D.C., 2006. The early history and future of the SEM. Surface and interface analysis, 38(12-13), pp.1738-1742.

Chapter 3

Experimental methods

This chapter gives an overview of all the chemicals and experimental methods used throughout the project. The outlined procedures for stock solution, preparation of buffer solutions and detailed experimental procedures are all illustrated in this chapter. This chapter also discusses and describes the techniques used for the characterization of green synthesised ZnO NPs and Ag NPs, the chemical synthesis of GO, and finally the nanocomposite Ag NPs/ GO and ZnO NP/ GO.

3.1. Reagents and materials

Most of the chemicals used in this study were of analytical grade purchased from Sigma Aldrich, South Africa. This includes graphite powder, sulfuric acid 99.99% (H_2SO_4), potassium permanganate 99% (KM_nO_4), Hydrogen peroxide (H_2O_2), Hydrochloric acid (HCl), sodium borohydride ($NaBH_4$), silver nitrate 99.8% ($AgNO_3$) and zinc nitrate ($Zn(NO_3)_2.6H_2O$). The reaction medium, pH 7.4, 0.1 M phosphate buffer was prepared from sodium phosphate dibasic dihydrate ($HNa_2O_4P.2H_2O$) (≥99.5%) and sodium phosphate monobasic dihydrate ($H_2NaO_4P.2H_2O$) (≥99%) that were purchased from Sigma Aldrich. Additionally fresh pear fruits, strawberries and green tea were purchased from Checkers Supermarket in Brackenfell. Furthermore recombinant ESAT-6 antibody - protein ab124574 and recombinant CFP-10 antibody and protein were purchased from Biocom Biotech, South Africa. De-ionized ultra-purified water used throughout these experiments was prepared with a Milli-Q water purification system.

3.2. Sample preparation

0.10 M phosphate buffer solution (PBS), pH 7.40 was prepared using NaH_2PO_4 and Na_2HPO_4 and it was used as an electrolyte solution throughout the course of this study unless where stated otherwise where acetate buffer was used. The prepared PBS electrolyte solutions were kept refrigerated at 4^0C when not in use.

3.3. Experimental methods

3.3.1. Green synthesis of silver nanoparticles (Ag NPs)

Silver nanoparticles were prepared using a green synthesis method catalysed by the use of pear juice extract. The pear was cut into small pieces and washed thoroughly with running tap water. 100 g of small cut pears was placed into 200 ml of deionized water and heated for 1 hour at 80 ^{0}C. The extract was then filtered using filter paper, and the filtrate was later used as the reducing agent for the synthesis of Ag NPs.

Silver Nitrate ($AgNO_3$) was obtained from Sigma Aldrich, South Africa. Synthesis of Ag NPs was prepared by using 20 ml of the pear extract in 180 ml of 0.1 M aqueous Ag NO_3 solution. The mixture was stirred and heated at 80 ^{0}C for 1 hour. A brown red colour was observed which confirmed the synthesis of Ag NPs.

3.3.2. Green synthesis of zinc oxide nanoparticles (ZnO NPs)

Zinc oxide nanoparticles were prepared using a green synthesis method where a mixture of strawberries (40 mg) and green tea extract (10 ml) was used to catalyse the synthesis. Strawberries (40 mg) were collected and washed with distilled water, then chopped into small pieces and boiled for 1 hour at 80 ^{0}C while the tea (10 ml) was only boiled at 70 ^{0}C for an hour.

Zinc nitrate (7 g) was mixed with 30 ml of distilled water and then 10 ml of each extract. This was then boiled for an hour with continuous stirring at 75 ^{0}C. A brownish solution was observed which was then washed 3 times with distilled water and phosphate buffer after centrifuged; a greyish-white colour was observed which confirms the formation of nanoparticles.

3.3.3. Synthesis of Graphene Oxide (GO)

Graphene oxide was synthesized using the Hummer method. 50 ml of sulfuric acid was added onto 2 g of graphite powder and stirred at room temperature for 30 minutes. The solution was then placed in an ice bath where 7 g of potassium permanganate was added gradually over a constant stirring for 30 minutes. The solution was then allowed to reach room temperature prior to being placed into a water bath set at 35 ^{0}C and left to stir for 2 hours. The solution was then returned to ice bath for half an hour where 150 ml of distilled water was added prior to the addition of approximately 5 ml hydrogen peroxide until effervescence ceased. The solution was left to stir overnight at room temperature after which it was filtered followed by 3 successful acid washes and then by distilled water. The resulting product was dried for 48 hours in a vacuum oven. The prepared graphite oxide (10 mg) was then exfoliated in 10 ml of acetate buffer (p H 4.6) by ultra-sonication for 1 hour to give a graphene oxide solution and then the solution was air dried in the oven for 48 hours to get powdered GO.

3.3.4. Synthesis of graphene-silver nanoparticle composite (Ag NPs/GO)

The composite of Ag NPs/GO was prepared by mixing 0 .1 M aqueous $AgNO_3$ (3 g) solution with 10 ml of GO which was previously synthesized as per the synthesis method described above. The reaction mixture was stirred for 30 minutes at room temperature before the slow

addition of 1 ml of the reducing agent $NaBH_4$ followed by vigorous stirring. A colour change of dark brown from grey occurred and the reaction mixture was further stirred at room temperature for another 5 hours for the complete synthesis of the nanocomposites.

3.3.5. Synthesis of graphene-zinc oxide nanoparticle composite (Zn NPs/GO)

Graphite (4 mg) was dispersed in 40 ml of di-methyl formamide (DMF) and ultra-sonicated for 30 minutes to form GO. Then 0.2 g of zinc nitrate was added to the GO solution then heated to 95 ^{0}C. The mixture was left stirring for 5 hours and then washed several times with water followed by ethanol in order to remove any unreacted product. The product was then vacuum-dried at 60 ^{0}C for 12 hours.

3.3.6. Development of Immunosensors

The immunosensor was developed by drop-coating 40 µl of 1-ethyl-3-(3-dimethylaminopropyl) carbodiimide (EDC) and N-hydroxysuccinimide (NHS) into a glassy carbon electrode at room temperature then left for 5 minutes. After that 10 µl of ESAT-6 or and CFP-10 was immobilised onto NHS/EDC followed by addition of Ag NPs/GO or ZnO NPs/GO solution and were allowed to dry overnight in the fridge at -2^0 C. The electrode was then washed with 10 µl of 6-mercapto-hexanol and bis (trimethylsilyl) acetamide (BSA) to remove excess nanoparticles on the electrode. The electrode was then be returned to the fridge for an hour before being characterised using CV and EIS.

References

1. Bond, A.M., 2002. *Broadening electrochemical horizons: principles and illustration of voltammetric and related techniques*. Oxford University Press on Demand.

2. JO, M.B., 1993. KSUM, Surface Electrochemistry—A Molecular Level Approach.

3. Kissinger, P.T. and Heineman, W.R., 1983. Cyclic voltammetry. *J. Chem. Educ*, *60*(9), p.702.

4. Bard, A.J., Faulkner, L.R., Leddy, J. and Zoski, C.G., 1980. *Electrochemical methods: fundamentals and applications* (Vol. 2). New York: Wiley.

5. Mann, M.A., Helfrick Jr, J.C. and Bottomley, L.A., 2014. Diagnostic Criteria for the Characterization of Quasireversible Electron Transfer Reactions by Cyclic Square Wave Voltammetry. *Analytical chemistry*, *86*(16), pp.8183-8191.

6. Mirceski, V., Gulaboski, R., Lovric, M., Bogeski, I., Kappl, R. and Hoth, M., 2013. Square Wave Voltammetry: A Review on the Recent Progress. *Electroanalysis*, *25*(11), pp.2411-2422.

7. Mirceski, V., Gulaboski, R., Lovric, M., Bogeski, I., Kappl, R. and Hoth, M., 2013. Square Wave Voltammetry: A Review on the Recent Progress. *Electroanalysis*, *25*(11), pp.2411-2422.

8. Perkampus, H.H., 1992. *UV-VIS Spectroscopy and its Applications* (pp. 220-22). Berlin: Springer-Verlag.

9. Klamt, A., 1996. Calculation of UV/Vis spectra in solution. *The Journal of Physical Chemistry*, *100*(9), pp.3349-3353.

10. Baker, M.J., Gazi, E., Brown, M.D., Shanks, J.H., Gardner, P. and Clarke, N.W., 2008. FTIR-based spectroscopic analysis in the identification of clinically aggressive prostate cancer. *British journal of cancer*, *99*(11), pp.1859-1866.

11. Gazi, E., Baker, M., Dwyer, J., Lockyer, N.P., Gardner, P., Shanks, J.H., Reeve, R.S., Hart, C.A., Clarke, N.W. and Brown, M.D., 2006. A correlation of FTIR spectra derived from prostate cancer biopsies with Gleason grade and tumour stage. *European urology*, *50*(4), pp.750-761.

12. Tonejc, A., Djerdj, I. and Tonejc, A., 2001, January. High-resolution electron microscopy (HRTEM) image processing analysis of defects and grain boundaries in ball-milled ZrO_2 and ZrO_2-Y_2O_3 powders. In *The Conference on Modern Microscopical Methods*.

13. Tonejc, A., 1999. High resolution transmission electron microscopy (HRTEM): image processing analysis of defects and grain boundaries in nanocrystalline materials. *Acta Chim Slov*, *46*(3), pp.435-461.

14. Wells, O.C. and Joy, D.C., 2006. The early history and future of the SEM. *Surface and interface analysis*, *38*(12-13), pp.1738-1742.

15. Nebel, M., Eckhard, K., Erichsen, T., Schulte, A. and Schuhmann, W., 2010. 4D shearforce-based constant-distance mode scanning electrochemical microscopy. *Analytical chemistry*, *82*(18), pp.7842-7848.

Chapter 4

Results and Discussion: Silver Nanoparticles

4.1. Introduction

Research on nanoparticles has been and still continues to be an area of interest in the scientific research, due to their wide variety of potential applications such as biomedical, optical, and electronic fields [1]. Synthesis of nanoparticles can be carried out by using various chemical and physical methods, even though use of some methods can be harmful due to the use of chemicals used which are often toxic, flammable, not easily disposable and have low production rate [2]. Thus new methods of synthesizing these nanoparticles to ensure that they are environmental friendly has to be implemented like using biological systems and plants for the synthesis of metal nanoparticles. Various microorganisms such as bacteria, fungi, and yeasts have been suggested as nano-factors for synthesizing metal nanoparticles of silver and various other nanoparticles. However, the use of plants and fruits for the fabrication of nanoparticles has also drawn the attention of researchers as they are rapid, low cost, eco-friendly and require a single step method [3]. It has been reported that the rate of reduction of metal ions using plants and fruits has been found to be much faster as compared to micro-organisms and stable formation of metal nanoparticles [4]. The synthesis of nanoparticles can be done both within the cells and outside the cells such as using leaf broth, sun dried leaves, fruits peel extract etc [4]. Additionally, silver nanoparticles are usually synthesized using fruits or boiled leaves since the shape and the size of the nanoparticles can be controlled easily by just changing the pH [5].

4.2. Spectroscopic techniques

4.2.1. Ultraviolet–visible spectroscopy (UV-Vis)

Ultraviolet–visible spectroscopy (UV-Vis) refers to absorption spectroscopy or reflectance spectroscopy. This means it uses light in the visible and adjacent (near-UV and near infrared [NIR]) ranges. The absorption or reflectance in the visible range directly affects the perceived colour of the chemicals involved in the sample being analysed.

In metal nanoparticles such as in silver, the conduction band and valence band lie very close to each other in which electrons move freely. These free electrons give rise to a surface plasmon resonance (SPR) absorption band [6], occurring due to the collective oscillation of electrons of silver nanoparticles in resonance with the light wave [7]. Basically, the electric field of an incoming wave induces a polarization of the electrons with respect to much heavier ionic core of silver nanoparticles. As a result a net charge difference occurs which it turns out to acts as a restoring force. This creates a dipolar oscillation of all the electrons with the same phase [8]. When the frequency of the electromagnetic field becomes resonant with the coherent electron motion, a strong absorption takes place, which is the origin of the observed colour. This absorption strongly depends on the particle size, dielectric medium and chemical surroundings [9]. Small spherical nanoparticles (< 20nm) exhibit a single surface plasmon band. For this study, the colour of the prepared silver nanoparticles was dark reddish brown, the distinctive colour of silver nanoparticles solution is due to the phenomenon known as plasmon absorbance. The incident light forms an oscillation in the conduction electron on the surface of the nanoparticles, then the collective oscillation of conduction electrons within metal nanoparticles and the surface plasmon resonance enables scattering and absorption of light at a particular frequency giving the nanoparticles a colour [9]. The UV/Vis absorption spectra of the

synthesized silver nanoparticles is shown in the Figure 4.1. The absorption peak (SPR) is obtained in the visible range at 448 nm which indicates the stability of silver nanoparticles [9].

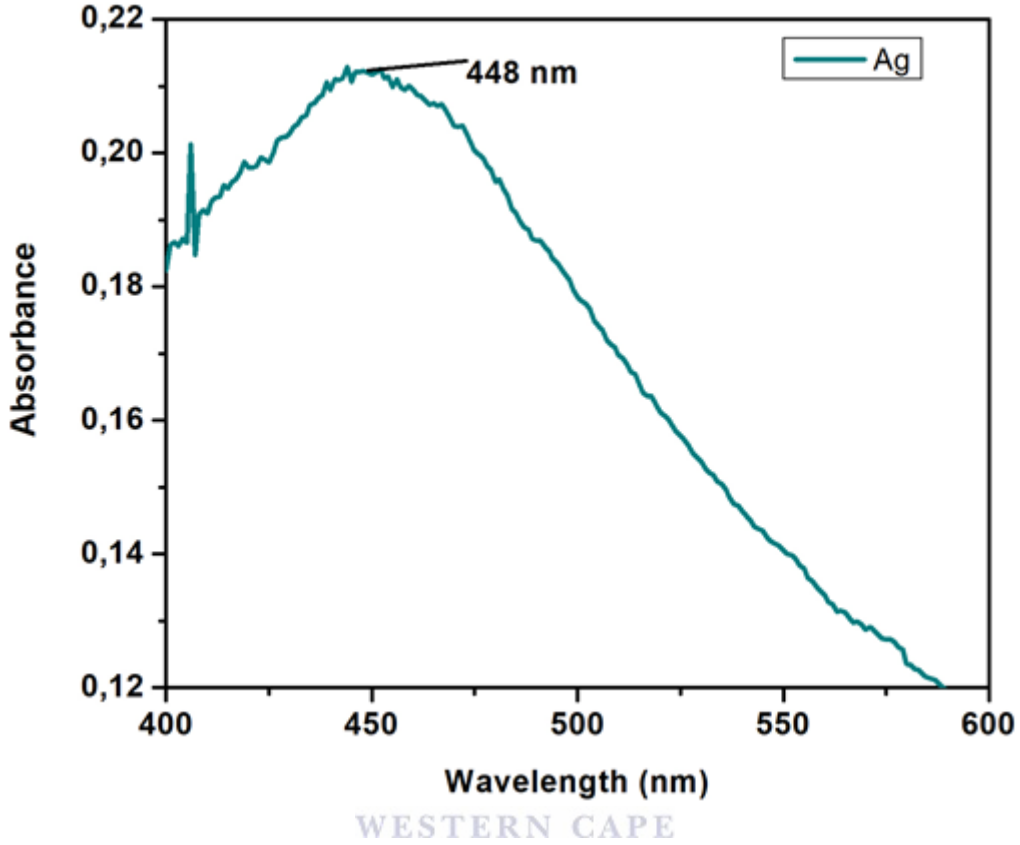

Figure 4.1: UV-VIS spectrum of green synthesized silver nanoparticles dispersed in ethanol.

4.2.2. Fourier Transform Infrared Spectroscopy (FTIR)

FTIR measurements were carried out to identify the possible biomolecules in the pear extract used during the green synthesis of silver nanoparticles. Pear extracts have shown to possess the presence of amines, alkaloids, steroids, rosins and antioxidants [10]. The absorption band observed at 612 cm^{-1} is due to the flavonoids while the band observed at 1054 cm^{-1} corresponds to C-Cl chloro moieties of stretching in the alkyl group. The strong intense peak at 1392 cm^{-1} corresponds to the C-N stretch vibrations of the amides groups found in antioxidants of the

pear extract [11]. The strong bands at 1074 cm^{-1} are due the linkage which suggests the presence of amines adsorbed at the surface of metal nanoparticle [12]. The very strong band at 1668 and 2093 cm^{-1} is due to C=C stretching in the aromatic ring confirming the presence of aromatic groups [13]. The absorption peak at 3389 cm^{-1} is due to O-H stretching of carboxylic groups in silver nanoparticles. FTIR spectroscopic studies have also showed that the pear fruit extract not only acts as reducing agent but as a stabilizer also at it which prevents the agglomeration of Ag NPs. The carbonyl group of amino acid residues has a strong binding ability with metal, suggesting the formation of a layer covering silver nanoparticles which act as a stabilizing agent to prevent agglomeration in the aqueous medium [14]. Figure 4.2 shows the FTIR structure of green synthesized Ag NPs.

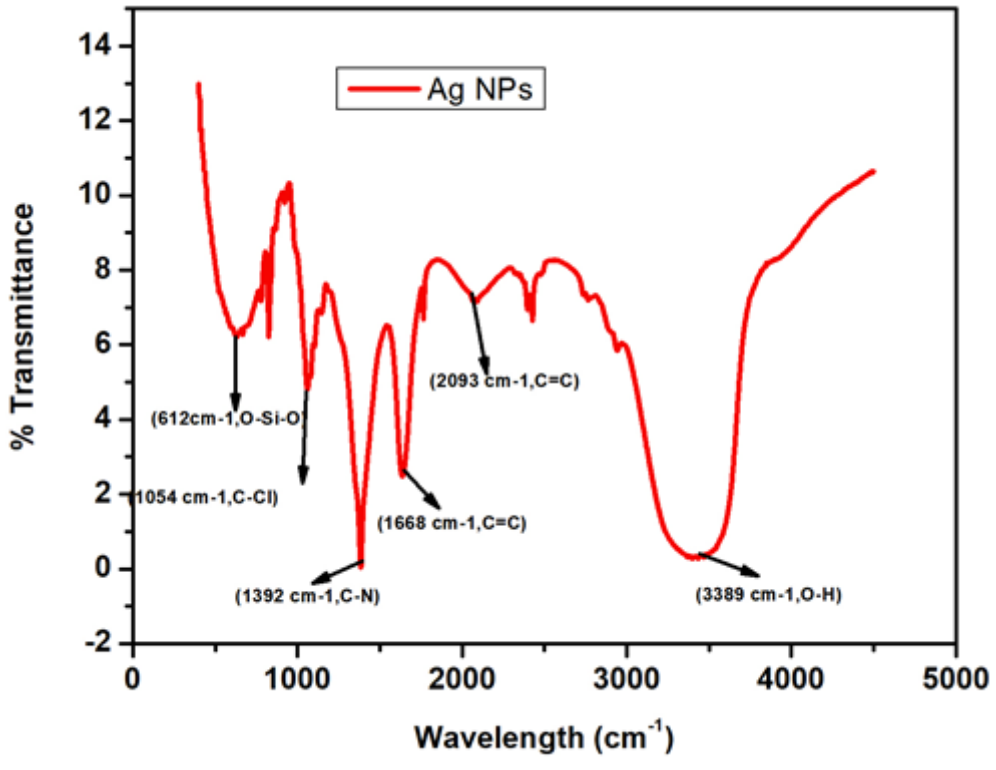

Figure 4.2: FTIR spectra of green synthesized Ag NPs.

4.3. Microscopic techniques

4.3.1. High resolution transmission electron microscopy (HR-TEM)

The shape and size of the resultant nanoparticles were elucidated with the help of HR-TEM Figure 4.3 (a). Aliquots of silver nanoparticle solution were placed on a carbon-coated copper grid and allowed to dry under high temperature conditions and HR-TEM images were recorded. The HR-TEM micrograph shows that the size of the nanoparticles was approximately 50 nm and were observed to be of spherical shape. These nanoparticles appear to have fabricated into very open, quasi-linear super structures rather than a dense closely packed fabrication [15]. The HR-TEM images also reveal that the nanoparticles are not in physical contact but are separated by uniform particle distance. This is due to these large-sized particles which aggregate two or more nanoparticles together which in turn result in the presence of excess amounts of reducing agents and the interactions between stabilizing molecules bound to the surface of particles and secondary reduction process on the surface of the preformed nuclei [16]. On the other hand Figure 4.3 (b) shows selected area of diffraction of the nanoparticles which shows that the nanoparticles are amorphous. Amorphous nanoparticles have the advantage of cooperating mechanism in enhancing dissolution rates due to nano size ranges as well as increasing super-saturation levels [17]. The particle size distribution of Ag NPs is shown in Figure 4.3 (c) below and the nanoparticles are found to be around 1.5 nm in diameter size.

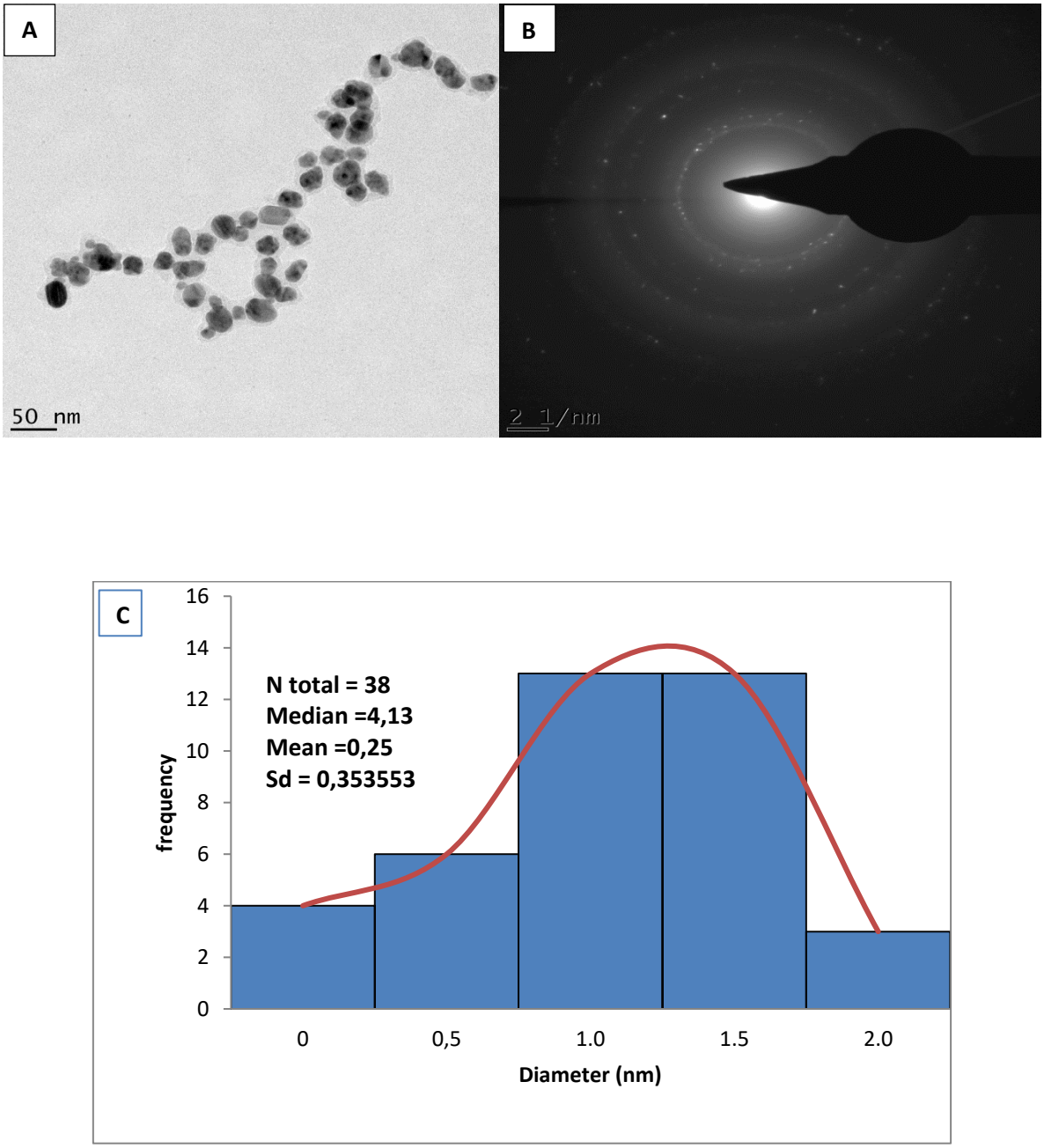

Figure 4.3 (A) HR-TEM image of Ag NPs, (B) SAED of Ag NPs and (C) particle size distribution.

4.3.2. High resolution scanning electron microscopy (HR-SEM)

The HR-SEM images of Ag NPs are shown in Figure 4.4 (A). The surface morphology of silver nanoparticles shows round and spherical shape of the nanoparticles which complements the findings in the HR-TEM image. Nanoparticles of that nature are usually found to be 20-50 nm in size[18]. Additionally, Figure 4.4 (B) shows the EDS analysis of Ag NPs which confirms that indeed Ag NPs synthesis were successful synthesized.

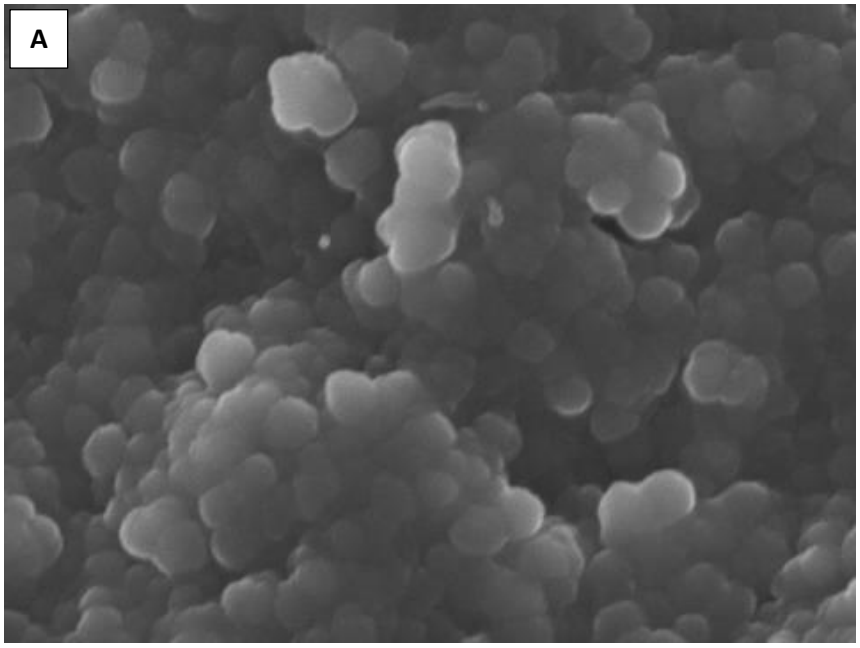

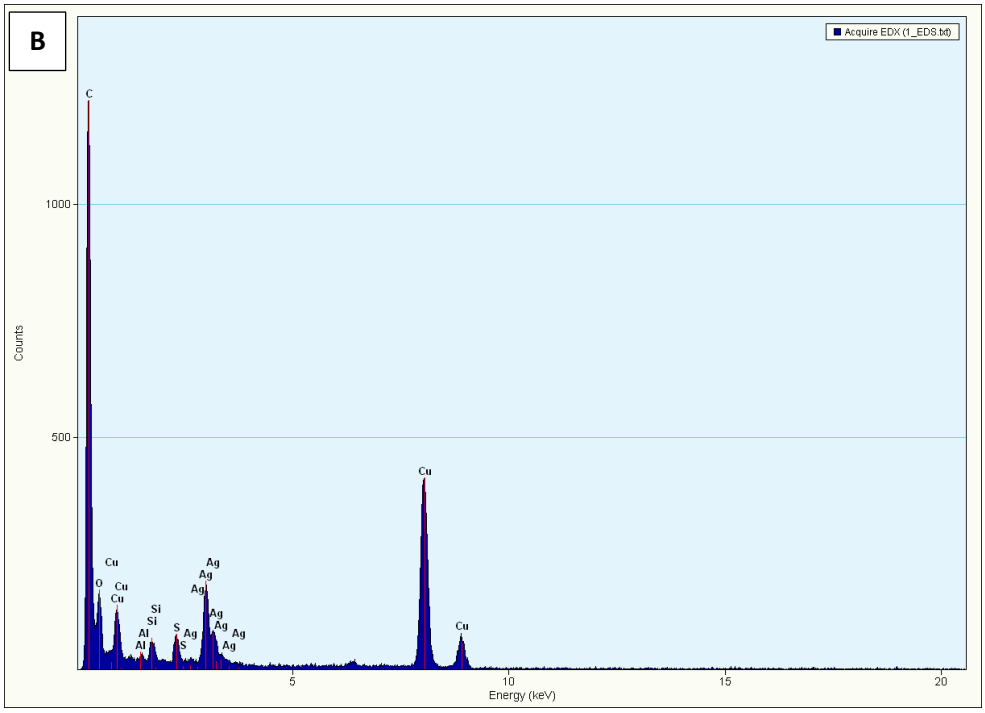

Figure 4.4 (A) illustrates the HR-SEM image of Ag NPs and (B) shows the EDS of Ag NPs.

4.4. Electrochemistry of green synthesized silver nanoparticles (Ag NPs)

4.4.1. Cyclic voltammetry (CV)

In this section we discuss the behaviour of green synthesized Ag NPs attached onto the GCE surface. The nanoparticles were attached on the electrode by drop-coating them onto the surface of the electrode and left overnight to dry before the characterization using CV starts. This was performed at different scan rates and the peak current for the oxidation process depends linearly on the scan rate that is as the scan rate increases, the peak current tend to absorb linearly. The anodic peak potential (E_{pa}) depends linearly with the logarithm of the scan rate [19]. The cathodic peaks are always well defined and suggest that the electron transfer is reversible, or at least close to reversible, this ratio strongly suggests that the oxidation of Ag NPs is accompanied by a loss of material from the electrode probably due to the solubility of charged nanoparticles and their diffusion away from the electrode.

The anodic peak shows the reduction of Ag NPs, as the scan rate increases the peaks shift towards the left and the changes might be due to due to electrochemical dissolution of Ag NPs on the electrode surface, at ~ +0.036 V. The change in appearance of the anodic peak as the scan rates increases possibly indicates the possible degradation of the nanoparticles [19].

Furthermore a plot of current versus the square root of scan rate was plotted for the green synthesized Ag NPs for both anodic and cathodic peaks. The slope for the anodic and cathodic have been calculated to be -3.4297 V/s and 18.75 V/s with R^2 being 0.4133 and 0.9162 respectively. In both cases the plots show a clear indication of the dependence of anodic peak and cathodic peak current on the scan rate. From the graph in figure 4.5 (b), the surface concentration of Ag NPs was determined using the Brown Anson equation [9] (Equation 4.1).

$$I_p/v = n^2F^2A\Gamma^*/4RT \quad (4.1)$$

From the equation, n is the number of electron transferred (n = 2), F is the faraday constant (96485 C mol^{-1}), Γ*Ag represent the surface concentration of Ag nanoparticles (mol cm^{-1}), A is the surface area of the glassy-carbon electrode (0.0201 cm^2), v is the scan rate (mV s^{-1}), R is the gas constant (8.314 J mol^{-1} K^{-1}) and T is the operating absolute temperature of the system (25 °C T in 298 K). The surface concentration (Γ*) of Silver nanoparticles was determined to is $2.5x10^{-4}$ mol cm^{-1}. Based on the graph (Figure 4.5(b), the Randel-Sevcik Equation (Equation 4.2) was also used to determine the diffusion coefficient of Ag NPs. A value of $3.58x10^{-23}$ cm^2/s was determined to be the diffusion coefficient of Ag NPs.

$$Ip = 0{,}4463nF\,{}^{nFDe}/_{RT}A\Gamma^*_{Ag}V \quad (4.2)$$

Where the indicated parameters maintain their usual definition as described above.

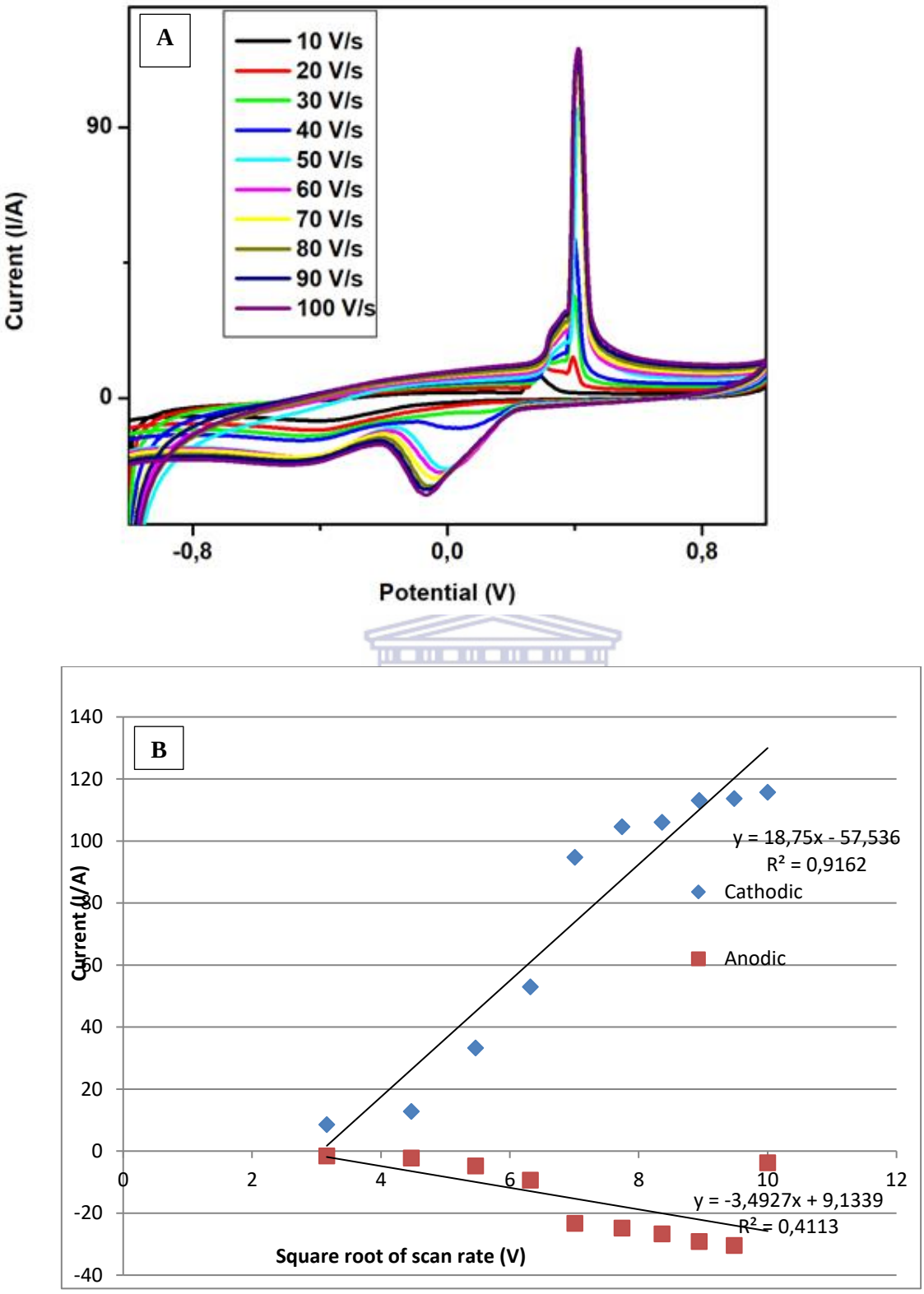

Figure 4.5: (A) Cyclic voltammetry of Ag NPs at different scan rates and (B) Plots of current versus log scan rate of anodic and cathodic peak Ag NPs.

4.4.2. Electrochemical impedance (EIS)

The conductivity of nanoparticles on the interface of an electrode can be examined by impedance measurements. The result may be represented graphically using two types of plots: Nyquist plot Figure 4.6 (A) and Bode plot Figure 4.6 (B). Figure 4.7 (A) exhibited almost a straight line with a very small depressed semi-circle arc (R_{et} = 2169 (Z′/Ω)) which represents the characteristics of diffusion limited electron transfer process on the electrode surface. While Figure 4.6 (B) shows that the nanoparticles are semi-conductive with a phase angle approximately 57.60^{o}.

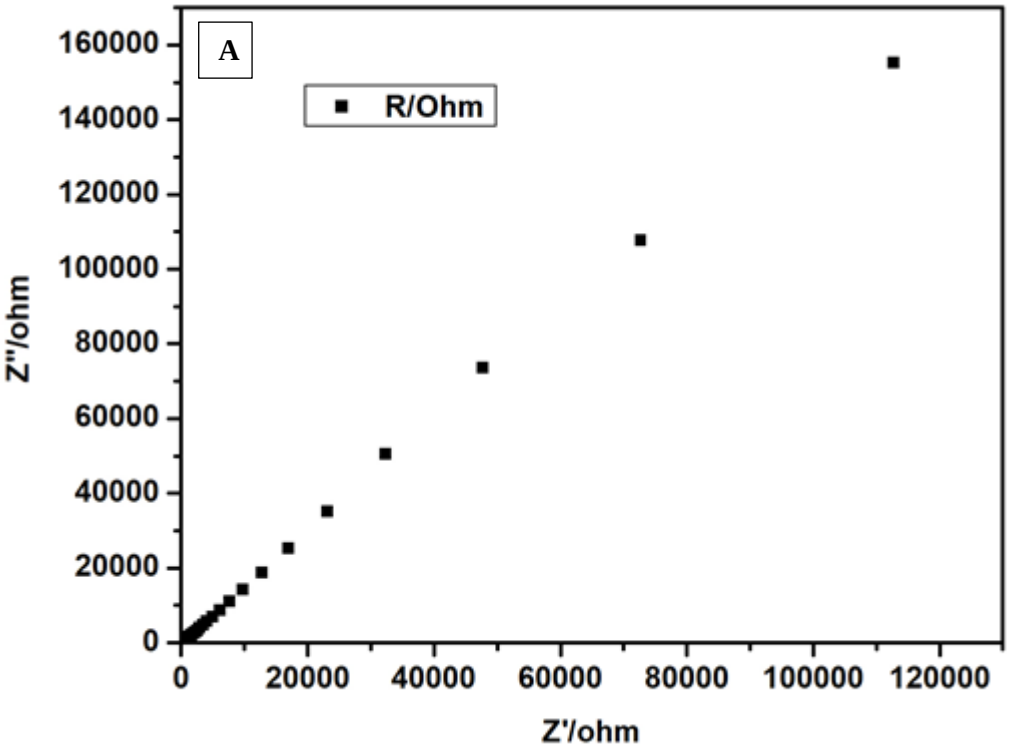

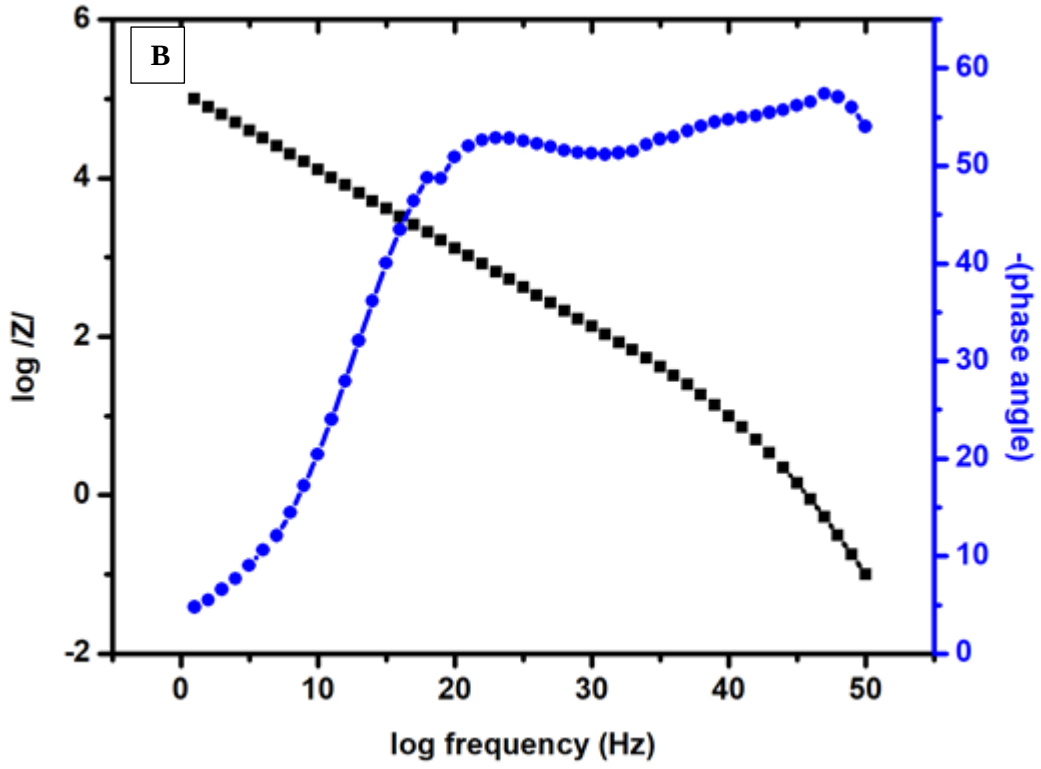

Figure 4.6 EIS data of green synthesized Ag NPs (A) Nyquist plot and (B) bode plot.

4. 5. Conclusion

A simple green synthesis method of stable silver nanoparticles using a pear extract at room temperature was reported in this study. Synthesis was found to be efficient in terms of reaction time as well as stability of the synthesized nanoparticles which exclude external stabilizers /reducing agents. It proves to be an eco-friendly, rapid green approach for the synthesis providing a cost effective and an efficient way for the synthesis of silver nanoparticles. Therefore, this reaction pathway satisfies all the conditions of a 100% green chemical process due to benefits of using fruit extract for synthesis is that it is energy efficient, cost effective, protecting human health and environment leading to lesser waste and safer products. This eco-friendly method could be a competitive alternative to the conventional physical/chemical methods used for synthesis of silver nanoparticle and thus has a potential to use in biomedical

applications and will play an important role in them being used as nanocomposite for immunosensor application. The Uv-vis spectrometry, cyclic voltammetry and HRTEM confirm the reduction of $AgNO_3$ to Ag^+. The EIS spectroscopy also complements the CV by studying the conductivity of the nanoparticles thus this confirms that pear extract is a good reducing agent for Ag NPs.

References

1. Kanchana, A., Agarwal, I., Sunkar, S., Nellore, J. and Namasivayam, K., 2011. Biogenic silver nanoparticles from Spinacia oleracea and Lactuca sativa and their potential antimicrobial activity. *Digest Journal of Nanomaterials and Biostructures*, *6*(4), pp.1741-1750.
2. Albrecht, M.A., Evans, C.W. and Raston, C.L., 2006. Green chemistry and the health implications of nanoparticles. *Green Chemistry*, *8*(5), pp.417-432.
3. Kanchana, A., Agarwal, I., Sunkar, S., Nellore, J. and Namasivayam, K., 2011. Biogenic silver nanoparticles from Spinacia oleracea and Lactuca sativa and their potential antimicrobial activity. *Digest Journal of Nanomaterials and Biostructures*, *6*(4), pp.1741-1750.
4. Lewinski, N., Colvin, V. and Drezek, R., 2008. Cytotoxicity of nanoparticles. *small*, *4*(1), pp.26-49.
5. Hardman, R., 2006. A toxicologic review of quantum dots: toxicity depends on physicochemical and environmental factors. *Environmental health perspectives*, *114*(2), p.165.
6. Das, R., Nath, S.S., Chakdar, D., Gope, G. and Bhattacharjee, R., 2009. Preparation of silver nanoparticles and their characterization. *Journal of Nanotechnology*, *5*, pp.1-6.
7. Taleb, A., Petit, C. and Pileni, M.P., 1998. Optical properties of self-assembled 2D and 3D superlattices of silver nanoparticles. *The Journal of Physical Chemistry B*, *102*(12), pp.2214-2220.
8. Nath, S.S., Chakdar, D. and Gope, G., 2007. Synthesis of CdS and ZnS quantum dots and their applications in electronics. *Nanotrends*, *2*(3), pp.20-28.

9. Noginov, M.A., Zhu, G., Bahoura, M., Adegoke, J., Small, C., Ritzo, B.A., Drachev, V.P. and Shalaev, V.M., 2007. The effect of gain and absorption on surface plasmons in metal nanoparticles. *Applied Physics B: Lasers and Optics*, *86*(3), pp.455-460.
10. Rajashekar, V., Rao, E.U. and Srinivas, P., 2012. Biological activities and medicinal properties of Gokhru (Pedalium murex L.). *Asian Pacific journal of tropical biomedicine*, *2*(7), pp.581-585.
11. Gurunathan, S., Jeong, J.K., Han, J.W., Zhang, X.F., Park, J.H. and Kim, J.H., 2015. Multidimensional effects of biologically synthesized silver nanoparticles in Helicobacter pylori, Helicobacter felis, and human lung (L132) and lung carcinoma A549 cells. *Nanoscale research letters*, *10*(1), p.35.
12. Shankar, S.S., Rai, A., Ahmad, A. and Sastry, M., 2004. Rapid synthesis of Au, Ag, and bimetallic Au core–Ag shell nanoparticles using Neem (Azadirachta indica) leaf broth. *Journal of colloid and interface science*, *275*(2), pp.496-502.
13. Reddy, N.J., Vali, D.N., Rani, M. and Rani, S.S., 2014. Evaluation of antioxidant, antibacterial and cytotoxic effects of green synthesized silver nanoparticles by Piper longum fruit. *Materials Science and Engineering: C*, *34*, pp.115-122.
14. Zuas, O., Hamim, N. and Sampora, Y., 2014. Bio-synthesis of silver nanoparticles using water extract of Myrmecodia pendan (Sarang Semut plant). *Materials Letters*, *123*, pp.156-159.
15. Logeswari, P., Silambarasan, S. and Abraham, J., 2015. Synthesis of silver nanoparticles using plants extract and analysis of their antimicrobial property. *Journal of Saudi Chemical Society*, *19*(3), pp.311-317.
16. Bar, H., Bhui, D.K., Sahoo, G.P., Sarkar, P., De, S.P. and Misra, A., 2009. Green synthesis of silver nanoparticles using latex of Jatropha curcas. *Colloids and surfaces A: Physicochemical and engineering aspects*, *339*(1), pp.134-139.

17. Magudapathy, P., Gangopadhyay, P., Panigrahi, B.K., Nair, K.G.M. and Dhara, S., 2001. Electrical transport studies of Ag nanoclusters embedded in glass matrix. *Physica B: Condensed Matter*, *299*(1), pp.142-146.

18. Dobre, N., Golgovici, F., Anicai, L. and Buda, M., 2014. Cyclic Voltammetry of Silver Nanoparticles on Platinum, Gold and Glassy Carbon Electrodes. *REVISTA DE CHIMIE*, *65*(5), pp.578-581.

Chapter 5

Results and discussion: ZnO nanoparticles

5.1. Introduction

Study of nanomaterials is one of the most and fast developing area in the field of nanoscience. Nanomaterials are controlled by nano crystalline sizes which are sizes less than 100 nm. They have an atom-like behaviour which occurs due to their large surface area and wider band gap between valence and conduction band when they are divided to near atomic size [1]. Metal oxides nanoparticles with nanostructure and semiconductors with dimensions in the nanometre (nm) empire have been of interest in many areas of chemistry, physics, material science, nanoscience, biotechnology, information technology and environmental technology as next generation technologies [2]. In recent years, zinc oxide (ZnO) has been an important semiconductor with enormous scientific and technological interest as well as increasing interest towards green chemistry and its application towards immunosensors [2]. This has resulted in the development of environmental friendly approach for the synthesis of nanoparticles due to the fact that green synthesis technique uses natural products such fruits and vegetables, teas or juice extracts to synthesize nanomaterials [3]. By using green synthesis pollution of the atmosphere by chemicals is reduced and thus green synthesized nanoparticles are known to be eco-friendly. ZnO has proved themselves to be a good nanomaterial for medical purposes due to its unique properties like UV absorption, antimicrobial, deodorizing, antifugal, antiviral and anticancer properties together with optical and steady thermal properties [3]. Thus in this study ZnO nanoparticles were prepared using green synthesis mixture of strawberries and green tea. These nanoparticles can be used in a wide variety of applications such as in biomolecular detection, immunosensor detection, diagnostic and micro-electronics.

5.2. Spectroscopic techniques

5.2.1. Ultraviolet–visible spectroscopy (UV-Vis)

Ultraviolet–visible spectroscopy (UV-Vis) is an absorption spectroscopy that measures the wavelength of a sample with the colour change of the sample involved using a light in the visible and adjacent ranges [4].

The size of the nanoparticles plays an important role in changing the entire properties of materials. Therefore size evolution of semiconducting nanoparticles becomes very important to explore the properties of the materials. UV-visible absorption spectroscopy is a widely used technique to examine the optical properties of nanosized particles [5]. For this study, the colour of the prepared zinc oxide nanoparticles was white with white precipitants, which is the distinctive colour of zinc oxide nanoparticles solution is due to the phenomenon known as plasmon absorbance. The incident light forms an oscillation in the conduction electron on the surface of the nanoparticles, then the collective oscillation of conduction electrons within metal nanoparticles and the surface plasmon resonance enables scattering and absorption of light at a particular frequency giving the nanoparticles a colour [6]. Electromagnetic radiation of ZnO NPs was obtained by characterizing with UV-vis as represented in Figure 5.1 where the UV-vis spectrum of the green synthesized nanoparticles where the absorption band was found to be approximately 301 nm. It indicates that the nanoparticles shift towards the blue line of the spectrum. The absorption band of 301 nm shows that the nature of the nanoparticles are mono-dispersed [4].

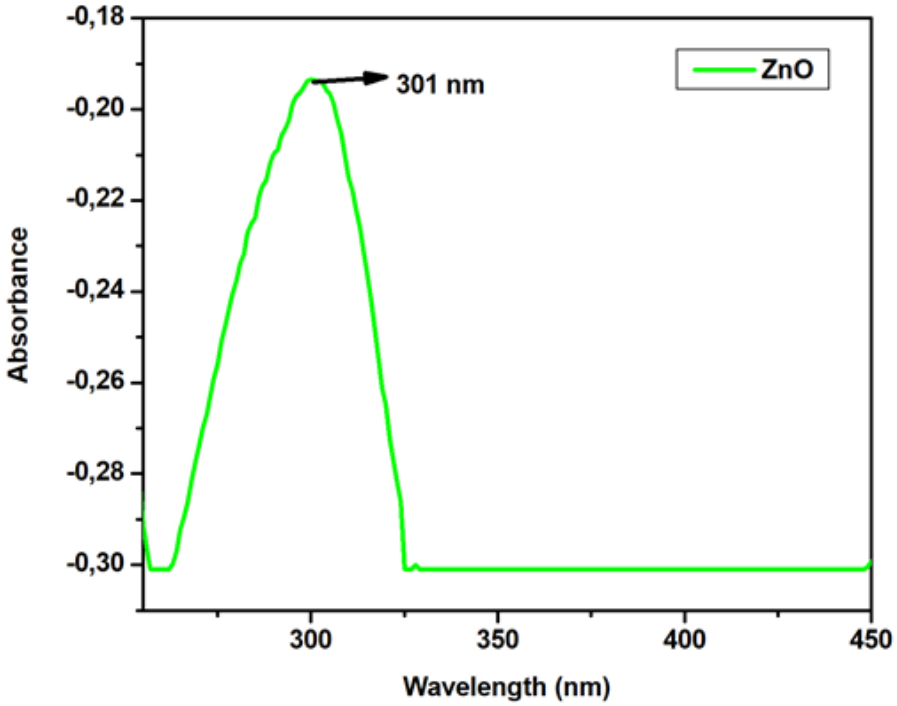

Figure 5.1: UV-VIS spectrum of green synthesized ZnO NPs dispersed in ethanol.

5.2.2. Fourier Transform Infrared Spectroscopy (FTIR)

FTIR has been used to gather information about the structure and purity of the green synthesized ZnO NPs from zinc nitrate as shown in Figure 5.2. The broad transition band found around 3444 cm^{-1} is due to the stretching vibrations of O-H groups in water, alcohols and phenols. The strong band around 2762 cm^{-1} is due to the stretching groups of C-H found in the green tea while the stretching vibrations found around 2426 cm^{-1} is due to N-H stretch in the amines of strawberries. The occurrence of the transition band around 2091 cm^{-1} is due to aromatic rings C=O found in polyphenols [7]. The C=C also confirms the presence of aromatic rings of amides around 1629 cm^{-1}.The C–N stretch of amide-I in protein gives the band around 1387 cm^{-1}. The C–O stretching in amino acid causes a band around 1031 cm^{-1}. The involvements of these biomolecules in the reduction and stabilization actions are clearly identified from the IR spectrum of the synthesized ZnO NPs. The additional two peaks

appearing around 695 cm^{-1} and 821 cm^{-1} in the IR spectrum of the ZnO NPs are the characteristic peaks of ZnO molecules [7]. The presence of higher percentage of phenolic group of molecules is responsible for the reduction process while the amino acids and amide linkages in protein are responsible for the stabilization of the ZnO nanoparticles [7].

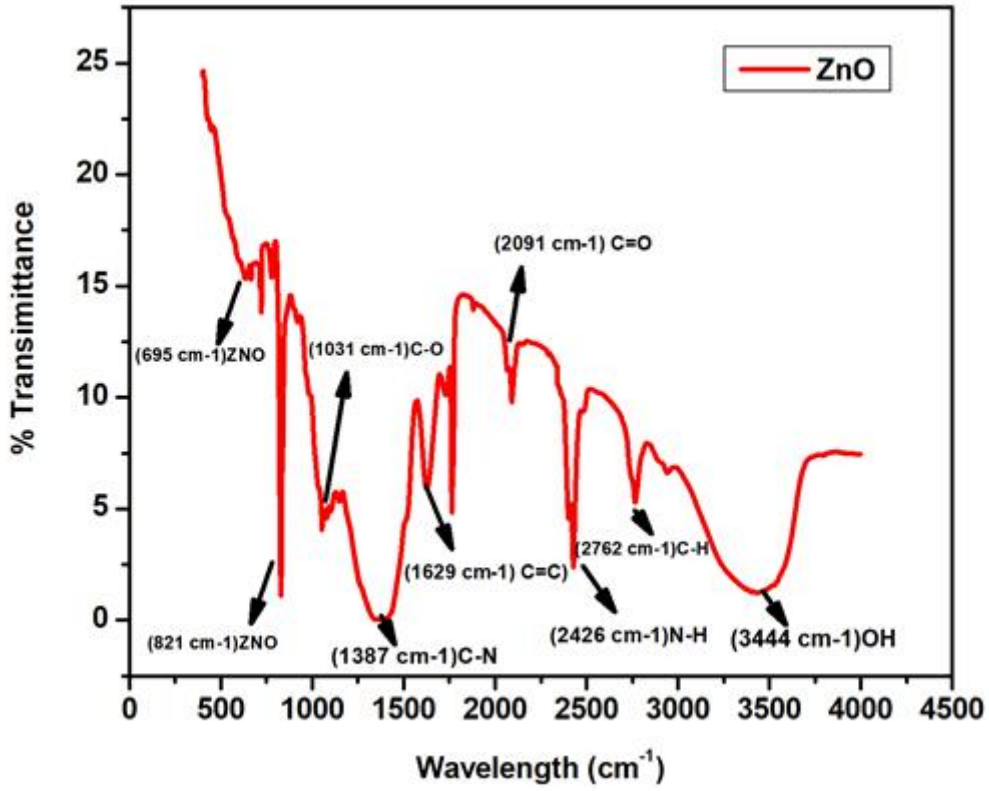

Figure 5.2: FTIR spectrum of green synthesized ZnO NPs.

5.3. Microscopic techniques

5.3.1. High resolution transmission electron microscopy (HR-TEM)

The shape and size of the resultant nanoparticles were elucidated with the help of HR-TEM figureb5.3 (a). Few drops of zinc oxide nanoparticle solution were placed on a carbon-coated copper grid and allowed to dry under high temperature conditions and HR-TEM images were recorded. Morphological images of ZnO NPs are scattered around and the shape of the

nanoparticles is found to be spherical with a diameter size of less than 20 nm. The HR-TEM images also reveal that the nanoparticles are separated by uniform particle distance. This is caused by large-sized particles which aggregate two or more nanoparticles together which in turn result in the presence of excess amounts of reducing efforts and the interactions between stabilizing molecules bound to the surface of particles and secondary reduction process on the surface of the preformed nuclei [8]. On the other hand figure 5.3 (B) shows SAED of the nanoparticles which confirms that the nanoparticles are crystalline. Crystalline nanoparticles are known to be the best semiconductors since they have no grain boundary [9], and the particle size distribution of the nanoparticles is presented in figure 5.3 (C) below and the nanoparticles are found to be 10 nm in diameter size.

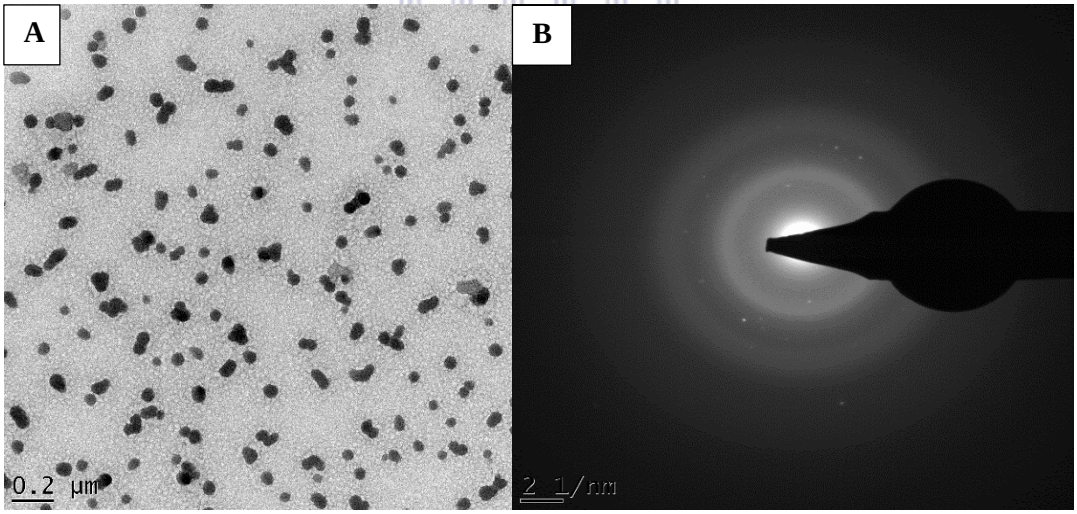

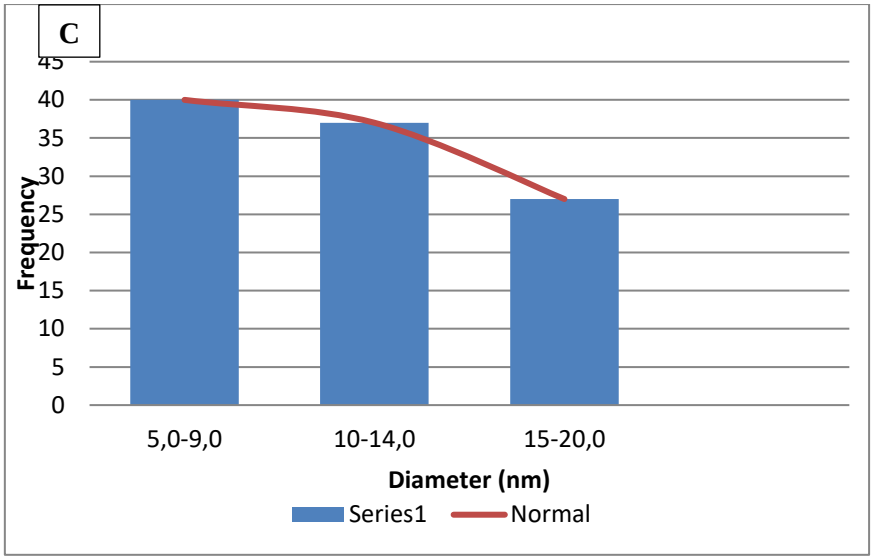

Figure 5.3 (A) HR-TEM image of green synthesized ZnO NPs, (B) SAED of ZnO and (C) particle size distribution of ZnO NPs.

5.3.2. High resolution scanning electron microscopy (HR-SEM)

The HR-SEM images of ZnO NPs are shown in Figure 5.4 (A). The surface morphology of zinc oxide nanoparticles are seen to have a spherical shape which complements the findings in the HR-TEM image. It is observed that the nanoparticles remain in an aggregated form due to high surface energy and high surface area to volume ratio [10]. Nanoparticles of that nature are usually found to be 10-30 nm in diameter size. The size and the shape nanoparticles can enhance drug targeting according to the new findings of science research, and spherical nanoparticles tend to adhere more effectively to the surface of endothelial cells that line inside the blood vessel [11]. On the other hand Figure 5.4 (B) shows the EDS analysis of ZnO NPs which confirms that indeed ZnO NPs synthesis was successful by showing about 1000 counts of zinc element.

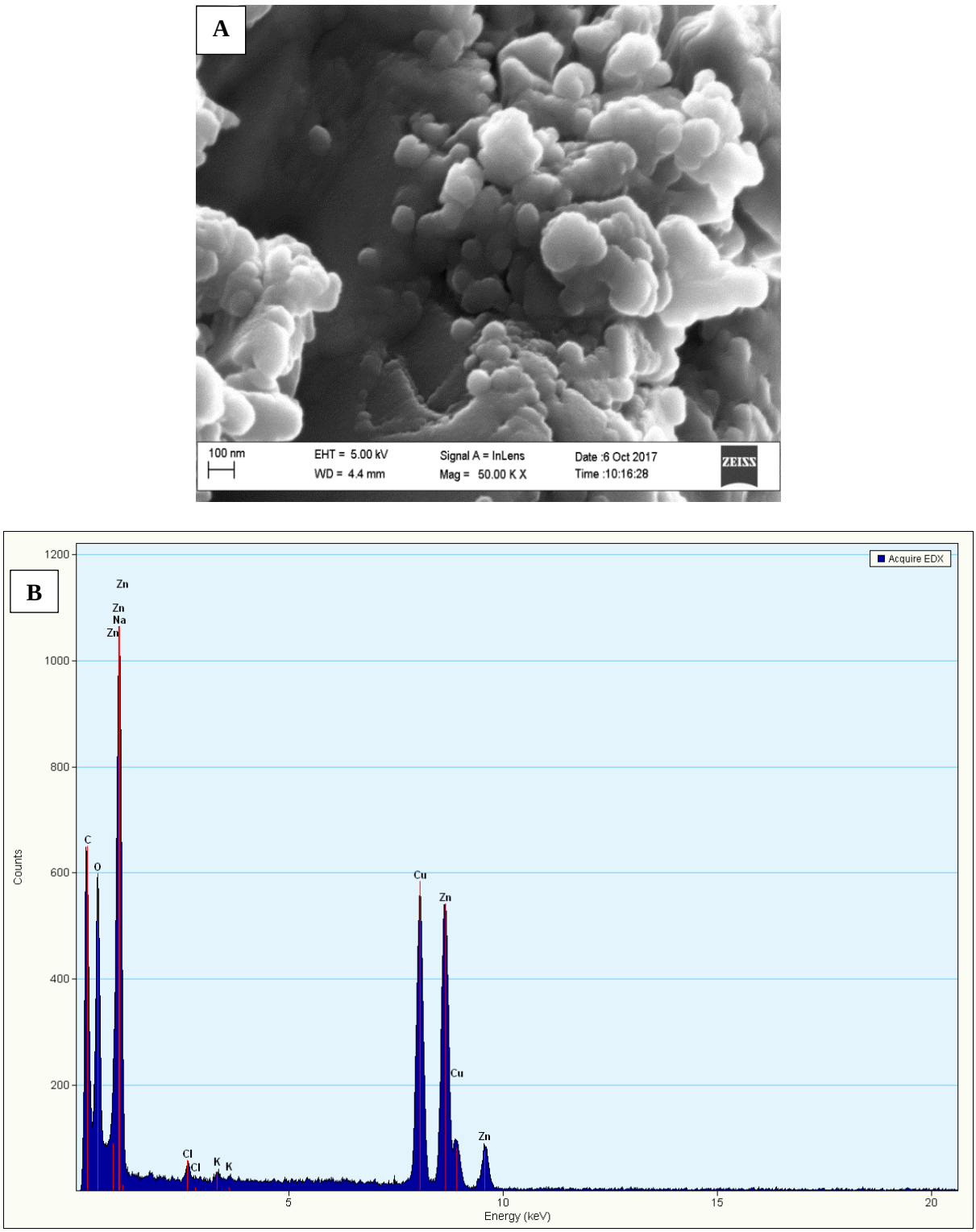

Figure 5.4 (a) HR-SEM image of green synthesized ZnO NPs and 5.4 (b) EDS of ZnONPs.

5.4. Electrochemistry of green synthesized ZnO nanoparticles

5.4.1. Cyclic voltammetry (CV)

The electrochemical properties of the green synthesized ZnO NPs was investigated by CV. ZnO nanoparticles are known to enhance specific capacitance and electrochemical stability of metal oxides. Figure 5.5 (A) represent CV of ZnO NPs at different scan rates and the anodic and cathodic peak are observed at -0.65 V and 0.37 V respectively at a potential scan of 100 V/s. A shift in the potential was observed with an increase in the scan rate [12].

Furthermore a plot of current vs the square root of scan rate was plotted for the green synthesized ZnO NPs for both anodic and cathodic (Figure 5.5 B). The slope for the anodic and cathodic have been calculated to be -0.5322 V/s and 0.4053 V/s with R^2 being 0.9206 and 0.971 respectively. In both cases the plots show a clear indication of the dependence of anodic peak and cathodic peak current on scan rate. From the cathodic peak (because the surface concentration need to be positive), the surface concentration of ZnO NPs was determined using the Brown Anson equation (Equation 4.1) [12].

$$I_p/v = n^2F^2A\Gamma^*/4RT \quad (4.1)$$

From the equation, n is the number of electron transferred (n = 2), F is the faraday constant (96485 C mol^{-1}), Γ*ZnO represent the surface concentration of ZnO nanoparticles (mol cm^{-1}), A is the surface area of the glassy-carbon electrode (0.0201 cm^2), v is the scan rate (mV s^{-1}), R is the gas constant (8.314 J mol^{-1} K^{-1}) and T is the operating absolute temperature of the system (25 °C T in 298 K). The surface concentration (Γ*ZnO) of zinc oxide nanoparticles was determined to be 1.71×10^{-2} mol cm^{-1}. Based on Figure 5.5 (B) the Randel-Sevcik Equation (Equation 4.2) was also used to determine the diffusion coefficient of ZnO NPs. A value of 1.98×10^{19} cm^2/s was determined to be the diffusion coefficient of ZnO NPs.

$$Ip=0{,}4463nF\,{}^{nFDe}/_{RT}A\Gamma^{*}_{ZnO}\,V \qquad (4.2)$$

Where the indicated parameters maintain their usual definition as described above.

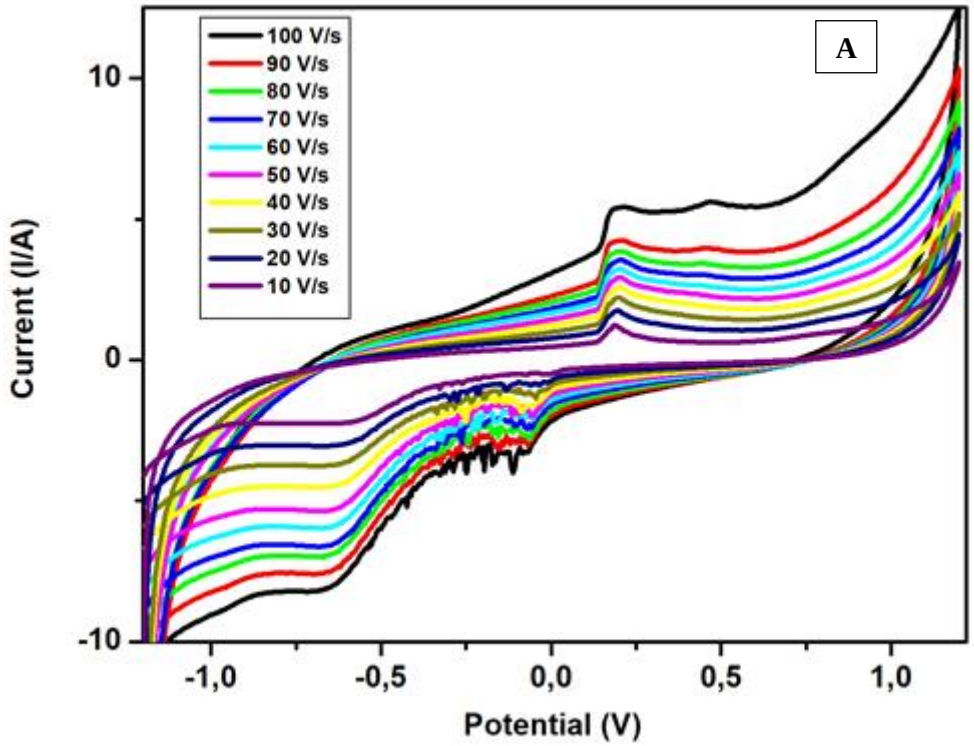

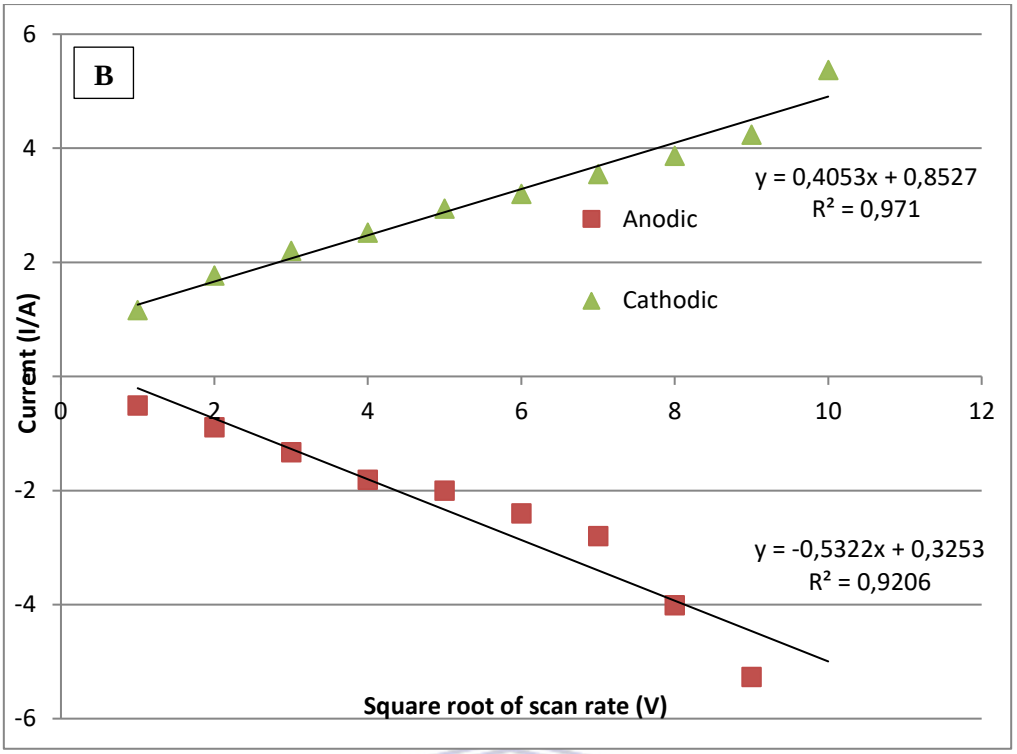

Figure 5.5 (a) CV of green synthesized ZnO NPs and (b) graph of current vs the square root of scan rate for ZnO NPs.

5.4.2. Electrochemical Impedance (EIS)

Electrochemical impedance spectroscopy (EIS) is very useful to understand the inner resistance and charge transfer kinetics of nanoparticles [13]. The electron transport properties of the ZnO NPs photo-electrodes annealed at the scan rate of 30 V/s were investigated by electrochemical impedance spectra. The conductivity of ZnO NPs was also investigated by characterizing it using EIS. EIS usually is divide into two graphs which are Nyquist and Bode plots. EIS analysis for green synthesized ZnO is represented by Figure 5.6 (A) shows the Nyquist plot of ZnO nanoparticle where the figure exhibit almost a straight line with no semi-circle. In Figure 5.6 (B) the Bode plot, it was found that the impedance at lower frequency (2 Hz) is higher than that at the higher frequency with a sharp decrease in impedance at 2.52 Z'/Ω due to an increase

in capacitance [14]. On the hand the phase angle shows that the nanoparticles are semi-conductive with a phase angle of 76.05^0.

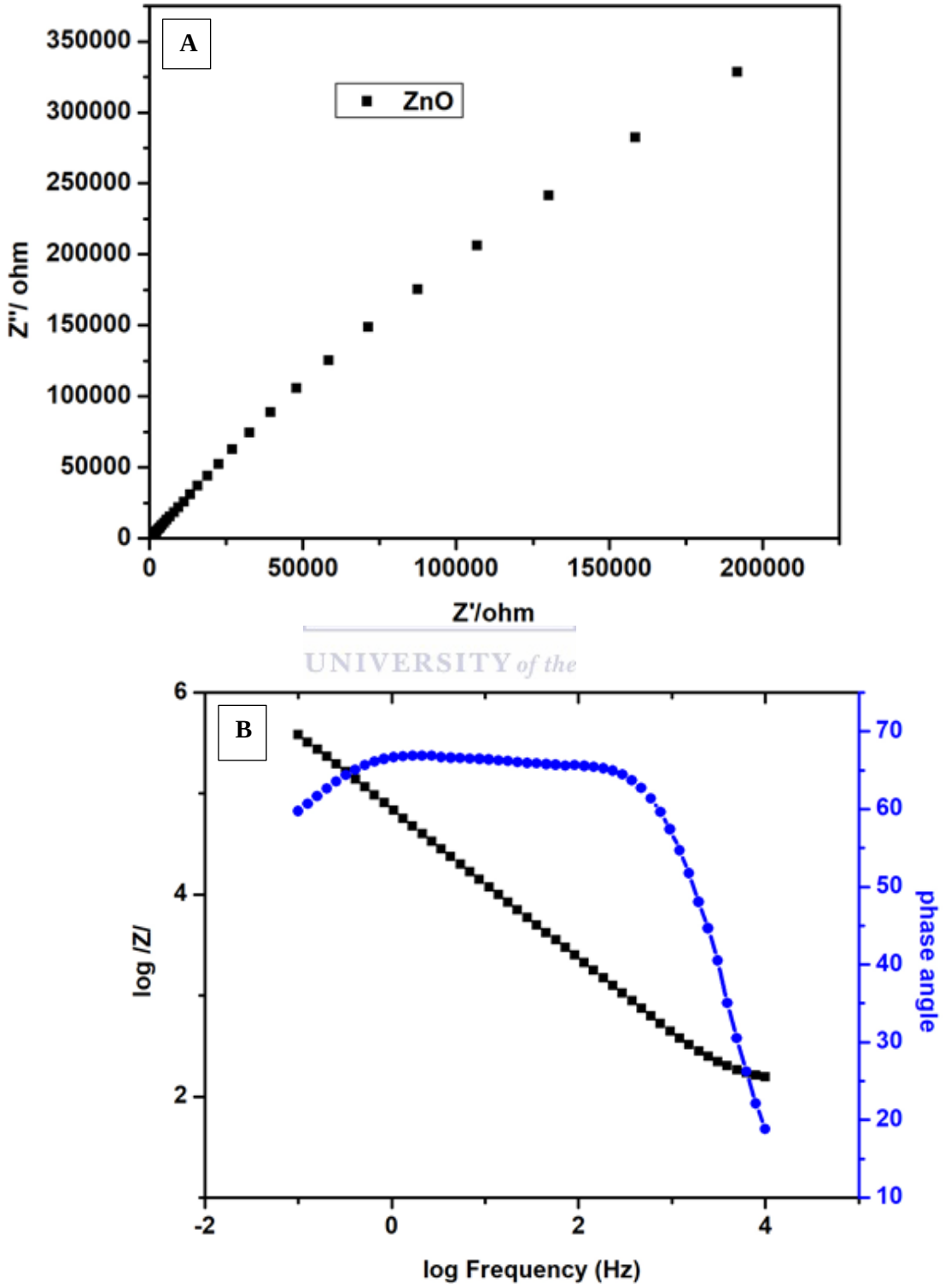

Figure 5.6 EIS data of green synthesized ZnO NPs (a) Nyquist plot and (b) Bode plot

5.5. Conclusion

ZnO nanoparticles have been successfully synthesized using zinc nitrate at room temperature using strawberry extract and green tea as capping agent. The morphological behaviour of ZnO NPs was studied using HRSEM, HRTEM and FTIR to check the shape, size and chemical groups found in the nanoparticles at which indeed these techniques showed that the nanoparticles were spherical in shape and a diameter of less than 20 nm particle size. The electrochemical behaviour of ZnO NPs was studied using CV and EIS. The semiconducting nature of ZnO observed in the Bode plot (Figure 5.6 (b) must be due to the large oxygen deficiency in the nanoparticles.

References

1. Khan, R., Kaushik, A., Solanki, P.R., Ansari, A.A., Pandey, M.K. and Malhotra, B.D., 2008. Zinc oxide nanoparticles-chitosan composite film for cholesterol biosensor. *Analytica chimica acta*, *616*(2), pp.207-213.
2. Dhanemozhi, A.C., Rajeswari, V. and Sathyajothi, S., 2017. Green Synthesis of Zinc Oxide Nanoparticle Using Green Tea Leaf Extract for Supercapacitor Application. *Materials Today: Proceedings*, *4*(2), pp.660-667.
3. Nava, O.J., Soto-Robles, C.A., Gómez-Gutiérrez, C.M., Vilchis-Nestor, A.R., Castro-Beltrán, A., Olivas, A. and Luque, P.A., 2017. Fruit peel extract mediated green synthesis of zinc oxide nanoparticles. *Journal of Molecular Structure*, *1147*, pp.1-6.
4. Guo L, Yang S, Yang C, Yu P, Wang J, Ge W, Wong GK. Synthesis and characterization of poly (vinylpyrrolidone)-modified zinc oxide nanoparticles. Chemistry of Materials. 2000 Aug 21; 12(8):2268-74.
5. Singh, A.K., 2010. Synthesis, characterization, electrical and sensing properties of ZnO nanoparticles. *Advanced Powder Technology*, *21*(6), pp.609-613.
6. Liu, H., Piret, G., Sieber, B., Laureyns, J., Roussel, P., Xu, W., Boukherroub, R. and Szunerits, S., 2009. Electrochemical impedance spectroscopy of ZnO nanostructures. *Electrochemistry Communications*, *11*(5), pp.945-949.
7. Xu, S., Cheng, C., Guo, W., He, Y., Huang, R., Du, S. and Wang, N., 2013. Tuning the optical and electrical properties of hydrothermally grown ZnO nanowires by sealed post annealing treatment. *Solid State Communications*, *160*, pp.41-46.
8. Zhang, Z., Yu, H., Wang, Y. and Han, M.Y., 2006. Aggregation-driven growth of well-oriented ZnO nanorod arrays. *Nanotechnology*, *17*(12), p.2994.

9. Zhang, Z., Yu, H., Shao, X. and Han, M., 2005. Near-Room-Temperature Production of Diameter-Tunable ZnO Nanorod Arrays through Natural Oxidation of Zinc Metal. *Chemistry-A European Journal*, *11*(10), pp.3149-3154.
10. Talam, S., Karumuri, S.R. and Gunnam, N., 2012. Synthesis, characterization, and spectroscopic properties of ZnO nanoparticles. *ISRN Nanotechnology*, *2012*.
11. Topoglidis, E., Cass, A.E., O'Regan, B. and Durrant, J.R., 2001. Immobilisation and bioelectrochemistry of proteins on nanoporous TiO 2 and ZnO films. *Journal of Electroanalytical Chemistry*, *517*(1), pp.20-27.
12. Gupta, A., Bhatti, H.S., Kumar, D., Verma, N.K. and Tandon, D.R., 2006. Nano and bulk crystals of ZnO: synthesis and characterization. *Digest Int J Nanomat Biostruct*, *1*, pp.1-9.
13. Al-Kahlout, A., 2015. Thermal treatment optimization of ZnO nanoparticles-photoelectrodes for high photovoltaic performance of dye-sensitized solar cells. *Journal of the Association of Arab Universities for Basic and Applied Sciences*, *17*, pp.66-72.
14. Al-Kahlout, A., 2012. ZnO nanoparticles and porous coatings for dye-sensitized solar cell application: Photoelectrochemical characterization. *Thin Solid Films*, *520*(6), pp.1814-1820.

Chapter 6

Results and discussion: Graphene Oxide

6.1. Introduction

Graphene oxide (GO) is obtained by the chemical treatment of graphite through oxidation, following with dispersion in water or a suitable organic solvent. GO exhibits large amount of oxygen functional groups such as hydroxyl, carbonyl, carboxyl and epoxy groups on its basal plane and edges [1]. Graphene oxides have currently transpired as a new carbon- based nanoscale particle that provides an alternative path to graphene due to its extraordinary properties like large specific surface area volume ratio and low production cost [1]. It is a single layered material made up of oxidizes graphite which is available in large sizes at inexpensive prices. Structurally GO display large amount of oxygen functional groups such as hydroxyl, carbonyl, carboxyl and epoxy groups on its basal plane and edges. Since these groups have a high level of hydrophilicity and can easily dissolve in water and other solvents allow GO to be informally deposited on to wide ranging substrates in the form of thin films, which makes it potentially useful for micro-electronics [2]. Recently, graphene oxide has gained more attention because it is functionalized easily with fluorescent probe and other compatible biomolecules [2]. These unique properties of GO make it a promising nanomaterial for bio-application. Industrially produced graphene oxide could be used for wide range of application such as solar cell, hydrogen storage, transparent conductive films, Polymer composite, Paper like materials, biomedicine, fabricating nano-electronic devices, energy storage devices , biosensors, catalysis and transparent electrodes [3].

6.2. Spectroscopic techniques

6.2.1. Ultraviolet–visible spectroscopy (UV-Vis)

Ultraviolet–visible spectroscopy (UV-Vis) in this chapter is used to measure the absorption wavelength of an aqueous GO.

A UV-vis spectrum of aqueous GO dispersions is presented in Figure 6.1. Two kinds of characteristic features were observed in these spectra to identify GO: The shoulder found around ~287 nm corresponds to α-π^* band transition which is due to the presence of localized oxygen bonds trapped in water, which has a band gap of 5.51 $x10^{-28}$ eV [4]. The broad peak found around ~ 222 nm corresponds to α-α^* transition which is similar to that of diamond-like carbon films [4]. This is due to attachment of oxygen to graphene which converts a planar sp^2 to sp^3 and produces a corresponding absorption peak at higher energy than the π-π^* band transition [4].

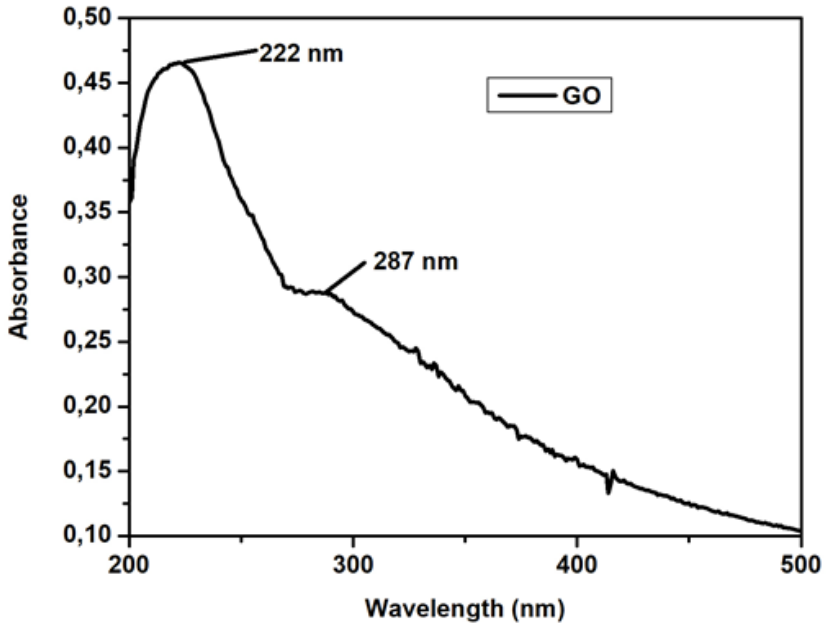

Figure 6.1: UV-VIS spectrum of synthesized graphene oxide dispersed in PBS solution.

6.2.2. Fourier Transform Infrared Spectroscopy (FTIR)

FTIR has been used to gather information about the structure and purity of the synthesized graphene oxide. Figure 6.2 shows the FTIR structure of GO. The FTIR spectra shows a broad peak between 3396 cm^{-1} in the high frequency area corresponds to the stretching and bending vibration of OH groups of water molecules adsorbed on GO. Therefore it can be concluded that it has strong hydrophilicity [5]. A broad peak from 1619 cm^{1} represent symmetric and asymmetric stretching vibrations of CH_2, while the band at 679 cm^{-1} corresponds to the stretching vibrations of C=O carbonyls groups present at the edges of GO. The stretching frequency from 1135 cm^{-1} represent the stretching vibrations of C-O carboxylic acids that are found in the near edge of GO [6]. The peak at 578 cm^{-1} and 624 cm^{-1} corresponds to the vibration of C-O of carboxylic acids and C-OH of alcohols respectively. The presence of oxygen-containing groups reveals that the graphite has been reduced to GO [6].

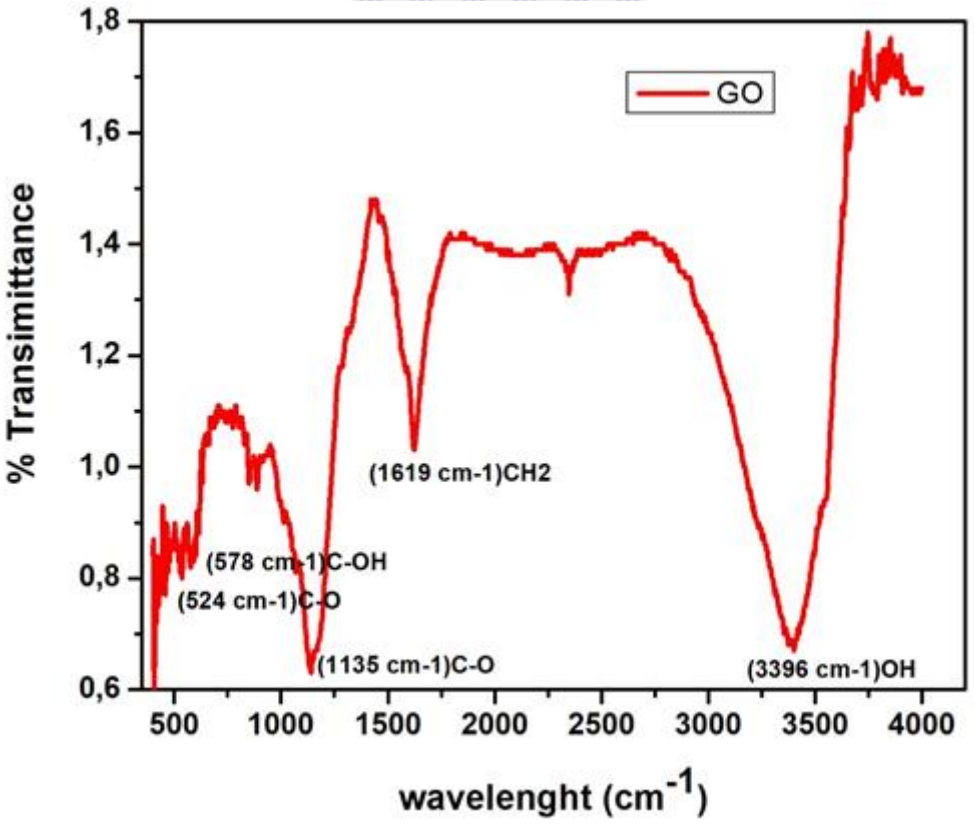

Figure 6.2: FTIR spectrum of Graphene oxide.

6.2.3. Raman Spectroscopy

The change in structural transformation from chemical transformation which is pure graphite Figure 6.3 (B) to graphene oxide Figure 6.3 (A) was investigated by Raman spectroscopy. The Raman spectrum for graphene oxide in figure 6.3 (A) reveals a strong D band at 2903 $cm^{-1}$and a moderate G band at 3005 cm^{-1}. The D band found at 2903 cm^{-1} is caused by the stokes phonon energy shift due to laser excitation which creates a second-order overtone of different in-plane vibration, commonly known as 2D band [7]. Because of added forces and chemicals used during the synthesis from the interaction of graphite layers being split into few layers of graphene it's possible for these bands to shift positions as the layers of graphene increase in size during the interaction. The position of the bands also depends on the number of layers available [8]. The G band occurs as results of the symmetry which allows first order scattering of the E_2g mode which is Sp^3 hybridization of carbon atoms that occur in the neatly ordered graphite structure [9]. Graphite [Figure 6.3 (B)] on the other hand shows a significant decrease, broadening and Raman shift to 2968 cm^{-1} for the G band while the D band at 2893 cm^{-1}. This change might be due to compressed graphite layers which is due to increase in size of the in-plane sp^2 domains caused by the insertion of the epoxy, carboxyl, carbonyl and hydroxyl groups between the individual layers of the graphite [10].

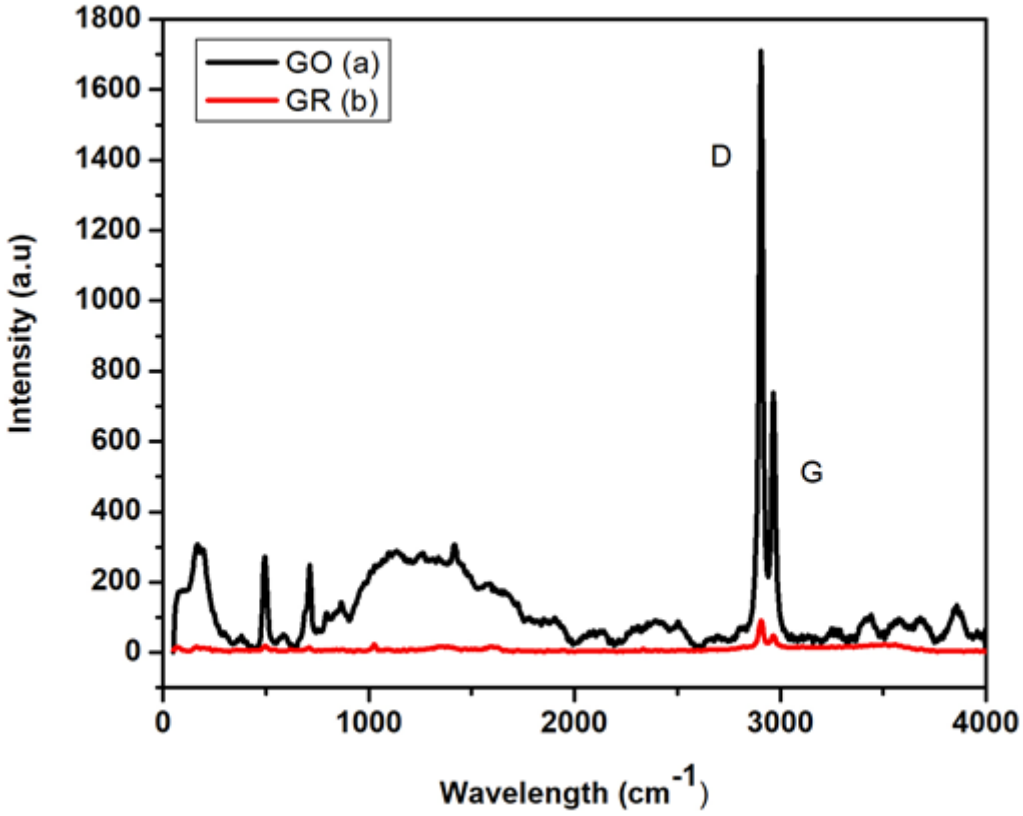

Figure 6.3: Raman spectroscopy of graphene oxide (a) graphite (b)

6.3. Microscopic Techniques

6.3.1. High resolution transmission electron microscopy (HR-TEM)

The Morphologic structure of Graphene oxide was investigated using HR-TEM. Samples for HR-TEM analysis were prepared by ultra-sonication in pure ethanol and then drop-coated onto Copper grids. The HR-TEM image, figure 6.4 (A) graphite shows thick dark flakes with distinct sharp, straight edges demonstrating its crystalline nature. The GO image, figure 6.4 (B), however is significantly different in graphitic structure when compared to that of graphite. Here, large transparent sheets which have soft edges are seen with entanglement and folding being described as large wrinkles within sheets. An increase in transparency suggests regions of monolayer graphene [11]. Figure 6.4 (C) represent the SAED of GO oxide which clearly

shows that GO is polycrystalline, which shows that GO will give a full support when nanoparticles are attached in the composite.

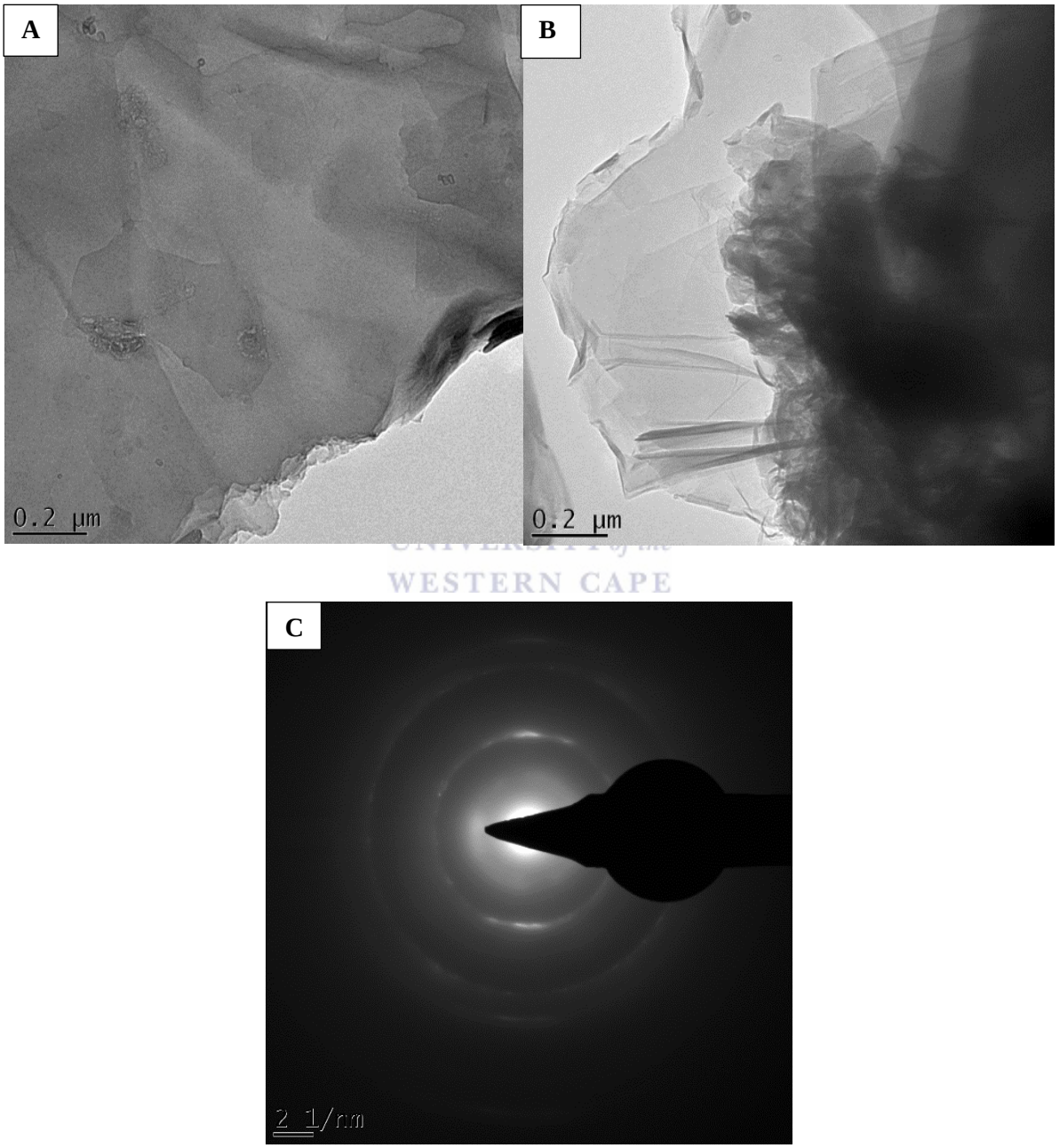

Figure 6.4 HR-TEM images of graphite (A) and graphene oxide (B) SAED of GO (C)

6.3.2. High resolution scanning electron microscopy (HR-SEM)

The images of HR-SEM were taken by scanning the beam across, creating an image of the surface of the sample, with exceptional depth of the field. The image is observed through the detection of "secondary" electrons that are released from the specimen as a result of it being scanned by high energy "primary" electrons [12]. This is all done in the Zess Auriga 1-20 KV machine. The samples are prepared by placing them on top of metal rings with adhesive and coated with 40 - 60 nm of metal such as Gold/Palladium and then observed in the microscope. Figure 6.5 (A) shows HR-SEM images of pure graphite without purification and it shows layers of graphite being starched together in one place, figure 6.5 (B) shows image of GO after purification which shows one layer sheet. On the other hand figure 6.5 (C) shows EDS analysis of GO. The presence of carbon and oxygen elements in the graph confirm the formation of GO as the GO is also known to be a carbon based material. On the other hand the availability of potassium and sulphur in the graph shows that the GO wasn't 100% percent purified as the sulphuric acid and potassium permanganate were used during the synthesis. Also the copper elements available are due to copper grids used during characterisation using HR-SEM imaging.

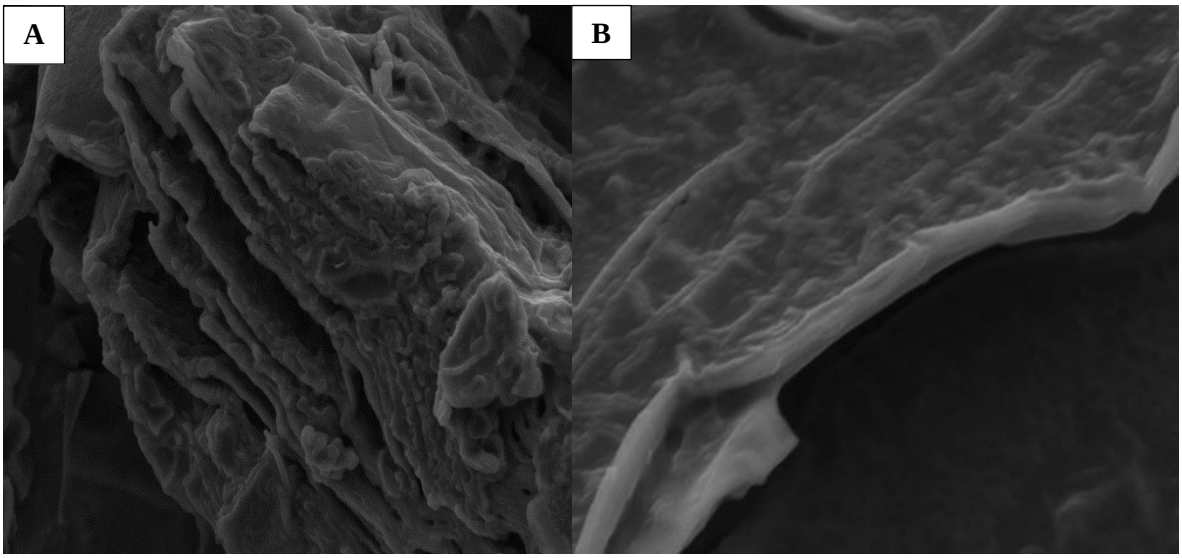

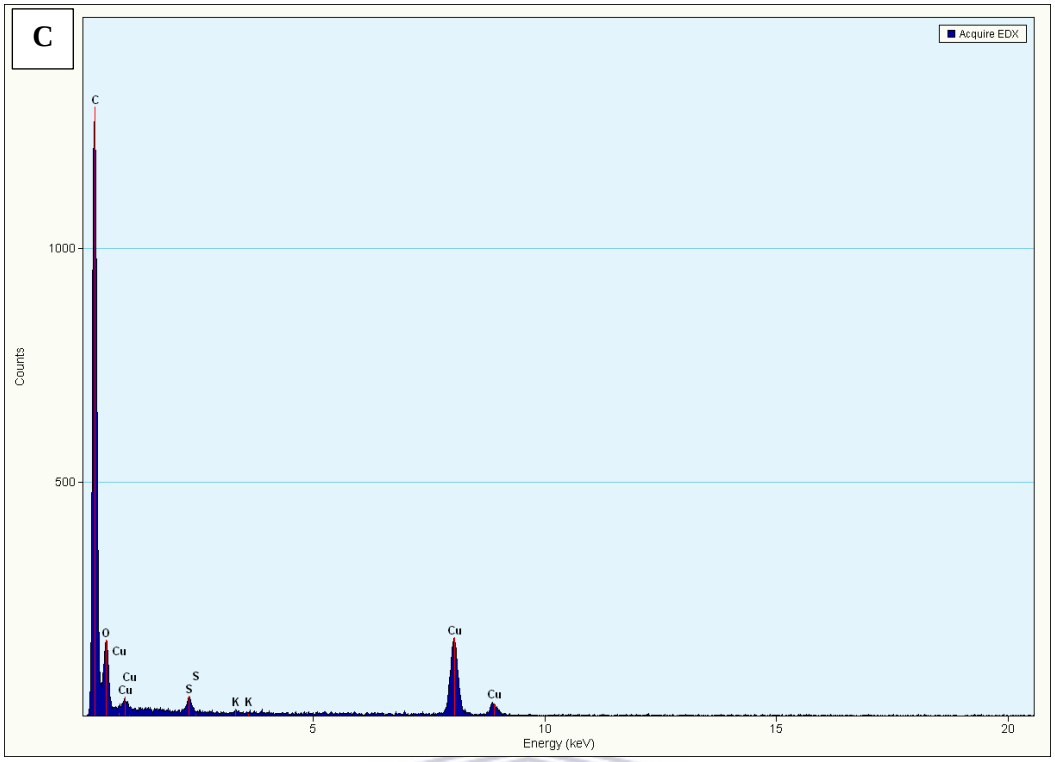

Figure 6.5: HR-SEM images of graphite (A), graphene oxide (B) and EDS of GO (C)

6.4. Electrochemistry of graphene oxide (GO)

6.4.1. Cyclic voltammetry (CV)

In this section we discuss the behaviour of synthesized graphene oxide attached onto the GCE surface. The GO solution was attached on the electrode by drop-coating it onto the surface of the electrode and left overnight to dry before the characterization using CV starts. Monotonous cyclic voltammetry obtained from the electrochemical reduction of a GO colloidal solution (1.0 mg mL^{-1}) onto GCE are shown in Figure 6.6 (A) it shows two anodic (I and II) and two cathodic (III and IV) peaks. The conductivity of GO on the GCE surface electrode is confirmed by the redox reaction which appears between peak (II and IV). An increase in anodic peak (II) at 0.8 V with increasing number of scans was observed [13] whereas the cathodic peak (IV) is infused at the scan rates from 50 V/s to 100 V/s but then increases continuously from the scan rate of

10 V/s to 40 V/s. This redox behaviour can be caused by the deposition of GO sheets that are in direct contact with the electrode surface [13].

Furthermore a plot of square root of scan rate vs current was plotted for the synthesized graphene oxide where a straight line was observed for both peaks. In both cases the plots show a clear indication of the dependence of anodic peak and cathodic peak current on scan rate. However the slope of the linear [*I*p,a vs υ½] plot of the redox peak anodic has been calculated to be -0.6293 (peak IV) and -0.08342 (peak III) whereas a slope for the cathodic peak is calculated to be 0.6285 (peak I) and 1.5654(peak II) V/s**.** From Figure 6.6 (B) the surface concentration of graphene oxide was determined using the Brown Anson equation (equation 6.1).

$$I_p/v = n^2F^2A\,\Gamma^{*}GO\,/4RT \qquad (6.1)$$

From the equation, *n* is the number of electron transferred (*n* = 1), F is the Faraday constant (96485 C mol^{-1}), Γ^{*}GO represent the surface concentration of GO nanoparticles (mol cm^{-1}), *A* is the surface area of the glassy-carbon electrode (0.0201 cm2), *υ* is the scan rate (mV s^{-1}), *R* is the gas constant (8.314 J mol^{-1} K^{-1}) and T is the operating absolute temperature of the system (25 °C T in 298 K). The surface concentration (Γ^{*}GO) graphene oxide was determined to be 1.33 x 10^{-6} mol cm^{-1} using Equation 6.1. Furthermore, the Randel-Sevcik Equation (Equation 6.2) was also used to determine the diffusion coefficient of graphene oxide. A value of 1.90 x10^{-16} cm^2/s was determined to be the diffusion coefficient of GO.

$$I_p = 0{,}4463nF\,{}^{nFDe}/_{RT}A\Gamma^{*}{}_{GO}V \qquad (6.2)$$

Where the indicated parameters maintain their usual definition as described above.

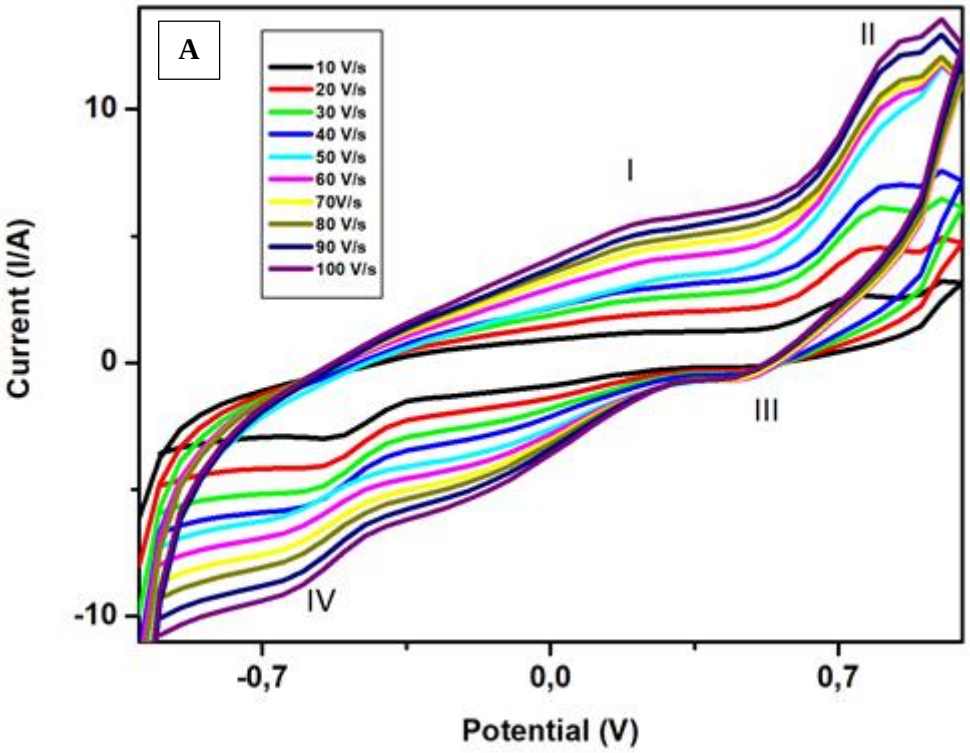

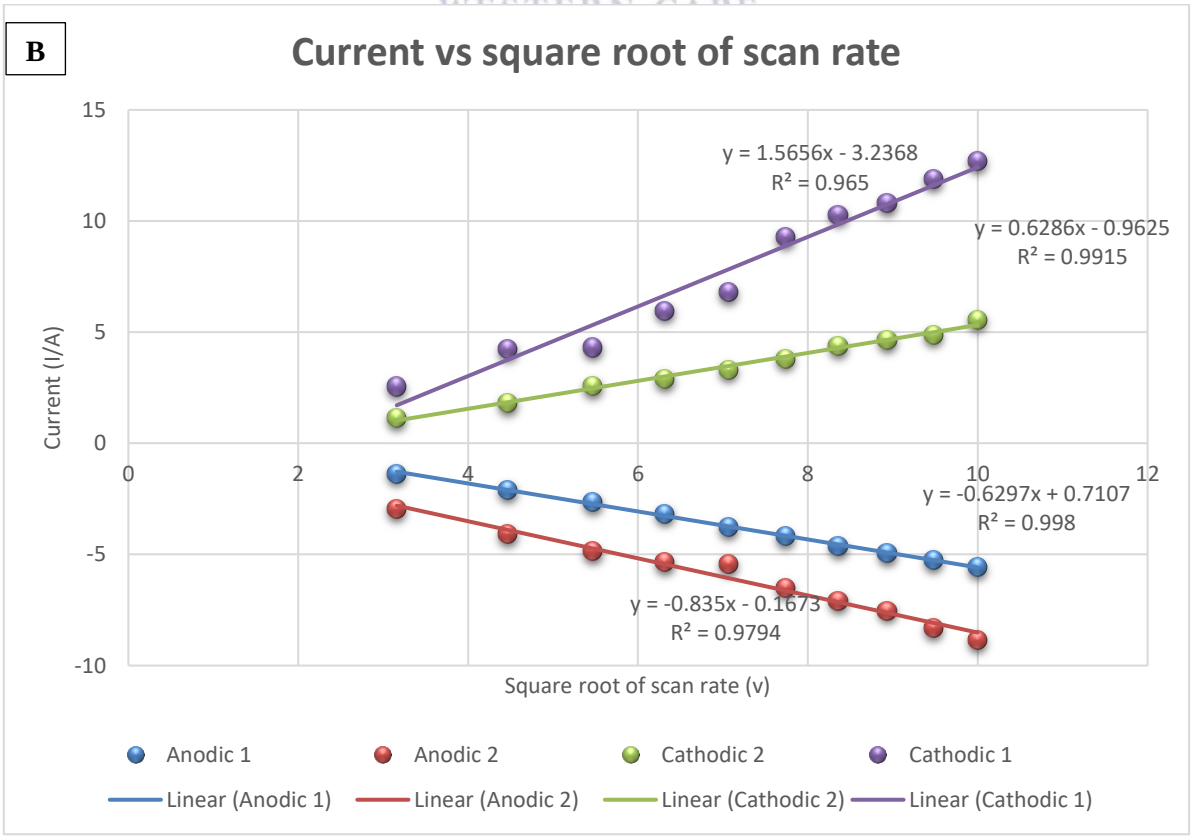

Figure 6.6 Cyclic voltammetry of GO (a) and 6.6 (b) a plot of square root of scan rate vs current for GO.

6.4.2. Electrochemical Impedance (EIS)

The conductivity of GO was also studied using EIS. Figure 6.7 (A) shows a Nyquist plot of GO which exhibit a straight line. In Figure 6.7 (B) the Bode plot of GO shows that the electrode exhibited typical AC impedance characteristics of supercapacitors [13]. In the high frequency region the real axis intercept represents a combined resistance (R_s) containing intrinsic resistance of electrode material, ionic resistance of electrolyte and contact resistance between the electrode and current collector as well as the radius of semicircle that act an indicative of the electrode conductivity and the charge-transfer resistance (R_{ct}) of electrode material [13]. Based on the phase angle of 70^{o} shows that GO has reached its capacitance.

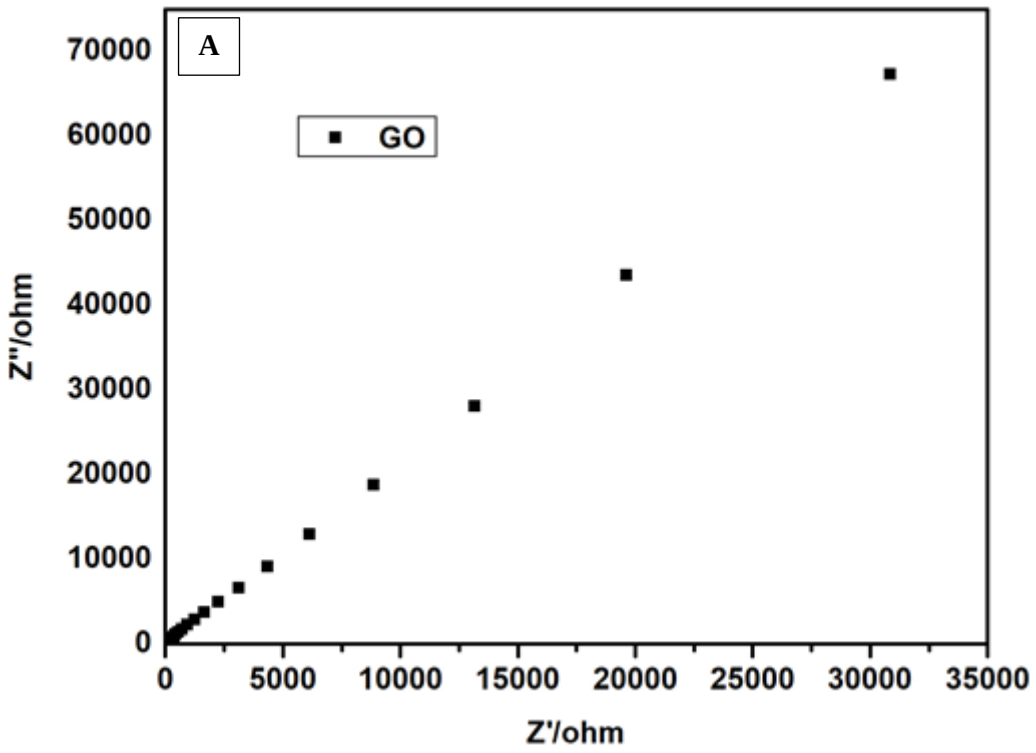

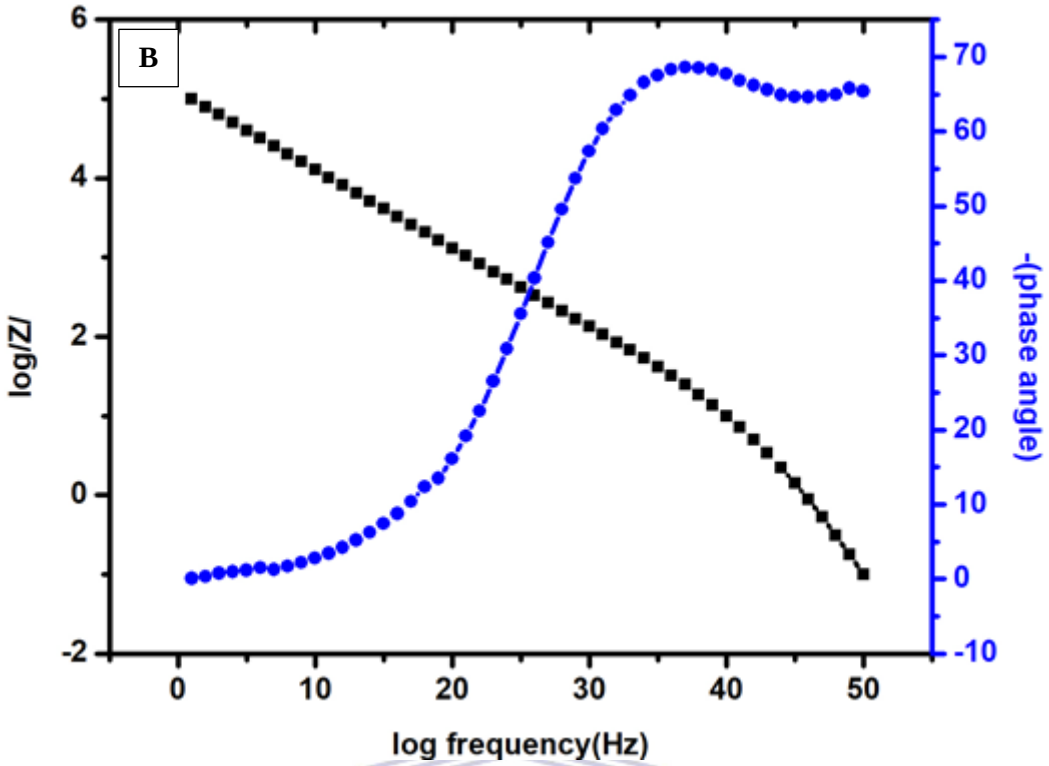

Figure 6.7 EIS data of GO (a) Nyquist plot and (b) Bode plot.

6.5. Conclusion

GO films were successfully prepared via modified Hummer method. The HR-TEM and HR-SEM analyses showed successful preparation of GO films with microscopic morphology. The thicknesses of the monolayer GO sheet were between 2 - 4 nm. The presence of oxygen-containing groups and characteristic peaks in FTIR analysis further determined the successful preparation of GO sheets. The presence of oxygen-containing functional groups provided more opportunities for potential applications of GO in many areas. This data will provide a reference to further studies in the synthesis of GO/Ag NPs composite for the preparation of immunosensor.

References

1. Pokpas, K., Zbeda, S., Jahed, N., Mohamed, N., Baker, P.G. and Iwuoha, E.I., 2014. Electrochemically reduced graphene oxide pencil-graphite in situ plated bismuth-film electrode for the determination of trace metals by anodic stripping voltammetry. *International Journal of Electrochemical Science*, *9*(2), pp.736-759.
2. Bao, Q., Zhang, D. and Qi, P., 2011. Synthesis and characterization of silver nanoparticle and graphene oxide nanosheet composites as a bactericidal agent for water disinfection. *Journal of colloid and interface science*, *360*(2), pp.463-470
3. Wu, T., Ma, J., Wang, X., Liu, Y., Xu, H., Gao, J., Wang, W., Liu, Y. and Yan, J., 2013. Graphene oxide supported Au–Ag alloy nanoparticles with different shapes and their high catalytic activities. *Nanotechnology*, *24*(12), p.125301.
4. Rose, A., Raghavan, N., Thangavel, S., Maheswari, B.U., Nair, D.P. and Venugopal, G., 2015. Investigation of cyclic voltammetry of graphene oxide/polyaniline/polyvinylidene fluoride nanofibers prepared via electrospinning. *Materials Science in Semiconductor Processing*, *31*, pp.281-286.
5. Kumar, N., Das, S., Bernhard, C. and Varma, G.D., 2013. Effect of graphene oxide doping on superconducting properties of bulk MgB2. *Superconductor Science and Technology*, *26*(9), p.095008.
6. Fathizadeh, M., Xu, W.L., Zhou, F., Yoon, Y. and Yu, M., 2017. Graphene Oxide: A Novel 2-Dimensional Material in Membrane Separation for Water Purification. *Advanced Materials Interfaces*, *4*(5).
7. Childres, I., Jauregui, L.A., Park, W., Cao, H. and Chen, Y.P., 2013. Raman spectroscopy of graphene and related materials. *New developments in photon and materials research*, *1*.

8. Ferrari, A.C., 2007. Raman spectroscopy of graphene and graphite: disorder, electron–phonon coupling, doping and nonadiabatic effects. *Solid state communications*, *143*(1), pp.47-57.
9. Ferrari, A.C., Meyer, J.C., Scardaci, V., Casiraghi, C., Lazzeri, M., Mauri, F., Piscanec, S., Jiang, D., Novoselov, K.S., Roth, S. and Geim, A.K., 2006. Raman spectrum of graphene and graphene layers. *Physical review letters*, *97*(18), p.187401.
10. Gupta, A., Chen, G., Joshi, P., Tadigadapa, S. and Eklund, P.C., 2006. Raman scattering from high-frequency phonons in supported n-graphene layer films. *Nano letters*, *6*(12), pp.2667-2673.
11. Stankovich, S., Dikin, D.A., Piner, R.D., Kohlhaas, K.A., Kleinhammes, A., Jia, Y., Wu, Y., Nguyen, S.T. and Ruoff, R.S., 2007. Synthesis of graphene-based nanosheets via chemical reduction of exfoliated graphite oxide. *carbon*, *45*(7), pp.1558-1565.
12. Li, X., Cai, W., An, J., Kim, S., Nah, J., Yang, D., Piner, R., Velamakanni, A., Jung, I., Tutuc, E. and Banerjee, S.K., 2009. Large-area synthesis of high-quality and uniform graphene films on copper foils. *Science*, *324*(5932), pp.1312-1314.
13. Chen, L., Tang, Y., Wang, K., Liu, C. and Luo, S., 2011. Direct electrodeposition of reduced graphene oxide on glassy carbon electrode and its electrochemical application. *Electrochemistry Communications*, *13*(2), pp.133-137.

Chapter 7

Results and Discussion: Graphene-silver (Ag NPs/GO) composites

7.1. Introduction

Synthesis and characterization of different types of nanoparticles have dramatically advanced over 20 years in the scientific world. The incorporation of metal nanoparticles with active carbon atoms has become a useful system for most applications. Hence the fabrication of metal nanocomposite has become a major challenge. The catalytic and optical properties of silver nanoparticles are useful for multiple range of applications such as catalysis, information storage, photonics, biological and chemical sensing and also surface enhancement Raman scattering [1]. By synthesizing and characterizing the metal nanoparticle with carbon active material into a single entity the catalytic performance of the material can be enhanced and the surface plasmon absorption of the composite (Ag NPs/GO) can be varied continuously [2]. On the other hand, the carbon active material which is graphene has attracted a great deal of attention due to a monolayer of graphene which has successful fabricated into being the active layer of nanomaterial surfaces [3]. Graphene oxide (GO) is known to be the derivative of graphene and it has been widely studied due to its unique properties and its convenient preparation on a large scale. GO has a large surface area and abundant functional groups on its surface which are used to provide binding sites for nanoparticles such as ZnO, Pt, Pd and Ag nanoparticles at which these nanocomposites provide a good photocatalytic and electrochemical properties [4].

Many monometallic nanoparticles such as Pt, Au, Ag and Pd have been successfully attached to graphene at which graphene supported bimetallic catalyst have been produced such as Au-Pt alloy attached to graphene [4]. This material has been found to have high stability for the oxidation state and high electro catalytic activity; hence nanomaterials are always deposited

onto the supporting material to form catalytic systems [5]. On the other hand metallic nanoparticles are known to be characterized by their electro catalytic ability together with the capacity for adsorption of biomolecules, high conductivity and biocompatibility. It is also known that functionalization of graphene to graphene oxide allows nanoparticles to firmly attach onto the graphene oxide surface with high support of dispersion hence enhancing the catalytic performance [6].

Despite their properties only few examples of the use of nanocomposite material with graphene can be found in literature in connection with the preparation of their use in electrochemical sensors this is due to poor stability and hard to reproduce because colloidal aggregation of Au, Pt, and Pd nanoparticles which became a major drawback for them to be used in sensors [7]. But then Ag nanoparticles instead of Pd, Pt or Au nanoparticles were used with graphene oxide to overcome the problem. The strong van der Waals forces between the graphene sheet and Ag nanoparticles help to reduce the nanoparticle aggregation since graphene has a large surface area [7].

7.2. Spectroscopic techniques

7.2.1. Ultraviolet–visible spectroscopy

Uv-visible spectroscopy refers to the ultraviolet radiation which is associated with the excitation of electrons in the atoms and molecules from lower energy level to higher energy level. When the energy levels are quanta the light with the exact amount of energy needed will cause transition from one level to another and be absorbed to get absorption band [8]. Ultraviolet–visible (UV–vis) absorption spectra were obtained using a Lambda 750S spectrometer (Perkin Elmer, Inc., USA) and UV–vis spectroscopy was used to monitor the formation of Ag NPs/GO.

The formation of Ag NPs/GO composites using GO and Ag NPs was confirmed by UV-vis spectra. Figure 7.1 shows the UV-vis spectrum of Ag NPs/GO at which an absorption spectra was found at 346 nm showing that the composite shifted towards the blue line of the spectrum. This peak corresponds to the surface plasmon resonance (SPR) absorption feature of the Ag NPs [9].

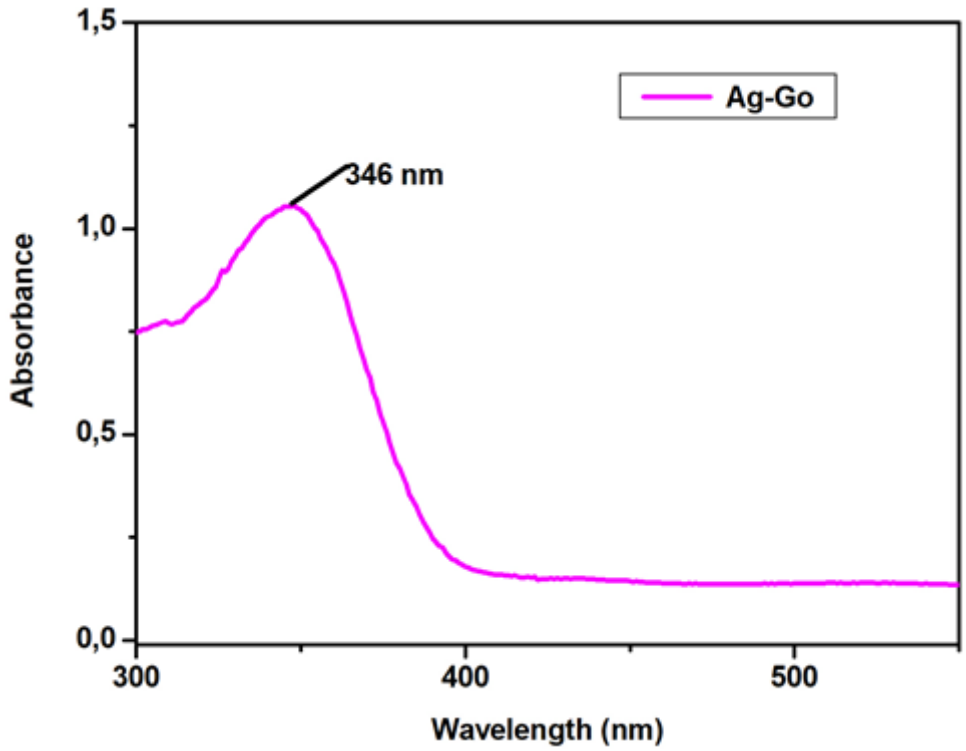

Figure 7.1 UV-vis spectroscopy of Ag NPs/GO composite dispersed in PBS solution.

7.2.2. Fourier Transform Infrared Spectroscopy (FTIR)

FTIR spectroscopy was used to verify the biomolecule-mediated Ag NPs/GO nanocomposite synthesis. The FTIR spectrum of Ag NPs/GO nanocomposite is shown in Figure 7.2. The spectrum shows dominant peaks at 1386, 2148 and 3442 cm^{-1}. The peak at 678 cm^{-1} corresponds to ring opening vibration while the transition vibration at 833 cm^{-1} corresponds to C-Cl stretching in the alkyl group due to the presence of Ag NPs in the composite [9]. The

stretching frequency around 1021 cm^{-1} corresponds to a stretching vibration from the C–O–C bonds of epoxy or alkoxy groups. The peak around 1120 cm^{-1} is attributed to C–OH bonds, while the peak centered at 1563 cm^{-1} is assigned to C=C bonds associated with the skeletal vibrations of unoxidized graphite domains. The transition band around 1629 cm^{-1} is attributed to C=O bonds in carboxylic acid [10] while the broad transition band around 3442 cm^{-1} corresponds to O-H group of water molecules found during the oxidation of GO. Ag NPs/GO composites shows a new band around 1386 cm^{-1}, resulting from the C–N stretching vibration of graphite-silver nitrate being reduced to Ag NPs/GO composite [11]. In addition, the Ag NPs/GO composite spectrum shows a significant decrease in the intensity of the adsorption bands of the oxygenated functional groups; this could result from the interaction of graphite that produces C=O groups on the surface, the presence of Ag on the GO surface, or the slight reduction of GO during the synthesis of the Ag NPs/GO nanocomposite. These results clearly demonstrate that GO was successfully exfoliated and reduced to graphene and that strong interactions may exist between Ag NPs and the remaining surface hydroxyl groups [11].

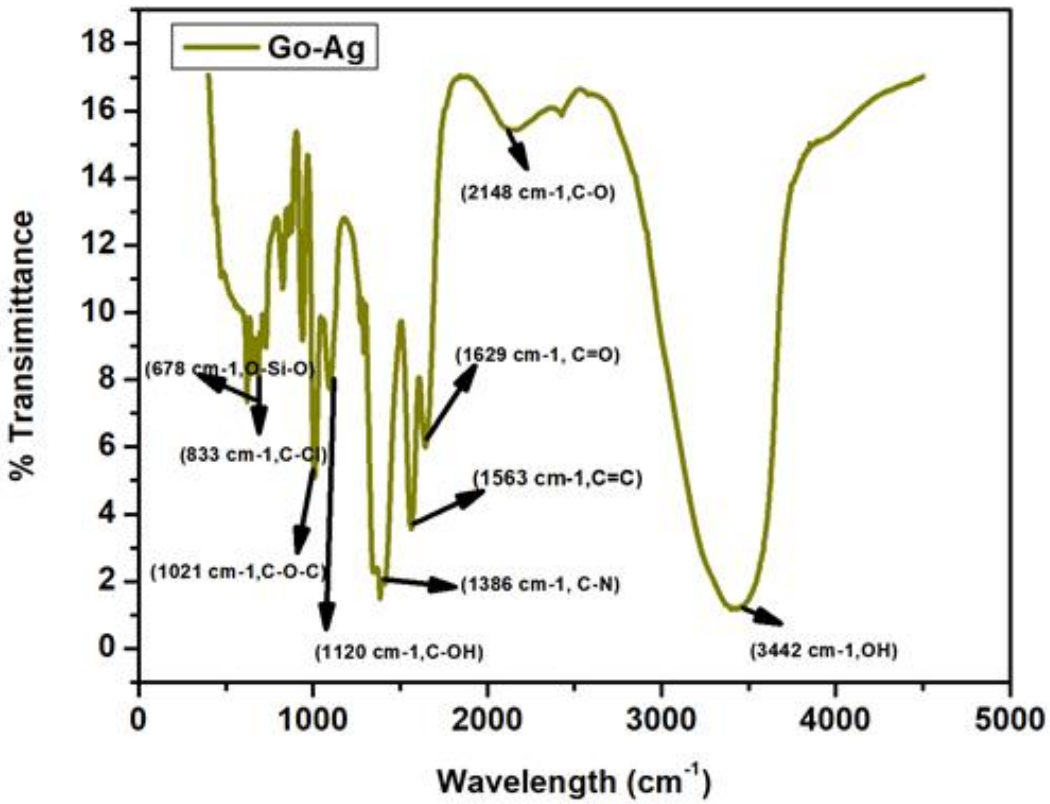

Figure 7.2: FTIR image of Ag NPs/GO composite.

7.3. Microscopic techniques

7.3.1. High resolution transmission electron microscopy (HR-TEM)

High transmission electron microscopy (HR-TEM) observations were carried out to observe the morphology of the Ag NPs/GO composites. Figure 7.3 (A) shows the HR-TEM images of the Ag NPs/GO composite synthesized room temperature for 60 min. Aliquots of Ag NPs/GO composite solutions were placed on a gold-coated copper grid (the reason for using gold instead of the normal carbon is due to the presence of a carbon material in the sample which might temper with the results) and allowed to dry under high temperature conditions and HR-TEM images were recorded. The nanoparticles on the composite tend to form aggregates on the GO sheets, and the GO sheets congregate together to form multilayer agglomerates as seen in the

image. Figure 7.3 (B) shows SAED of the Ag NPs/GO composite which indicates that the composite is more crystalline suggesting that the composites have no particular melting point. Figure 7.3 (C) shows particle size distribution of the Ag NPs in the composite. The nanoparticles in the Ag NPs/GO composite were found to be around 30 nm to 40 nm in diameter.

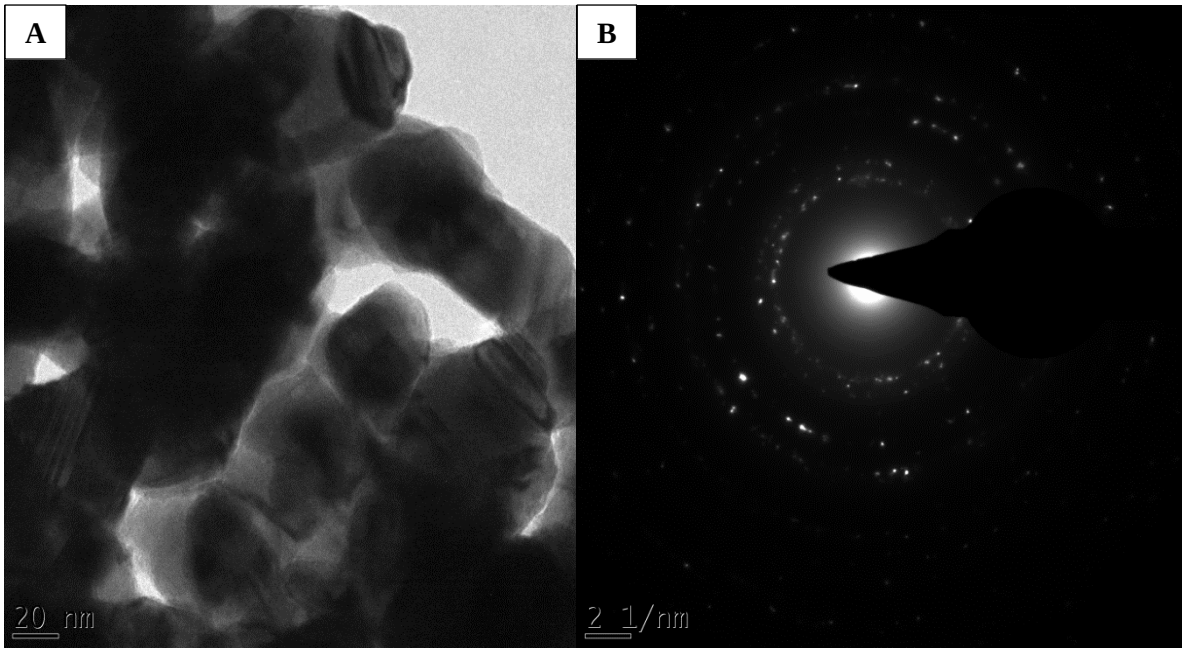

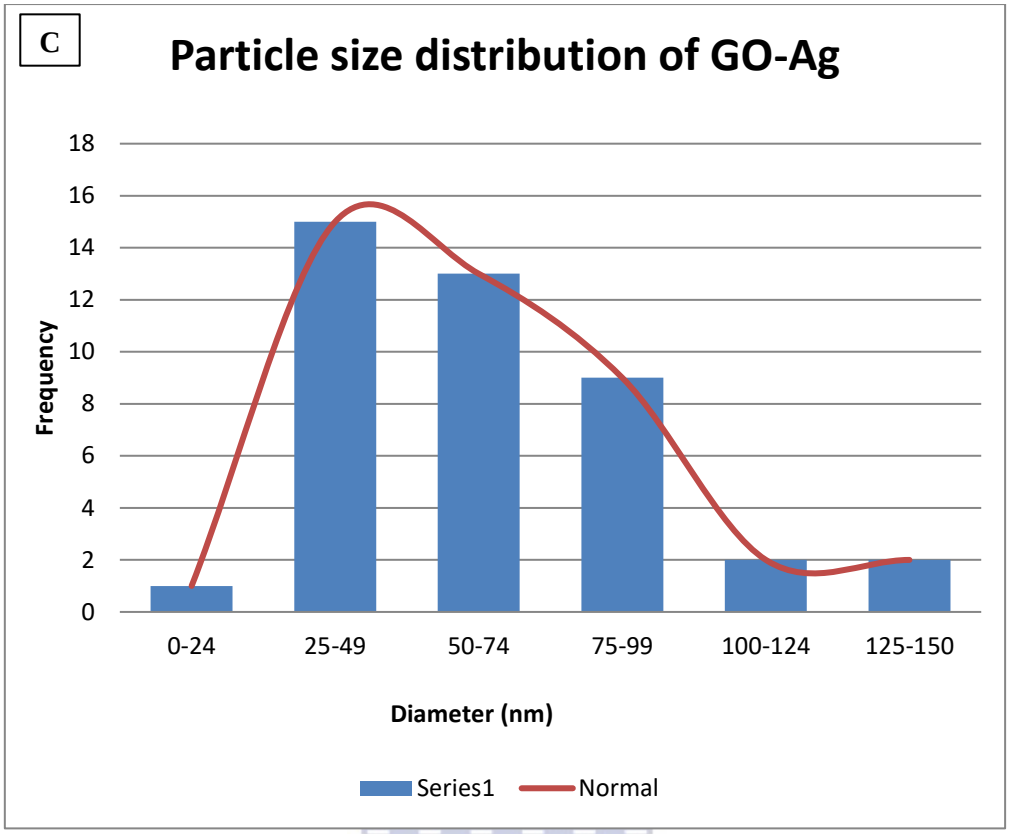

Figure 7.3: (A) HRTEM image, (B) SAED and (C) particle size distribution of Ag NPs/GO.

7.3.2. High resolution scanning electron microscopy (HR-SEM)

The size and morphologies of the prepared sample were examined by high resolution scanning electron microscopy (HR-SEM). Figure 7.4 (A) shows morphology images of Ag NPs placed on top of GO layers. The image shows that some silver nanoparticles are well dispersed on the surface of the GO sheets while few are aggregated on the GO sheets. Silver nanoparticles that are dispersed on the surface of the GO sheets exhibit a LSPR phenomenon and enhanced absorption of the visible light [12]. On the other hand Figure 7.4 (B) shows the EDS analysis of Ag NPs/GO composite. The EDS image shows carbon and oxygen elements which are from the carbon active material which is GO and Ag element from silver nitrate, thus this confirms the successful synthesis of Ag NPs/GO composite. Other elements observed in the EDS

analysis may be due to chemicals used during the synthesis of GO such as Cl and S, while copper is from the copper grids used during the characterization of the composite

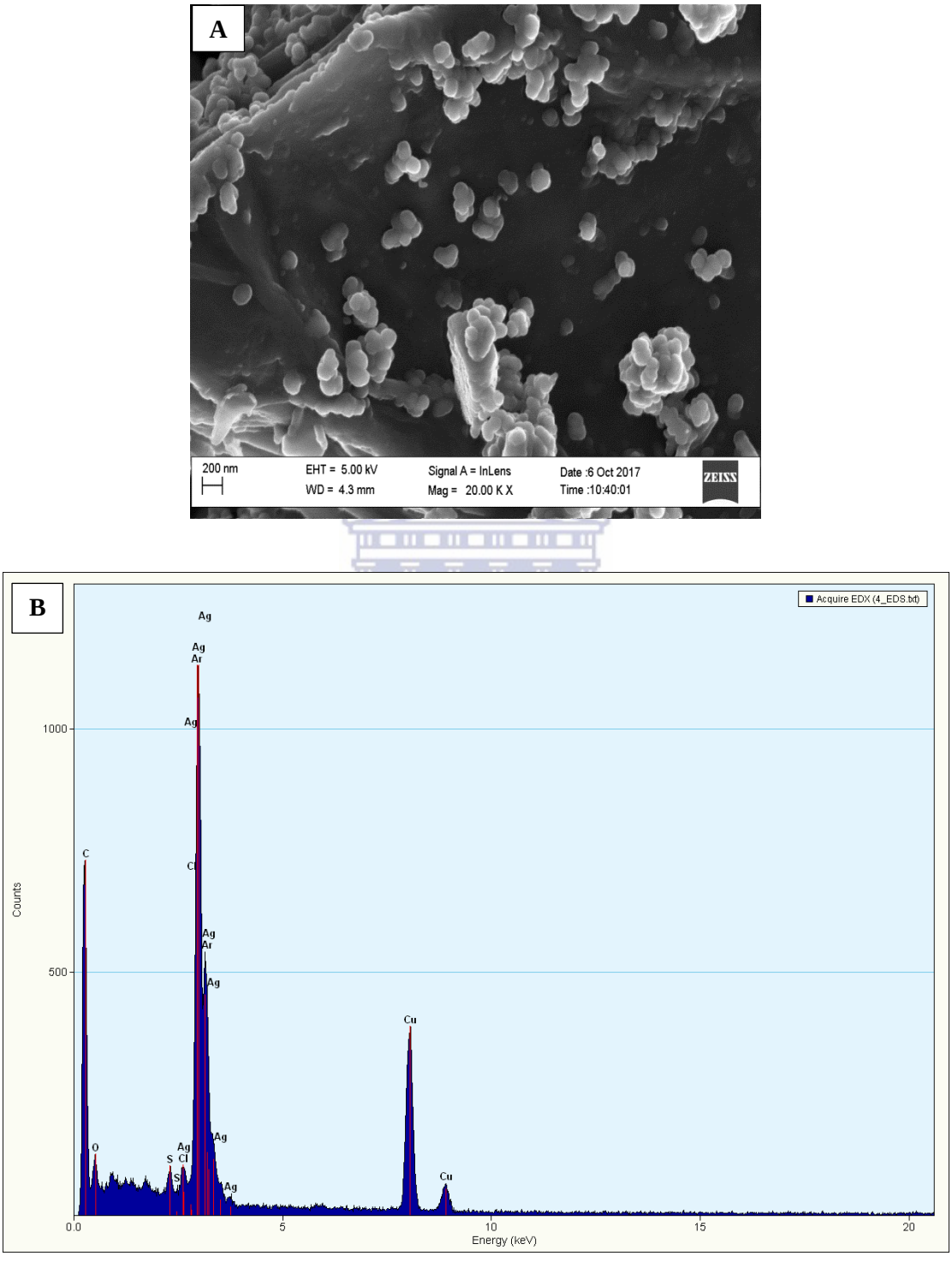

Figure 7.4: (A) HR-SEM image and (A) EDS of Ag NPs/GO.

7.4. Electrochemistry of graphene-silver composites Ag NPs/GO

7.4.1. Cyclic voltammetry (CV)

In this section we discuss the behaviour of the synthesized Ag NPs/GO attached onto the GCE surface. The nanocomposite was attached on the electrode by drop-coating it onto the surface of the electrode and left overnight to dry before the characterization using CV starts. This was performed at different scan rates and the peak current for the oxidation process depends linearly on the scan rate that is as the scan rate increases: the peak tend to absorb linearly. The electrochemical behaviour of Ag NPs/GO composite was tested using CV. Figure 7.5 (A) shows the CV of Ag NPs/GO composite which has an anodic peak shifting to the left while the cathodic peak shifting to the right as the scan rate increases. The shift of current and potential shows that the composite is conductive and that there is electron flow within the composite [12]. The cathodic peak identified to be shifting towards the right may be due to the reduction of electrochemically active oxygen-containing groups on the graphene planes [11]. It can be also be the attributed to the reduction of Ag^{+} to form metallic Ag [12]. Moreover, the reduction current increases with the increase of Ag NPs indicating the presence of an increasing amount of loading material of Ag NPs on the surface of the GO. The cathodic peak that shifted to the positive direction can have a good impact on the composite by having a higher stability.

Moreover a graph of current versus the square root of scan rate for the cathodic peak (Figure 7.5 (B)) was plotted in order to assist in the determination of the diffusion coefficient and surface concentration. The slope was determined to be 218.95 V/s with R^2 being 0.7261. Using the Brown Anson equation (Equation 4.1), the surface concentration (Γ* Ag NPs/GO) was determined to be 1.2 x 10^{-2} mol cm^{-1} and using the Randel-Sevcik Equation (Equation 4.2), the diffusion coefficient of Ag NPs/GO was determined to be 7.74 x 10^{-9} cm^2/s.

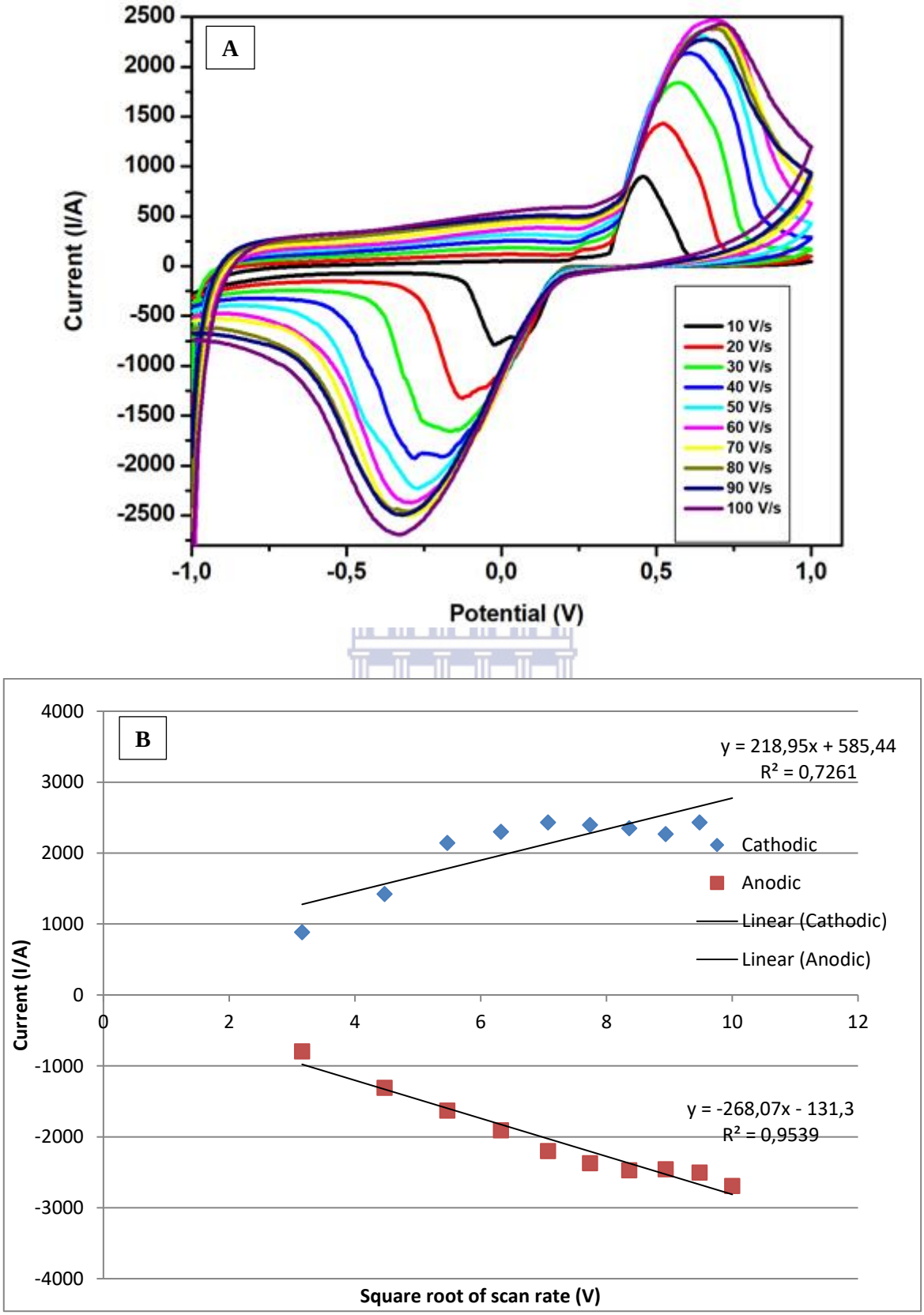

Figure 7.5: (A) CV of the synthesized Ag NPs/GO and (B) Graph of current vs the square root of scan rate Ag NPs/GO.

7.4.2. Electrochemical Impedance (EIS)

The Nyquist plot in Figure 7.6 (A) shows a nearly straight line graph with a small semi-circle around 20098 Ω, which might be due to the capacitance of the composites. In figure 7.6 (B) the change in phase angle in the Bode plot of frequency 0 - 50 Hz, the electrode shows a two phase shift of 74.24 ^{0} and 67.79 ^{0} at frequency of ~34 and 50 Hz respectively. The phase shift at higher and lower frequency corresponds to the capacitive and diffusive characteristics of GO. While the phase shift ~71.65 ^{0} at a frequency of 47 Hz corresponds to the capacitive behaviour of Ag nanoparticles with no diffusive characteristic indicating a moderate heterogeneous feature of the modified electrode with Ag NPs/GO composite.

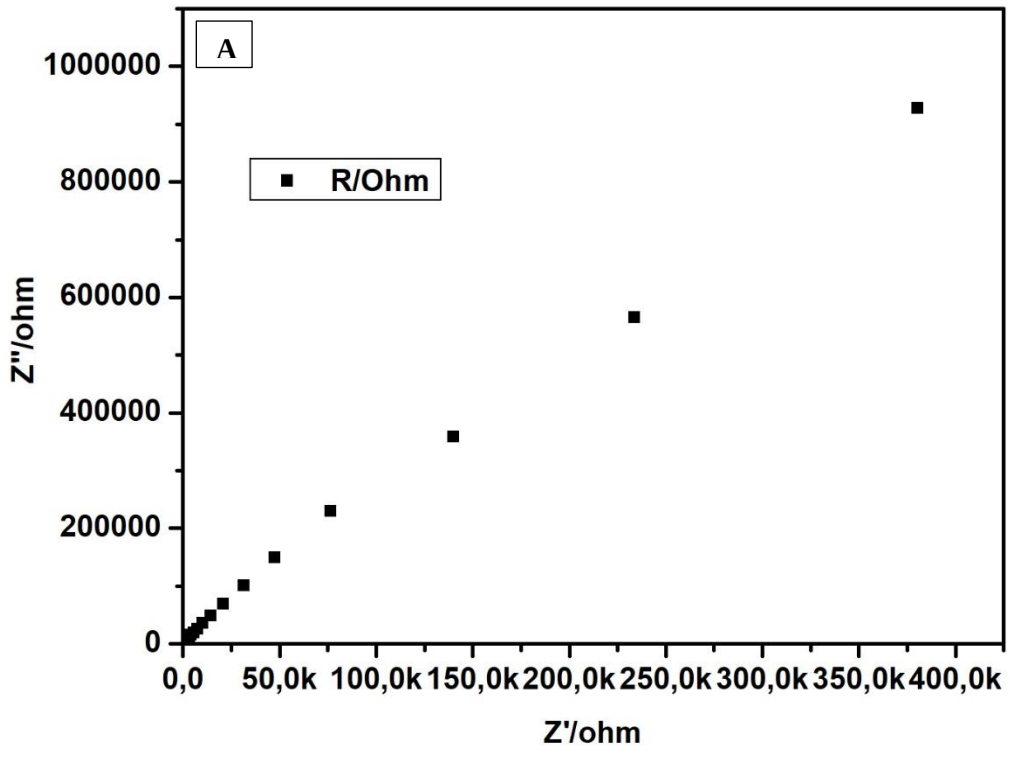

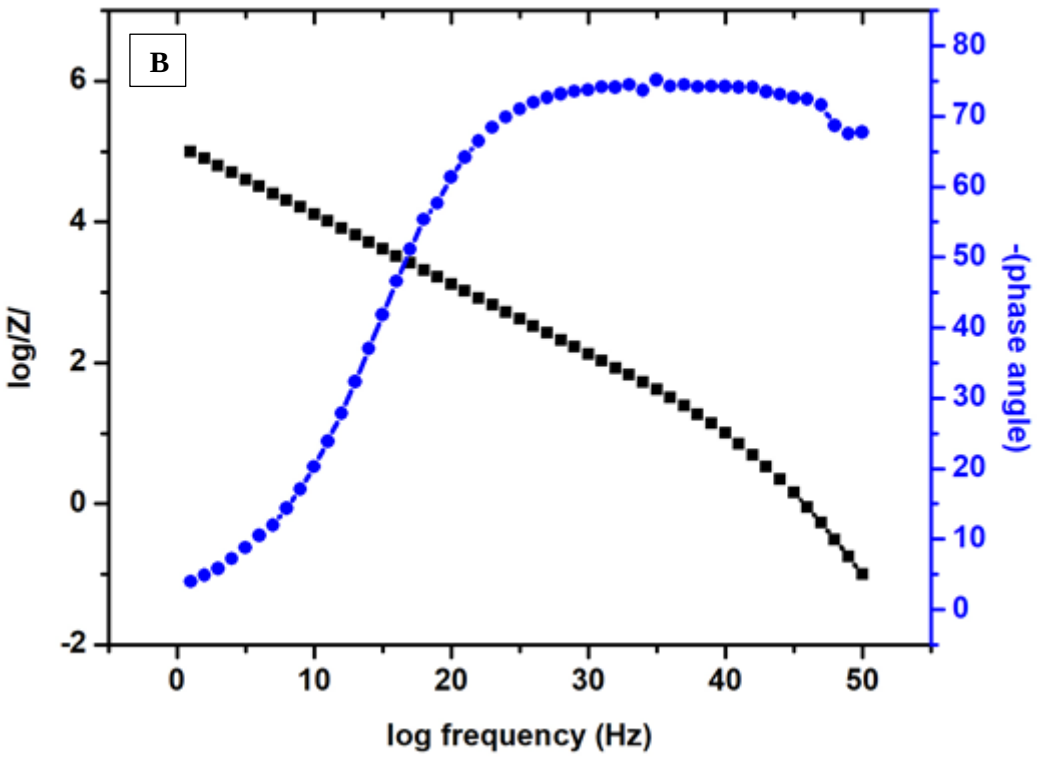

Figure 7.6: EIS of Ag NPs/GO composite (A) Nyquist plot and (B) Bode plot.

7.5. Electrochemical detection of ESAT-6 immunosensor

ESAT-6 immunosensors were developed using Ag NPs/GO nanocomposite and used for the detection of anti-ESAT-6 antigens. Figure 7.7 (A) shows a CV graph at different scan rates of the immunosensor where Ag NPs/GO composites were immobilised with ESAT-6 antibodies; while Figure 7.7 (B) shows EIS Nyquist plot of the developed immunosensor confirming the findings of Figure 7.7 (A) The detection of the antigen anti-ESAT-6 is shown in Figure 7.7 (C) and (D). Figure 7.7 (C) shows the detection of the antigens using the developed immunosensor using CV where different concentrations of anti-ESAT-6 was analysed at the concentration range of 0.05 to 0.2 ug/ul. Confirmation of these finding was achieved using EIS as seen in Figure 7.7 (D).

Furthermore a linear graph of R_{ct} (Ag NPs/GO / ESAT-6) versus concentration of anti-ESAT-6 was plotted for determination of limit of detection (LOD) and percentage error of the immunosensor as well as the circuit for the sensor, as shown in Figure 7.7 (E).The calculated LOD was determined to be 0.058408 ′Ω/µl. It was observed that the curves recorded in Figure 7.7 (D) overlap at all concentrations. For low concentrations the impedance spectrum includes only the straight line, which can be attributed to a very fast transfer of electron (small R_{ct}) [14]. At higher concentrations the imaginary part of the impedance depends upon the number of molecules that diffuses toward the electrode and its value significantly decreases with the increase of anti-ESAT-6 concentration. In addition, the accumulation of oxidation products at electrode surface hinders the transfer of electrons and leads to a large R_{ct} (107260 Ω) as compared to GO (8745 Ω) and Ag NPs (10114 Ω). Furthermore by comparing the work previously done by other scientist based on ESAT-6 immunosensor, one can conclude that the developed immunosensor in this study is effective as seen from the recorded LOD's as it is within the expected value compared to previously done ESAT-6 immunosensors. Table 2 below illustrates these findings

Table 2: Summary of the developed Antigen-based immunosensor for TB diagnosis using ESAT-6.

Target antigens	**Bio recognition element**	**Mechanism of transduction**	**Detection limit**	**References**
ESAT-6 lipoarabinomannan Ag 85	antibody	Waveguide based optical biosensor	$5.0x10^{-10}$ mg/ml	16
ESAT-6	antibody	Physical vapour deposition bioelectrochemical	$5.0x10^{-7}$ mg/ml	17
ESAT-6,MTb CFP	antibody	Square wave voltammetry electrochemical	$7.0x10^{-6}$ mg/ml	15
ESAT-6	antibody	Impedance electrochemical	$5.0x10^{-4}$ mg/µl	Current work

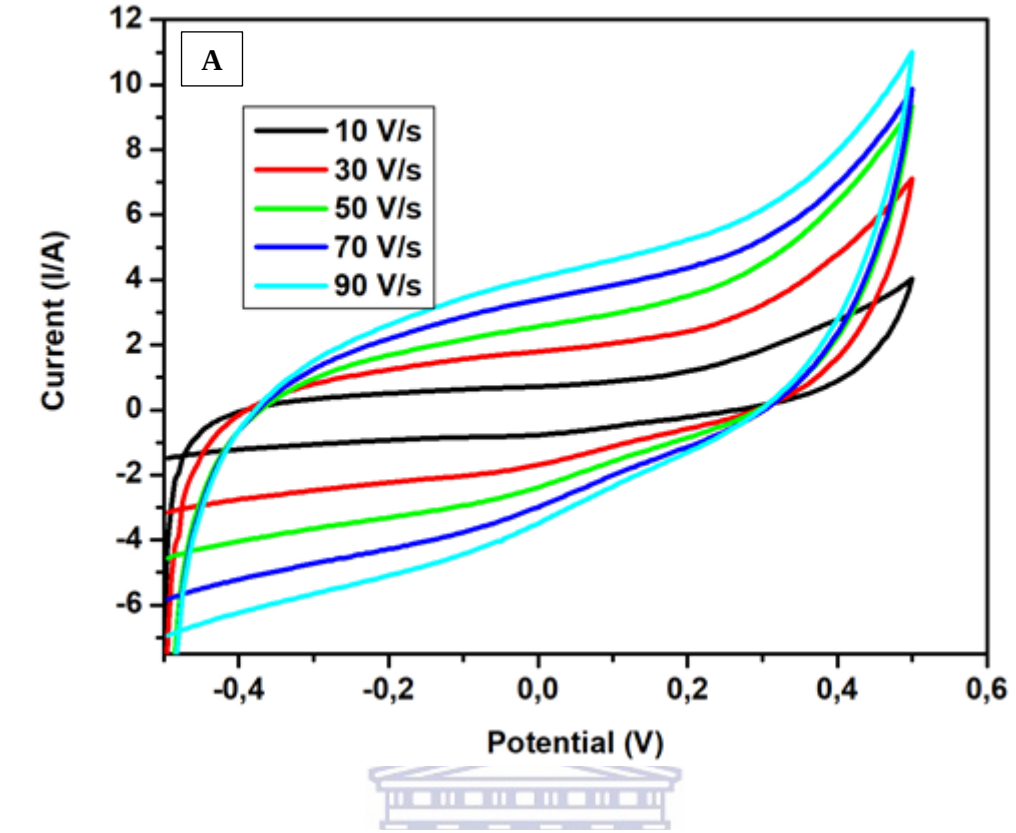

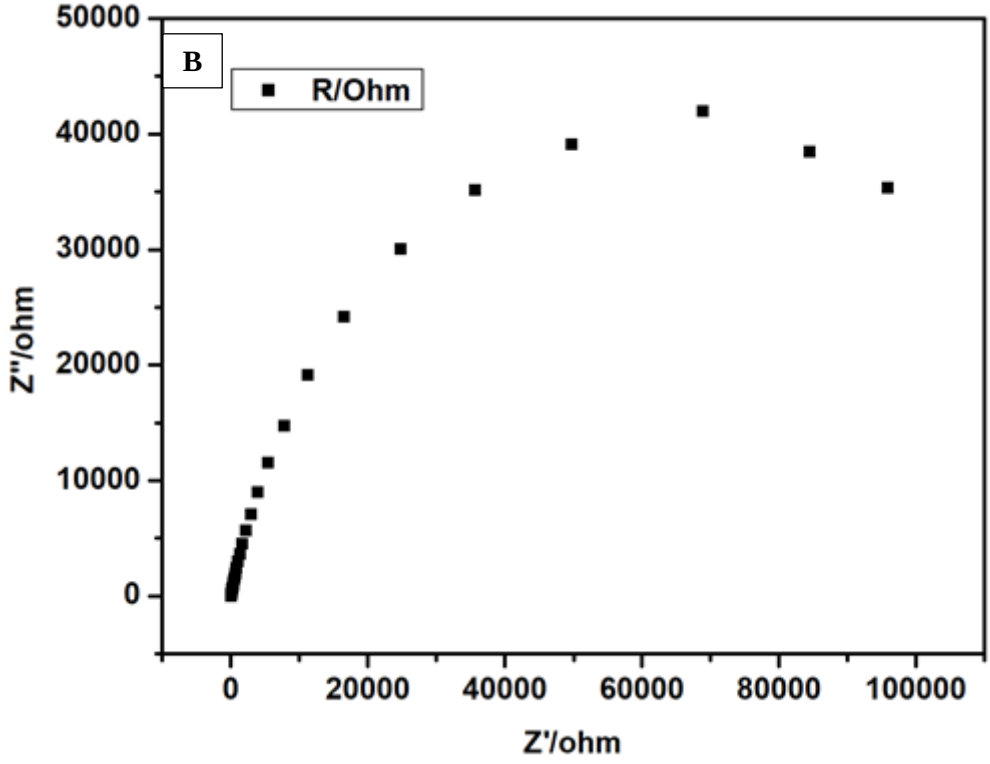

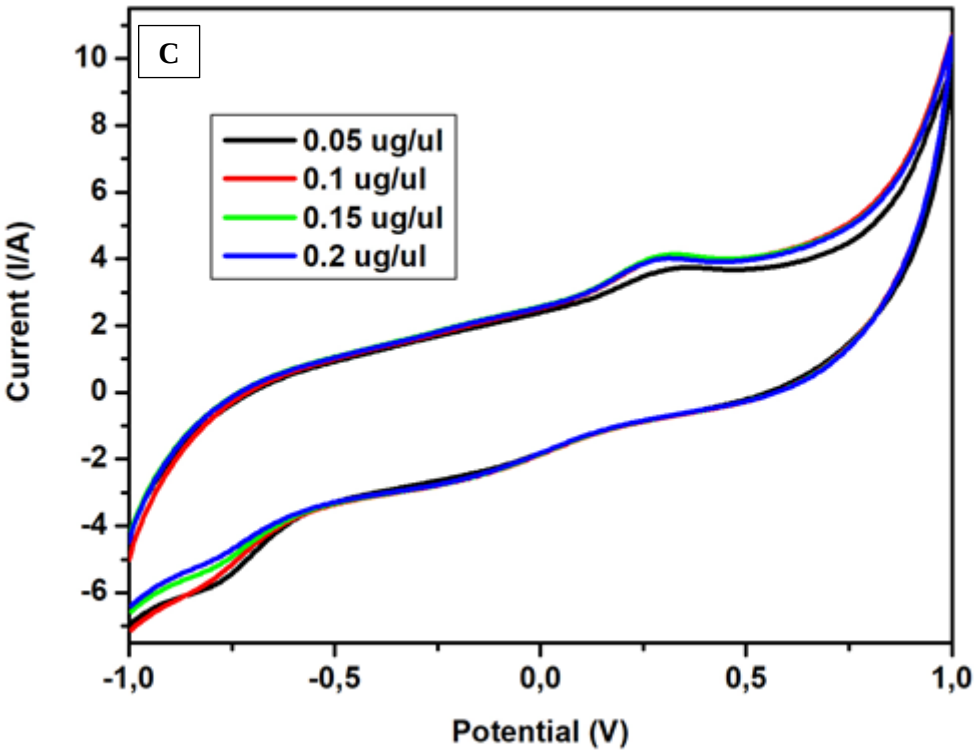

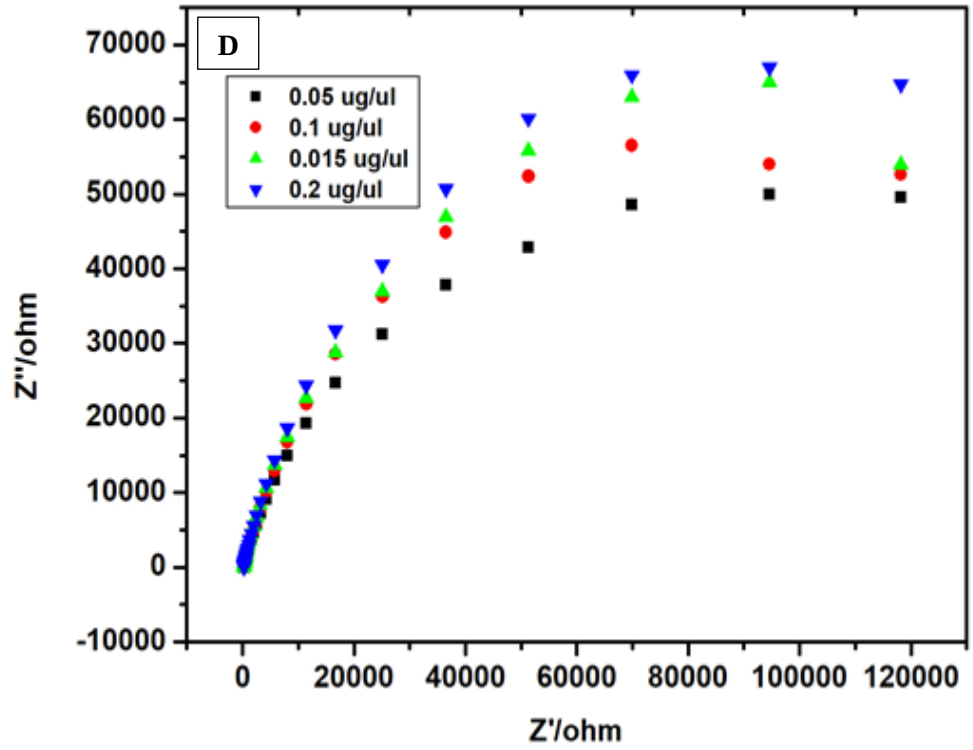

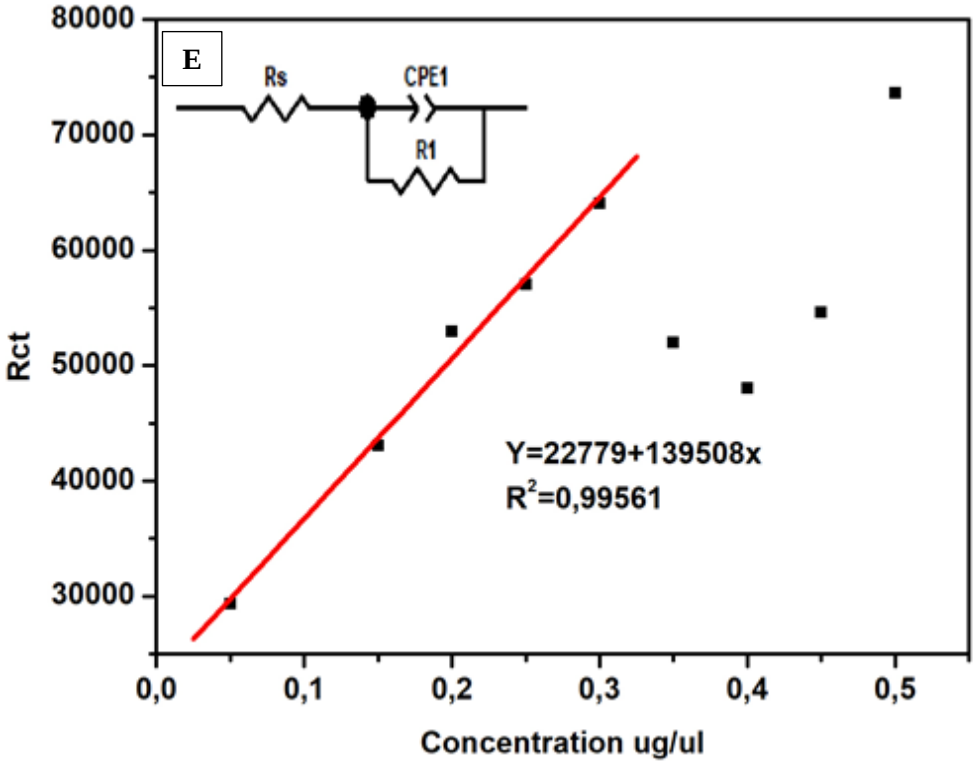

Figure 7.7: (A) CV of immunosensor development for Ag NPs/GO /ESAT-6 composite at different scan rates; (B) EIS of immunosensor development for Ag NPs/GO /ESAT-6 composite; (C) CV of immunosensor detection of different concentrations of anti-ESAT-6; (D) Figure 7.7 (d): EIS of immunosensor detection of anti-ESAT-6; (E) linear graph of Rct (Ag NPs/GO/ESAT-6) vs concentration of anti-ESAT-6

7.6. Conclusion

Graphene based nanomaterial created unmatched curiosity in the scientific world. The unique structure of its kind not only marked its cavity in the field of electronics (optoelectronics, printed electronics) and energy storages devices but also created a stir in sensing region with incorporation of plasmonic, optically and electrochemically active silver nanoparticles. The different shape and size of silver nanostructures shows excellent properties decorated on the graphene based nanomaterials have an ability to form an intimate contact with graphene to form an atomically smooth layer. The mechanistic aspects of Ag NPs/GO nanocomposites imputing towards improving electrochemical immunosensors are understood to be the contribution of both individual structures. The morphological and electrochemical behaviour

of the composites was investigated and proved by HR-TEM and CV respectively which allowed us to develop an immunosensor using CV and EIS. The LOD found was to be 5.0 $x10^{-4}$ mg/µl which confirms that the development and detection of an immunosensor was successful since the LOD is equivalent to the starting concentration used in the detection of anti-ESAT-6.

References

1. Li, J., Kuang, D., Feng, Y., Zhang, F., Xu, Z., Liu, M. and Wang, D., 2013. Green synthesis of silver nanoparticles–graphene oxide nanocomposite and its application in electrochemical sensing of tryptophan. *Biosensors and Bioelectronics*, *42*, pp.198-206.
2. Golsheikh, A.M., Huang, N.M., Lim, H.N., Zakaria, R. and Yin, C.Y., 2013. One-step electrodeposition synthesis of silver-nanoparticle-decorated graphene on indium-tin-oxide for enzymeless hydrogen peroxide detection. *Carbon*, *62*, pp.405-412.
3. Novoselov, K.S., Geim, A.K., Morozov, S.V., Jiang, D., Zhang, Y., Dubonos, S.V., Grigorieva, I.V. and Firsov, A.A., 2004. Electric field effect in atomically thin carbon films. *science*, *306* (5696), pp.666-669.
4. Lee, C., Wei, X., Kysar, J.W. and Hone, J., 2008. Measurement of the elastic properties and intrinsic strength of monolayer graphene. *science*, *321*(5887), pp.385-388.
5. Balandin, A.A., Ghosh, S., Bao, W., Calizo, I., Teweldebrhan, D., Miao, F. and Lau, C.N., 2008. Superior thermal conductivity of single-layer graphene. *Nano letters*, *8*(3), pp.902-907.
6. Pruneanu, S., Pogacean, F., Biris, A.R., Coros, M., Watanabe, F., Dervishi, E. and Biris, A.S., 2013. Electro-catalytic properties of graphene composites containing gold or silver nanoparticles. *Electrochimica Acta*, *89*, pp.246-252.
7. Azevedo, J., Bourdillon, C., Derycke, V., Campidelli, S., Lefrou, C. and Cornut, R., 2013. Contactless surface conductivity mapping of graphene oxide thin films deposited on glass with scanning electrochemical microscopy. *Analytical chemistry*, *85*(3), pp.1812-1818.
8. Sundaram, R.S., Gómez-Navarro, C., Balasubramanian, K., Burghard, M. and Kern, K., 2008. Electrochemical modification of graphene. *Advanced Materials*, *20* (16), pp.3050-3053.

9. Zhou, Y., Yang, J., He, T., Shi, H., Cheng, X. and Lu, Y., 2013. Highly stable and dispersive silver nanoparticle–graphene composites by a simple and low energy consuming approach and their antimicrobial activity. *Small*, *9* (20), pp.3445-3454.
10. Stankovich, S., Dikin, D.A., Piner, R.D., Kohlhaas, K.A., Kleinhammes, A., Jia, Y., Wu, Y., Nguyen, S.T. and Ruoff, R.S., 2007. Synthesis of graphene-based nanosheets via chemical reduction of exfoliated graphite oxide. *carbon*, *45*(7), pp.1558-1565.
11. Fan, X., Peng, W., Li, Y., Li, X., Wang, S., Zhang, G. and Zhang, F., 2008. Deoxygenation of exfoliated graphite oxide under alkaline conditions: a green route to graphene preparation. *Advanced Materials*, *20*(23), pp.4490-4493.
12. Du, M., Xiong, S., Wu, T., Zhao, D., Zhang, Q., Fan, Z., Zeng, Y., Ji, F., He, Q. and Xu, X., 2016. Preparation of a microspherical silver-reduced graphene oxide-bismuth vanadate composite and evaluation of its photocatalytic activity. *Materials*, *9*(3), p.160.
13. Wang, A., Shen, S., Zhao, Y. and Wu, W., 2015. Preparation and characterizations of BiVO 4/reduced graphene oxide nanocomposites with higher visible light reduction activities. *Journal of colloid and interface science*, *445*, pp.330-336.
14. Xu, L., Wei, Y., Guo, W., Guo, Y. and Guo, Y., 2015. One-pot solvothermal preparation and enhanced photocatalytic activity of metallic silver and graphene co-doped BiVO 4 ternary systems. *Applied Surface Science*, *332*, pp.682-693.
15. Diouani, M.F., Ouerghi, O., Refai, A., Belgacem, K., Tlili, C., Laouini, D. and Essafi, M., 2017. Detection of ESAT-6 by a label free miniature immuno-electrochemical biosensor as a diagnostic tool for tuberculosis. *Materials Science and Engineering: C*, *74*, pp.465-470.
16. Mukundan, H., Kumar, S., Price, D.N., Ray, S.M., Lee, Y.J., Min, S., Eum, S., Kubicek-Sutherland, J., Resnick, J.M., Grace, W.K. and Anderson, A.S., 2012. Rapid detection of

Mycobacterium tuberculosis biomarkers in a sandwich immunoassay format using a waveguide-based optical biosensor. *Tuberculosis*, *92*(5), pp.407-416.

17. Sepulveda, D., Aroca, M.A., Varela, A., Del Portillo, P. and Osma, J.F., 2017. Bioelectrochemical Detection of Mycobacterium tuberculosis ESAT-6 in an Antibody-Based Biomicrosystem. *Sensors*, *17*(10), p.2178.

Chapter 8

Results and discussion: Graphene-zinc (ZnO NPs/GO) composite

8.1. Introduction

Graphene oxide is known as a single 2D carbon sheet with the similar structure as of that individual layers found in graphite. It has been discovered that it has broad scientific activities due to its extraordinary electrical, thermal, and mechanical properties [1]. Graphene-nanocomposites are prominent class of exciting materials that hold promise for many applications. Potential applications of graphene –based nanomaterial are explore by decorating graphene sheets with inorganic nanoparticles such as sulphides and metal oxides which are semi-conductive to the material [2]. It has been reported that several graphene-inorganic nanocomposites have been successfully synthesized and show desirable combinations of these properties which is not possible to find on a single component. As part of metal oxide nanomaterial zinc oxide is known to be the one that possesses many potential application in the field of sensors, transistors, emission display and photocatalysis due to its large band gap and large exciting binding energy [3]. In the research conducted by Zhu and co-workers for the synthesis of heterojunction of ZnO nanocrystals with carbon nanotubes (CNTs) revealed that the ZnO/CNTs nanocomposites can enlarge the applications and reinforce the immaculate properties of composed ZnO and CNTs material [4]. In comparison with CNTs GO has similar physical properties but larger surface area which is known as an unrolled CNT [4]. However the production cost of GO sheets in large quantities is much lower than that of CNTs hence GO is labelled as a low cost alternative to CNTs in nanocomposites. Recently an effective one-pot reaction method in which GO sheets and precursor of nanoparticles are subjected to successive chemical reactions in just one reactor, has been reported to prepare graphene/nanoparticles composites but possess danger to environment. Hence in this study we synthesize GO/ nanomaterial using a chemical method.

8.2. Spectroscopic techniques

8.2.1. UV-vis spectroscopy

Uv-vis spectroscopy in this chapter was used to measure the absorption wavelength of ZnO NPs/GO composite using light which passes through the sample in the visible areas.

Figure 8.1 below shows UV–vis absorption spectra of the ZnO NPs/GO composite. It can be observed that the spectra exhibit a characteristic absorption peak at 210 nm, indicating the existence of highly crystallized GO sheets. The spectrum shows relatively lower absorption intensity in the visible region. The absorption of ZnO NPs/GO composites in the visible light region decreases along with the addition of GO content during the preparation.

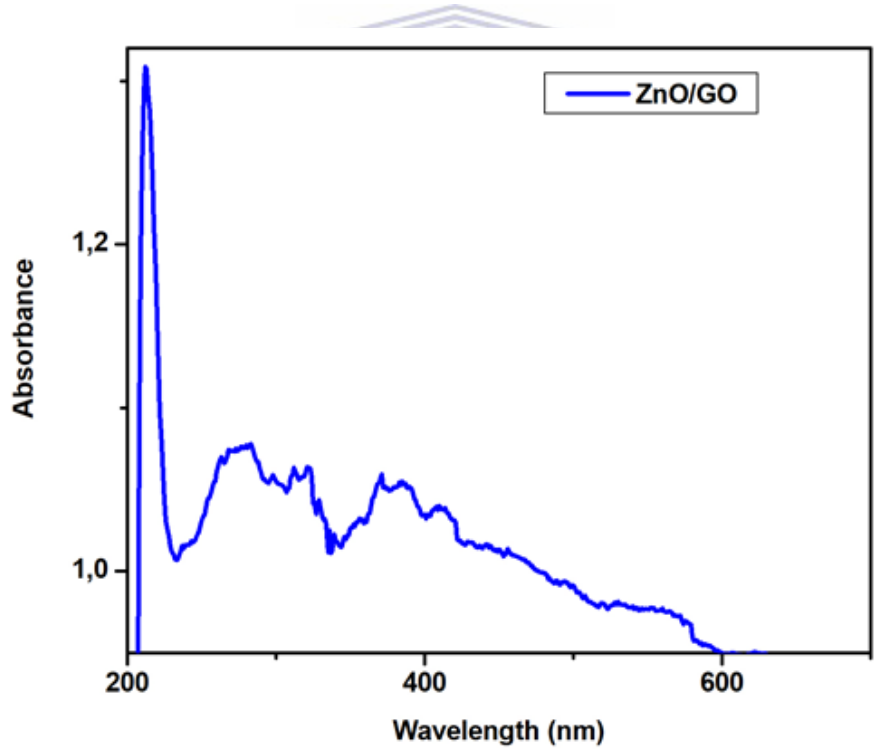

Figure 8.1: UV-vis spectrum of ZnO NPs/GO dispersed in PBS solution.

8.3. Microscopy techniques

8.3.1. HRTEM microscopy

Morphology of ZnO-GO composite was investigated by using HR-TEM microscopy as seen in Figure 8.2 (A). Aliquots of ZnO NPS/GO solution was placed on a gold-coated copper grid and allowed to dry under high temperature conditions and HR-TEM images were recorded. The HR-TEM micrograph shows that the size of the nanoparticles layered on top of graphene sheets were approximately 50 nm in diameter size at which the ZnO nanoparticles are evenly dispersed on top of the GO sheet layers. The shape of the nanoparticles in the composite are found to be rods, spherical and cubes. On the other hand Figure 8.2 (B) shows the SAED of ZnO NPs/GO nanocomposites which indicates the crystalline of the composite while Figure 8.2 (C) indicate the particle size distribution of the composite with nanoparticles ranging from 0 nm to 124 nm in particle size, and the diameter size of the nanoparticles is found to be around 50nm.

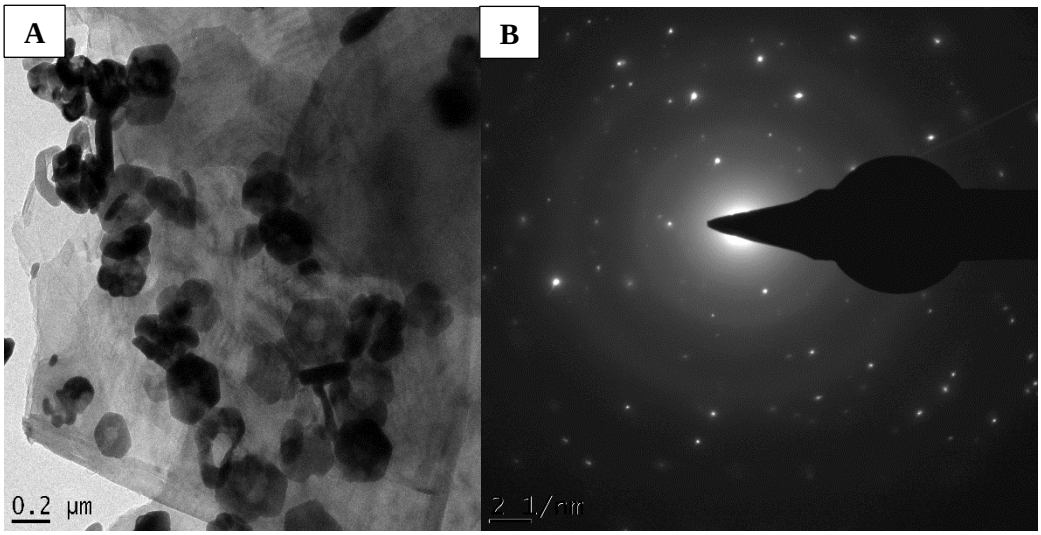

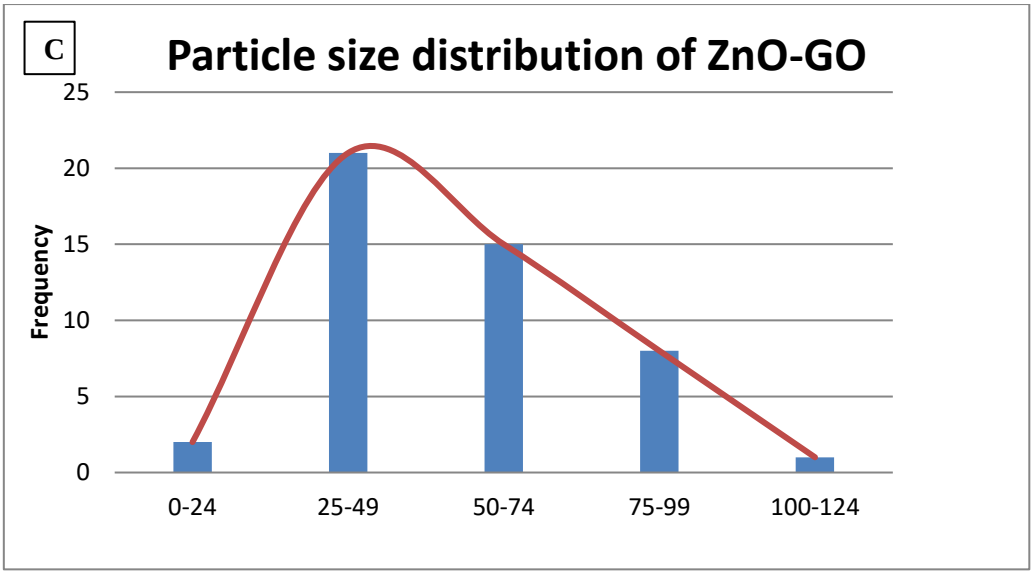

Figure 8.2 (a) HRTEM image, (b) SAED and (c) particle size distribution of ZnO NPs/GO.

8.3.2. High resolution scanning electron microscopy (HR-SEM)

The morphology of ZnO NPs/GO composite was studied using HR-SEM to complement the imaging found in HR-TEM in-terms of particle shape. Figure 8.3 (a) shows HR-SEM image of ZnO NPs/GO nanocomposites with the nanoparticles rested on the GO sheets. The GO sheets in the image are closely packed on top of each other while the nanoparticles are congregated on the sides of the sheets, the shape of the nanoparticles complement the HRTEM image above they are spherical, cubical and few rods. Controlling the morphology of nanoparticles is of key importance for exploiting their properties for their use in several emerging technologies. Optical filters and bio-sensors are among the many applications that use optical properties of nanoparticles and it requires anisotropy of the particle shape as larger shapes produce greater plasmon losses [6]. On the other side Figure 8.3(b) shows the EDS image analysis of ZnO NPs/GO composite. The EDS image shows a carbon and oxygen elements which are from the carbon active material which is GO, oxygen element is also reflect the presence of Oxygen in zinc oxide element and Zn element which is from zinc nitrate, thus this confirms the successful

synthesis of ZnO NPs/GO composite. The sulphur elements observed in the EDS analysis may be due to sulphuric acid used during the synthesis of GO, while copper is from the copper grids used during the characterization of the composite.

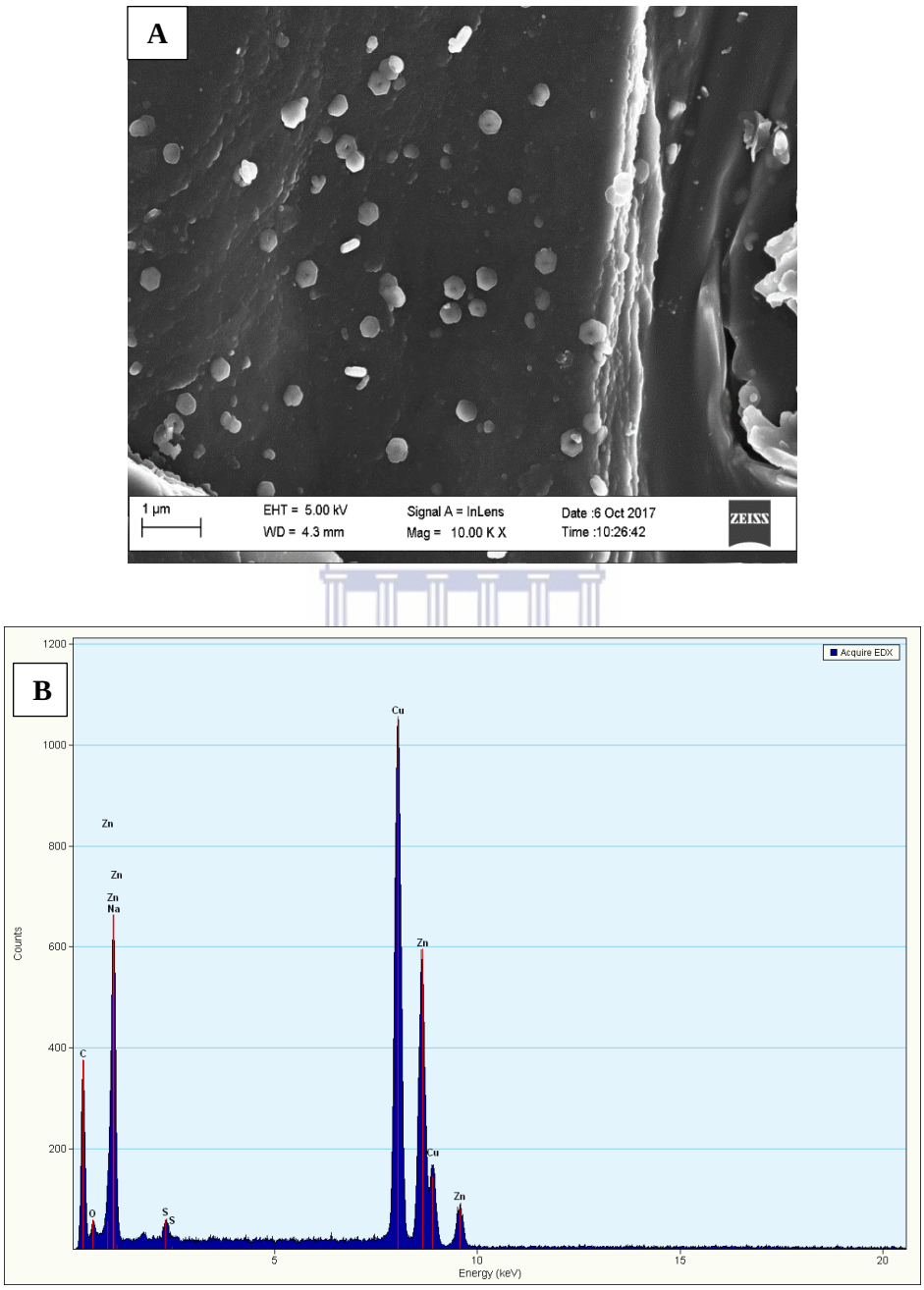

Figure 8.3: (a) HR-SEM image and (b) EDS of ZnO NPs/GO.

8.4. Electrochemical techniques

8.4.1. Cyclic voltammetry

In this section we discuss the behaviour of ZnO NPs/GO attached onto the GCE surface. The composite was attached on the electrode by drop-coating it onto the surface of the electrode and left overnight to dry before characterization using cyclic voltammetry (CV). The conductive performances of the materials were further evaluated by cyclic voltammetry (CV) in 0.1 M pH 7.4 PBS electrolyte. The CV was run at different scan rates at the potential ranging from 10 V to 100 V as represented in Figure 8.4 (A). As seen from the figure the curve is partially circular which shows deviation from an ideal circular shape with some redox peaks due to addition of ZnO in the reaction, an indication of the charge transfer nature of the material. Observed in the figure is also the fact that the current level increases with the increase of scan rates for the ZnO NPs/GO composite. Figure 8.4 (B) indicates a plot of current versus the square root of scan rate to aid the calculation of the surface concentration and diffusion coefficient of the composite.

The cathodic and anodic slopes have been calculated to be 0.900 and -1.433 V/s respectively. The plot shows a clear indication of the dependence of the peaks current on scan rate; as the scan rate increases the current also increases an indication of conductivity and electron transfer. From the calculated slope, the surface concentration of ZnO NPs/GO composite was determined using the Brown Anson equation (equation 6.1). From the equation, n is the number of electron transferred (n =2), F is the faraday constant (96485 C mol^{-1}), Γ*ZnO NPS/GO represent the surface concentration of the composite (mol cm^{-1}), A is the surface area of the glassy-carbon electrode (0.0201 cm^2), υ is the scan rate (mV s^{-1}), R is the gas constant (8.314 J mol^{-1} K^{-1}) and T is the operating absolute temperature of the system (25 °C T in 298 K). Thus the he surface concentration (Γ*ZnO NPs/GO) of the composite was determined to be

$5.31x10^{-6}$ mol cm^{-1}. Additionally, the Randel-Sevcik Equation (Equation 6.2) was used to determine the diffusion coefficient of the ZnO NPs/GO composite where a value of $3.13x10^{-26}$ cm^2/s was determined.

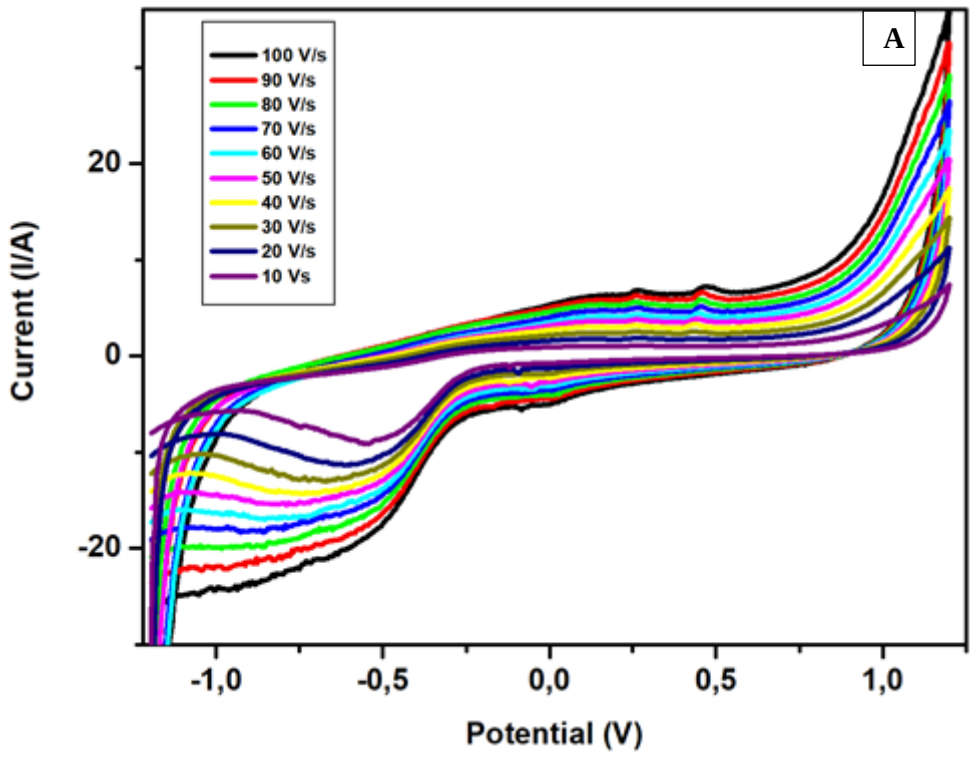

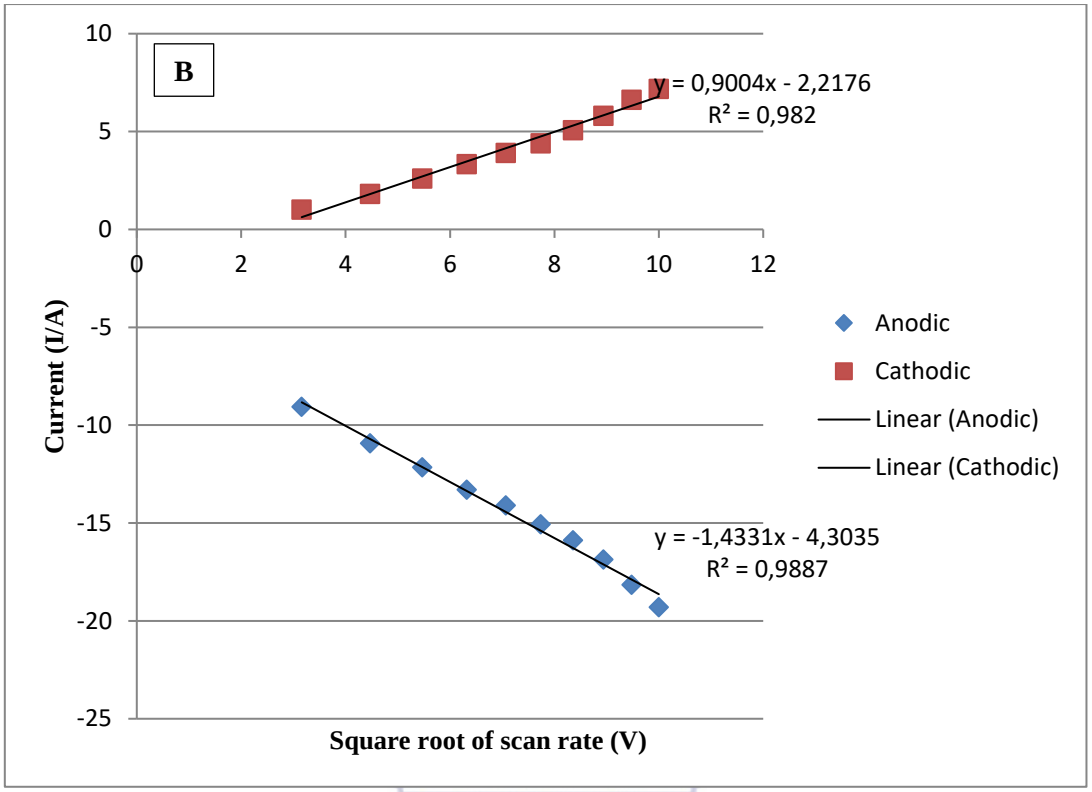

Figure 8.4: (A) Cyclic voltammetry of ZnO NPs/GO composite at different scan rates and (B) Plots of current versus log scan rate of anodic and cathodic peak ZnO NPs/GO composite.

8.4.2. Electrochemical impedance

Electrochemical impedance spectroscopy (EIS) analysis is one of the principle methods for examining the fundamental behaviour of electrode materials. Figure 8.5 (a) shows the impedance spectrum of ZnO NPs/GO composite Nyquist plot. The plot exhibits the absence of semicircle in the higher frequency region and a straight line in the low frequency region. The high–frequency corresponds to the charge transfer limiting process and is impute to the pseudo–capacitance at the contact interface between electrode and electrolyte solution. The straight line in the low frequency range corresponds to the diffusive resistance of the electrolyte into the interior of the electrode and ion diffusion into the electrode surface [5].The Bode plot in Figure 8.5 (B) has enhanced electrochemical properties at low frequency and this could be

attributed to the synergistic effect between GO and ZnO NPs in which a good electron conductor GO is coupled with ZnO NPs to improve the charge transfer between the electrode material and electrolyte resulting in higher electro catalytic response [6]. At high frequency the nanocomposites is found to have no charge effect.

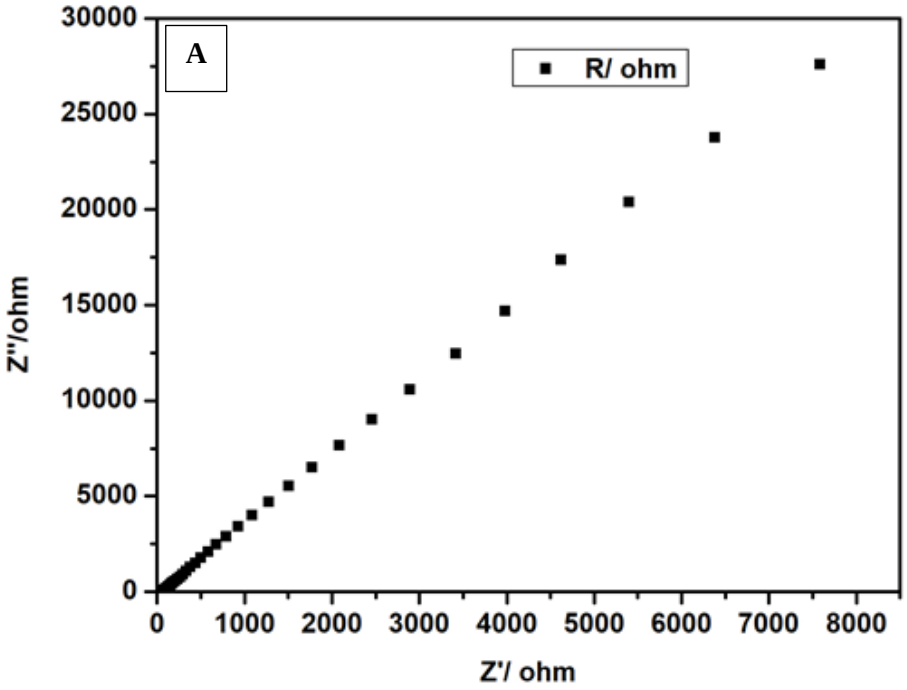

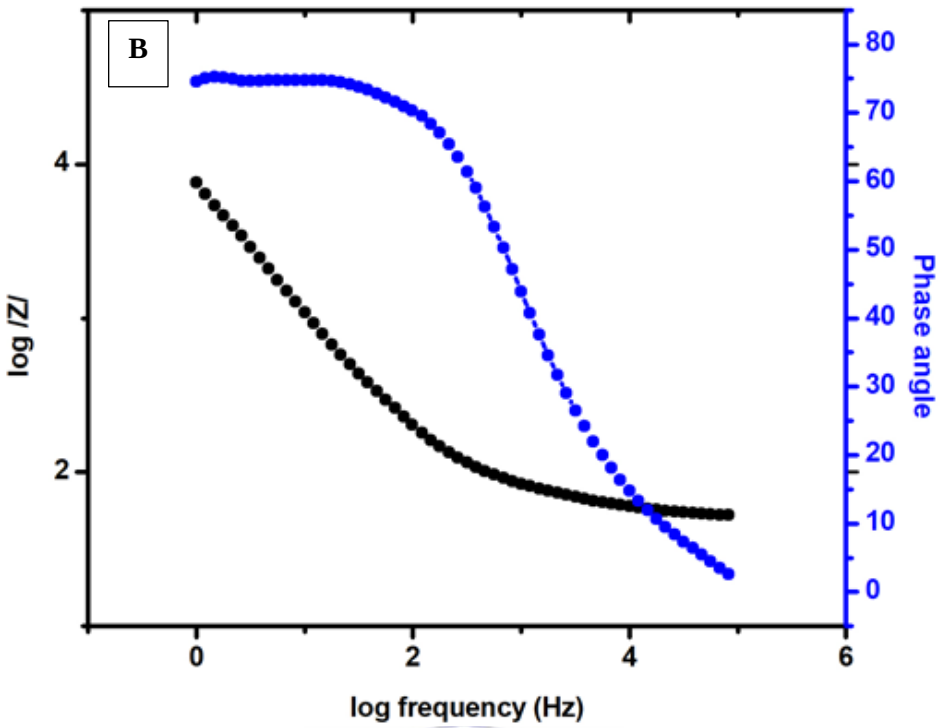

Figure 8.5 EIS data of ZnO NPs/GO (A) Nyquist plot and (B) Bode plot.

8.5. Development and detection of an immunosensor

The CFP-10 immunosensor was developed using ZnO NPs/GO nanocomposite where the antibody CFP-10 was attached onto it. The immunosensor was developed by drop-coating 40 µl of 1-ethyl-3-(3-dimethylaminopropyl) carbodiimide (EDC) and N-hydroxysuccinimide (NHS) onto a glassy carbon electrode at room temperature then left for 5 minutes. After that 10 µl of CFP-10 was added on top of the NHS/EDC followed by the addition of ZnO NPs/GO solution and allowed to dry overnight in the fridge at -2 ^{0}C. The electrode was then washed with 10 µl of 6-mercapto-hexanol and bis (trimethylsilyl) acetamide (BSA) to remove excess nanoparticles on the electrode. The electrode will then be returned to the fridge for an hour before being characterised by CV and EIS in PBS electrolyte.

EIS was employed for sensitivity studying of electrode material on the electrode surface with an electrolyte. Figure 8.6 (B) shows an EIS graph of the developed immunosensor using ZnO NPs/GO/CFP-10 while Figure 8.6 (D) shows the detection of immunosensor which is interpreted by the fitted equivalent circuit shown in Figure 8.6 (E) with the linear graph of charge transfer versus the concentration of the antigen. The detection of ZnO NPs/GO/CFP-10 modified electrode shows an increased R_{ct} as the addition of the antigen increases also illustrating a LOD of $7.3x10^{-4}$ mg/ml. Furthermore by comparing the work previously done by other scientist based on CFP-10 immunosensor, one can conclude that the developed immunosensor in this study is within reasonable acceptance based on the comparison indicated by LOD as shown in Table 3 below.

Table 3: Summary of the developed Antigen-based immunosensor for TB diagnosis using CFP-10.

Target antigens	Biorecognition element	Mechanism of transduction	Detection limit	References
CFP-10	antibody	Surface plasmon optical sensor	0.0001 mg/ml	6
IFN-γantibodies	Antibody	Squarewave anodic stripping electrochemical sensor	$3.4x10^{-10}$ mg/ml	7
CFP-10 antilipoarabinomannan	antibody	Screen printed carbon electrode electrochemical	5.3 mg/ml	8
ESAT-6 Mtb CFP	antibody	Square wave electrochemical	$7.0x10^{-6}$ mg/ml	9
CFP-10	antibody	Impedance electrochemical	$7.3x10^{-4}$ mg/µl	Current work

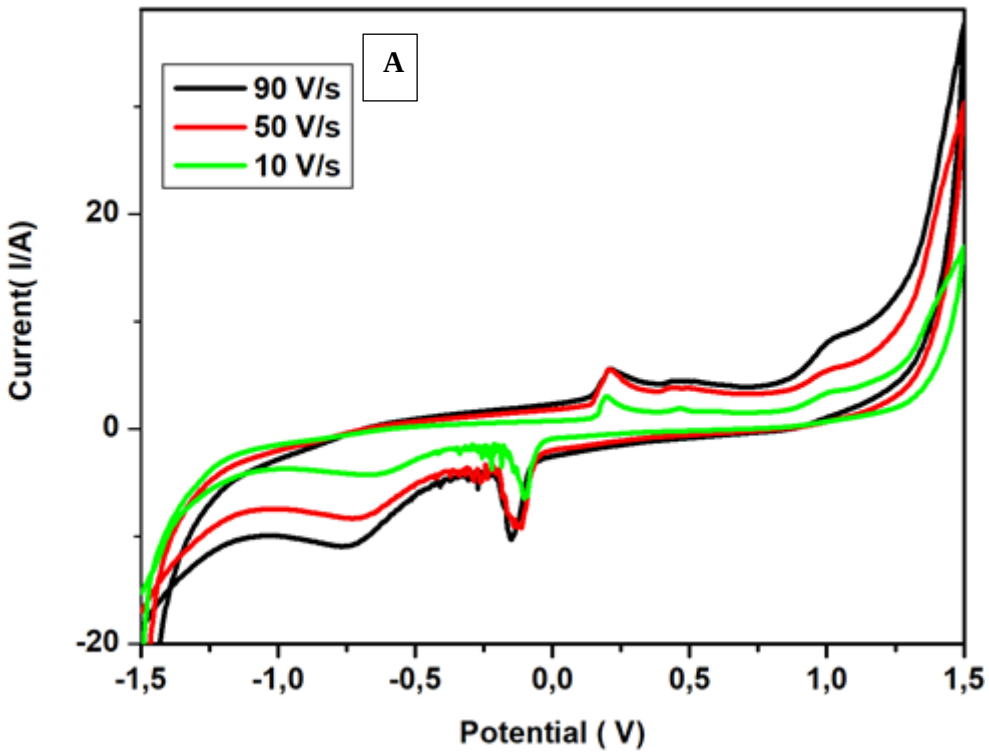

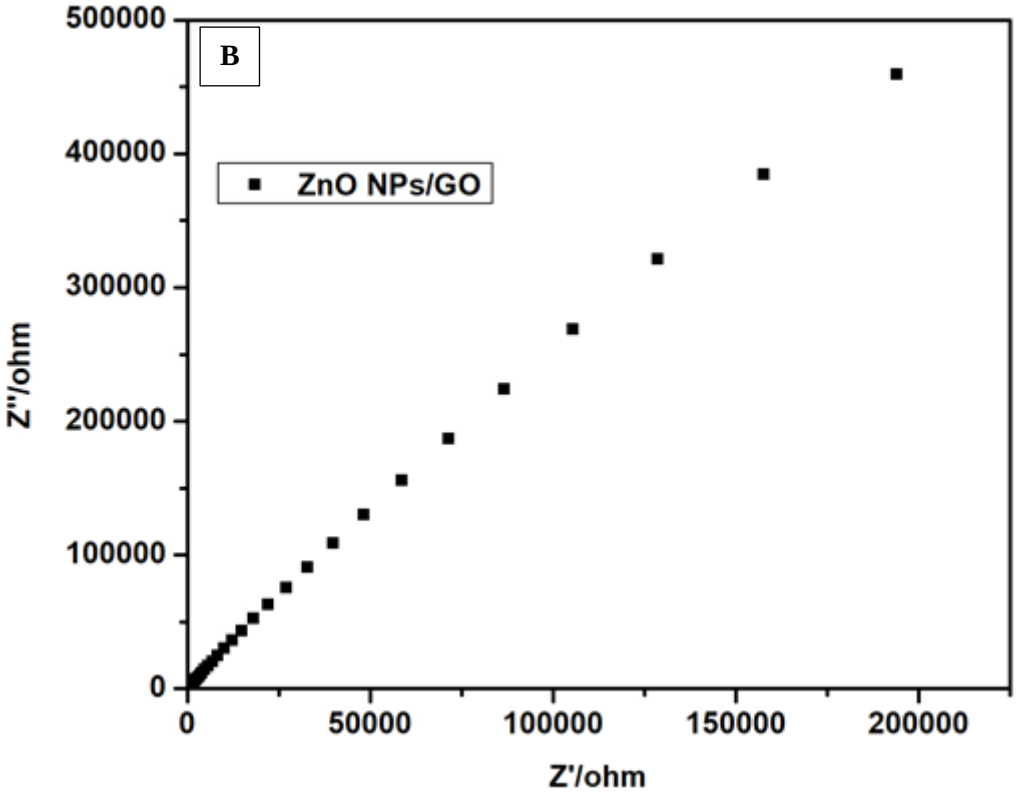

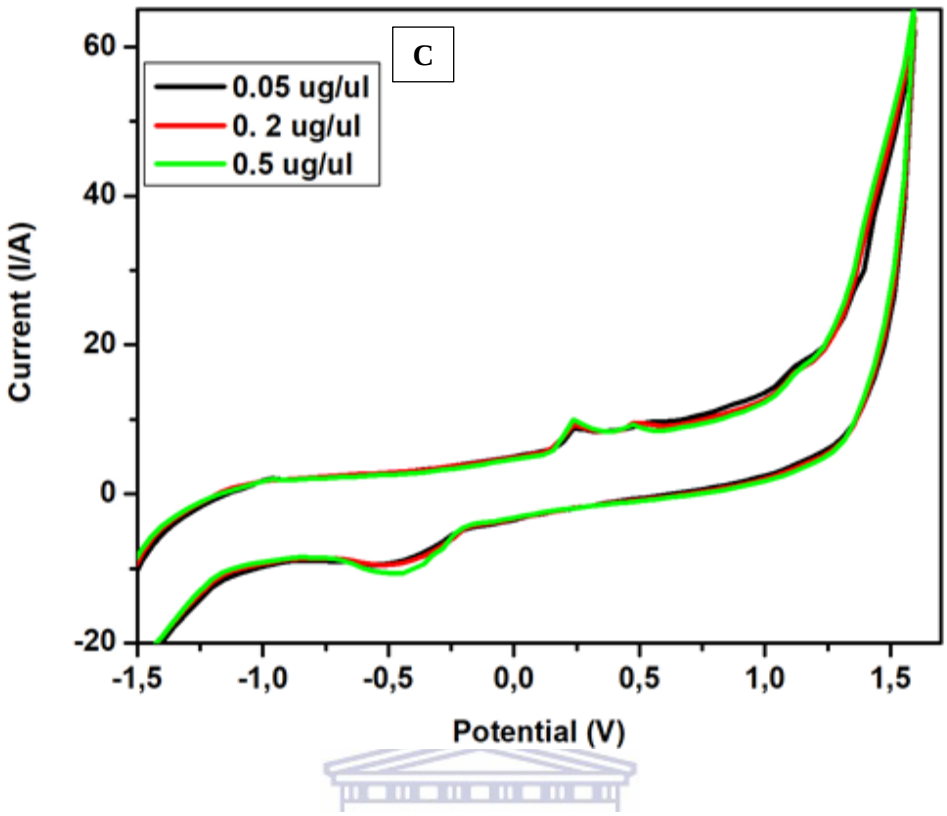

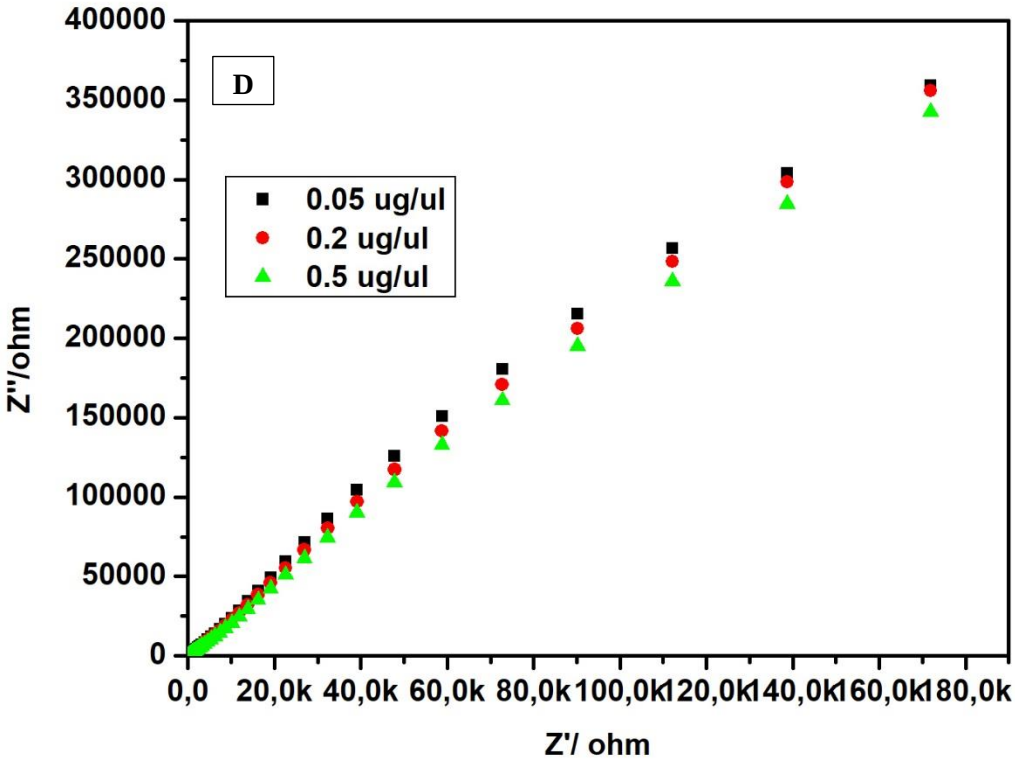

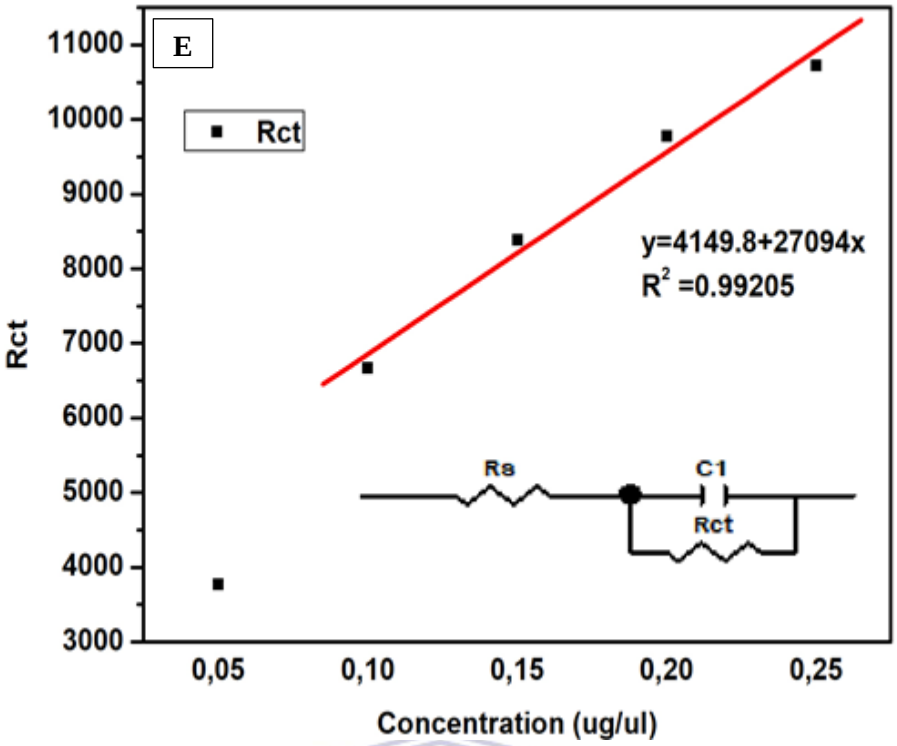

Figure 8.6 (a) immunosensor CV of ZnO NPs/GO/CFP-10, (b) EIS sensor of ZnO NPs/GO/CFP-10, (c) detection cv of anti-CFP-10, (d) detection EIS graph of anti-CFP-10. And (e) linear graph of Rct vs concentration of anti-CFP-10.

8.6. Conclusion

The ZnO NPs/GO composite was successfully synthesized and its structural and morphological studies were studied using HR-TEM, HR-SEM and UV-vis. Electrochemical properties of the electro-active material were tested by cyclic voltammetry (CV) and electrochemical impedance spectroscopy (EIS). Due to excellent properties such as large surface area and the fact that the composites are electro-active as seem from charge transfer and current responses; there is no doubt that they were successful in the development of immunosensors for the detection of anti-CFP-10 antigens.

References

1. Luo, Q.P., Yu, X.Y., Lei, B.X., Chen, H.Y., Kuang, D.B. and Su, C.Y., 2012. Reduced graphene oxide-hierarchical ZnO hollow sphere composites with enhanced photocurrent and photocatalytic activity. *The Journal of Physical Chemistry C*, *116*(14), pp.8111-8117.
2. Tie, W., Bhattacharyya, S.S., Wang, Y., He, W. and Lee, S.H., 2017. Facile in-situ synthesis of a zinc oxide crystals/few-layered graphene flake composite for enhanced photocatalytic performance. *Journal of Photochemistry and Photobiology A: Chemistry*, *348*, pp.89-95.
3. Wu, J., Shen, X., Jiang, L., Wang, K. and Chen, K., 2010. Solvothermal synthesis and characterization of sandwich-like graphene/ZnO nanocomposites. *Applied Surface Science*, *256*(9), pp.2826-2830.
4. Rajeswari, V., Jayavel, R. and Dhanemozhi, A.C., 2017. Synthesis And Characterization Of Graphene-Zinc Oxide Nanocomposite Electrode Material For Supercapacitor Applications. *Materials Today: Proceedings*, *4*(2), pp.645-652.
5. Ezeigwe, E.R., Tan, M.T., Khiew, P.S. and Siong, C.W., 2015. One-step green synthesis of graphene/ZnO nanocomposites for electrochemical capacitors. *Ceramics International*, *41*(1), pp.715-724.
6. Hong, S.C., Chen, H., Lee, J., Park, H.K., Kim, Y.S., Shin, H.C., Kim, C.M., Park, T.J., Lee, S.J., Koh, K. and Kim, H.J., 2011. Ultrasensitive immunosensing of tuberculosis CFP-10 based on SPR spectroscopy. *Sensors and Actuators B: Chemical*, *156*(1), pp.271-275.
7. Huang, H., Li, J., Shi, S., Yan, Y., Zhang, M., Wang, P., Zeng, G. and Jiang, Z., 2015. Detection of interferon-gamma for latent tuberculosis diagnosis using an

immunosensor based on CdS quantum dots coupled to magnetic beads as labels. *Int J Electrochem Sci*, *10*, p.2580.

8. Wang, L., Leng, C., Tang, S., Lei, J. and Ju, H., 2012. Enzyme-free signal amplification for electrochemical detection of Mycobacterium lipoarabinomannan antibody on a disposable chip. *Biosensors and Bioelectronics*, *38*(1), pp.421-424.
9. Diouani, M.F., Ouerghi, O., Refai, A., Belgacem, K., Tlili, C., Laouini, D. and Essafi, M., 2017. Detection of ESAT-6 by a label free miniature immuno-electrochemical biosensor as a diagnostic tool for tuberculosis. *Materials Science and Engineering: C*, *74*, pp.465-470

Chapter 9

Conclusion and recommendations

9.1. Conclusion

A simple green synthesis method of stable silver nanoparticles (Ag NPs) using a pear extract at room temperature was reported in this study. Synthesis was found to be efficient in terms of stability of the synthesized nanoparticles which exclude external stabilizers/reducing agents. It proves to be an eco-friendly, rapid green approach for the synthesis providing a cost effective and an efficient way for the synthesis of silver nanoparticles. Therefore, this reaction pathway satisfies all the conditions of a 100% green chemical process due to benefits of using fruit extract for synthesis of nanoparticles which is energy efficient, cost effective, protecting human health and environment leading to lesser waste and safer products. This eco-friendly method could be a competitive alternative to the conventional physical/chemical methods used for synthesis of silver nanoparticle and thus has a potential to be used in biomedical applications and will play an important role in them being used as nanocomposite for immunosensor application. On the other hand zinc oxide (ZnO NPs) nanoparticles have been successfully synthesized using zinc nitrate at room temperature using strawberry extract and green tea as the capping agent. The synthesized ZnO NPs also have the same benefits as Ag NPs which include energy efficient, cost effective, protecting human health and environment leading to lesser waste and safer products.

In this study we also report the synthesis of graphene (GO) oxide for the synthesis of graphene-nanoparticles composites, thus the GO films were successfully prepared via modified Hummer method. The HR-TEM and HR-SEM analyses showed successful preparation of GO films possessing microscopic morphology with thicknesses of between 2 - 4 nm. The presence of oxygen-containing groups and characteristic peaks in FTIR analysis further determined the successful preparation of GO sheets. The presence of oxygen-containing functional groups

provided more opportunities for potential applications of GO in many areas. This data will provide a reference to further studies in the synthesis of GO/Ag NPs composite for the preparation of immunosensors. Graphene based nanomaterial created unmatched curiosity in the scientific world. The unique structure of its kind not only marked its cavity in the field of electronics (optoelectronics, printed electronics) and energy storages devices but also created a stir in sensing region with incorporation of plasmonic, optically and electrochemically active silver nanoparticles. The different shape and size of silver nanostructures shows excellent properties decorated on the graphene based nanomaterials have an ability to form an intimate contact with graphene to form an atomically smooth layer. The mechanistic aspects of Ag NPs/GO and ZnO NPs/GO nanocomposites imputing towards improving electrochemical immunosensors are understood to be the contribution of both individual structures. The morphological and electrochemical behaviour of the composites was investigated and proved by HR-SEM, HR-TEM and CV respectively which allowed the development of immunosensors whose responses were achieved using CV and EIS. In summary this study describes the successful development of ESAT-6 and CFP-10 immunosensors based on impedance method. The immunosensors were made through the immobilization of graphene-based nanoparticle (Ag NPs/GO and ZnO NPs/GO) ESAT-6 and CFP-10 antibodies respectively on glassy-carbon electrodes. The interaction of the antibody with their ESAT-6 and CFP-10 antigens showed low limit of detections respectively, high selectivity and good reproducibility.

Since ESAT-6 and CFP-10 are one of the earliest secreted mycobacterial proteins in Tuberculosis infected patients, this study is a clear indication that the developed immunosensors could possibly be used in sputum samples to detect Tuberculosis infection.

9.2. Recommendations

Testing ESAT-6 and CFP-10 immunosensor with serums and sputum from positive and negative TB patients is still needed and should be the next step before getting the approval to implement such assay for rapid and specific TB diagnosis.